

# Abstract

The era of gravitational waves astronomy was ushered in by the LIGO (Laser Interferometer Gravitational-Wave Observatory) collaboration with the detection of a binary black hole collision [2]. The event that shook the foundation of space-time allowed mankind to view the cosmos in a way that had never been done previously. Since then, another remarkable event was found by the LIGO and Virgo detectors where two neutron stars collided sending both gravitational and electromagnetic waves to earth [3]. LIGO was built with the purpose of detecting the ripples in space-time caused by astrophysical events with the hopes of understanding the complexities hidden within the cosmos. In 2011, the primary stages of Advanced LIGO were installed and commissioned to start the first observing run (O1). During the writing of this thesis, the detectors had hardware replaced in order to mitigate noise from scattered light and new optics which reduced the losses from absorption. The upgrades were in preparation for the third observing run (O3) and the work presented here is primarily focused on experimental techniques for operating at higher power and mode matching Gaussian beams in the dual-recycled Michelson interferometer for the Advanced LIGO era and beyond. The first two chapters discuss the fundamentals of gravitational waves and the LIGO detector configurations. The third chapter introduces the reader to fundamentals in mode matching Gaussian laser beams. The fourth and fifth chapter summarizes the author's work at Syracuse University and LIGO Hanford observatory in mode sensing and high-powered commissioning.

# Adaptive Mode Matching in Advanced LIGO

Thomas Vo

Spring 2017

# Acknowledgements

I would like to thank my thesis advisor Stefan Ballmer for trusting in me as a scientist, always being there for indispensable advice to push forward, and letting me work on whatever I found interesting and useful.

To Peter Saulson, your stories, love of science, and intuition truly inspires me to be a better scientist and teacher.

To Duncan Brown, being asked questions at the board during group meetings always made me sweat a little but it also made me a better physicist.

To Sheila Dwyer, Jenne Driggers, and Georgia Mansell: thank you for your patience in teaching me the gritty details about the Hanford interferometer, I will never forget the difficult in-chamber work on HAM6 and the long commissioning hours in the control room.

To Daniel Sigg, the dinners were always amazing and thank you for letting me participate in some of the crucial interferometer tasks.

To Keita Kawabe, thank you for the tough questions but also the encouragement to do the best science possible.

To Rick Savage, the Fellows program is one of the best parts of being at Hanford and I was honored to be a part of it for so long, thank you for the advice about all aspects of life and the fishing trips just when I needed it most.

To Aidan

To Daniel Vander-Hyde, thank you for helping at Hanford with your extra hands/brain and being patient with me when things weren't going well but also celebrating when things

were!

To Dan Brown,

To Corey Gray, Gunner and Gomez:

To all the operators and staff at Hanford: Jeff, Betsy, Chandra, TJ, Jim, Cheryl, Nico, Patrick, Ed, Gerardo, Evan.

To Hang Yu, thank you for helping me understand the inner workings of the interferometer with only a few lines of math and a picture.

To all the fellows and visitors who contributed to making my time at Hanford so enjoyable.

To all of my former teachers Melissa Brainerd, Paul Didier, Chrissy Dahms, Carolyn West, and Dan Dorsey: The accumulated effect of my work is a direct result of your teachings, thank you for inspiring kids like me in White Center to chase our dreams.

To my childhood friends Quang, Leah, Thang, Sienna, Khanh, Truc, Kay, Tuan, Wanda, James, Matt and Trung: I've been gone a long time to pursue this work but I know there is always support back home.

To the Bloomingdale family: Thank you for always making me feel at home even in the coldest of Syracuse winters.

To Jaysin Lord, Laura Nuttall, and Mat Hutchens: Thank you for the laughs and Thursday wings.

To my family Cuong, Nhi, Tony, Theresa, Brittny, Kayla, Chloe: Thank you for always supporting in pursuing my dreams

To my parents: I know it was difficult leaving Vietnam to come here, this work is dedicated to you.

To my darling Tiffany: Your support provides nourishment for my soul and your love gives a guiding light through the darkest of nights.

# Contents

<b>Preface</b>	<b>2</b>
<b>1 Introduction</b>	<b>6</b>
1.1 Gravitational Waves . . . . .	6
1.2 Measuring Gravitational Waves with Light . . . . .	8
1.3 Detection of Gravitational Waves . . . . .	13
<b>2 The LIGO Instrument</b>	<b>17</b>
2.0.1 Simple Michelson . . . . .	17
2.0.2 Fabry-Perot Cavities . . . . .	22
2.0.3 Fabry-Perot Michelson . . . . .	28
2.0.4 Power-Recycled Fabry-Perot Interferometers . . . . .	32
2.0.5 Dual-Recycled Fabry-Perot Interferometers . . . . .	34
2.0.6 Fundamental Noise Sources . . . . .	38
2.1 Mode Matching with Squeezed States of Light . . . . .	50
<b>3 The Fundamentals of Mode-Matching</b>	<b>55</b>
3.1 Gaussian Beam Optics . . . . .	56
3.1.1 Misalignment and Higher Order Modes . . . . .	60
3.1.2 Mode Mismatch and Higher Order Modes . . . . .	63
3.2 Wavefront Sensing . . . . .	65

<b>4</b>	<b>Simulating Mode-Matching with FINESSE</b>	<b>72</b>
4.1	FINESSE Simulations . . . . .	74
4.2	Effects of Signal Recycling Mismatch . . . . .	75
<b>5</b>	<b>Experimental Mode Matching Cavities at Syracuse</b>	<b>83</b>
5.1	Commissioning the Real Time Digital System . . . . .	83
5.2	Sensors . . . . .	84
5.2.1	Bullseye Photodiodes (BPD) . . . . .	85
5.2.2	Mode Converters . . . . .	86
5.2.3	DC Mode Matching . . . . .	89
<b>6</b>	<b>Wavefront Control at LIGO Hanford</b>	<b>94</b>
6.1	Hot vs. Cold Interferometers . . . . .	95
6.1.1	Thermal Lensing . . . . .	95
6.2	Wavefront Distortions from Thermal Effects . . . . .	98
6.3	Contrast Defect . . . . .	104
6.3.1	Simple Michelson Contrast Defect . . . . .	105
6.3.2	Modal Contrast Defect . . . . .	106
6.4	Tuning Thermal Compensation for LIGO . . . . .	107
6.4.1	Hartmann Wavefront Sensors . . . . .	108
6.4.2	Ring Heater and CO <sub>2</sub> Commissioning . . . . .	117
6.5	Point Absorbers . . . . .	122
6.6	Higher Power Operation . . . . .	125
6.7	Mode Matching IFO to OMC: Single Bounce . . . . .	127
6.7.1	SR3 Heater . . . . .	127
6.7.2	SRM Heater . . . . .	128
6.8	Mode Matching Squeezer to OMC . . . . .	128

<b>7 Solutions for Detector Upgrades</b>	<b>133</b>
7.1 Sensors . . . . .	133
7.2 High Sensitivity Telescope . . . . .	133
7.3 A Global Active Wavefront Control Scheme . . . . .	134
7.3.1 Hard and Soft Mode Matching . . . . .	134
<b>Appendices</b>	<b>135</b>
<b>A Resonator Formulas</b>	<b>136</b>
<b>B Hermite Gauss Normalization</b>	<b>139</b>
<b>C Bullseye and Quadrant Photodiode Characterization</b>	<b>141</b>
C.1 Quadrant Photodiodes (QPD) . . . . .	141
C.2 Bullseye Photodiodes . . . . .	142
C.2.1 Width . . . . .	143
C.2.2 Pitch . . . . .	144
C.2.3 Yaw . . . . .	145
<b>D Overlap of Gaussian Beams</b>	<b>146</b>

# Chapter 1

## Introduction

This chapter will focus primarily on the theoretical constructs of gravitational waves and underlying principles of using a Michelson interferometer to detect them. The derivations draw heavily on the work of Schutz [79] and Saulson [75].

### 1.1 Gravitational Waves

In 1915, Albert Einstein published his theory of general relativity [37], which contains the most complete description of gravity to date. This theory has stood the test of time and scrutiny by correctly predicting the perihelion of mercury [35], the bending of light from massive objects [5], and the loss of energy from gravitational radiation [88]. The seminal equation in this theory, called the Einstein Field Equation is

$$G_{\mu\nu} = 8\pi T_{\mu\nu} \quad (1.1)$$

which is a set of 10 coupled second-order differential equations that are nonlinear and fully describes the interaction between space-time and mass-energy. Equation 1.1 is difficult to solve except in situations where specific approximations allow a user to find exact solutions such as spherical symmetry [20] [80]. In areas where the curvature is close to flat, the weak

field approximation can be applied and the metric is described as

$$g_{\mu\nu} \approx \eta_{\mu\nu} + h_{\mu\nu} \quad (1.2)$$

where  $\eta_{\mu\nu}$  is the metric of flat spacetime and  $|h_{\mu\nu}| \ll 1$  is the perturbation due to a gravitational field. By plugging in equation 1.2 into 1.1 and using empty space we obtain the familiar wave equation

$$\left( \nabla^2 - \frac{1}{c^2} \frac{\partial^2}{\partial t^2} \right) h_{\mu\nu} = 0 \quad (1.3)$$

which has a plane-wave solution of the form  $h_{\mu\nu} = A_{\mu\nu} e^{ik_\nu x^\nu}$ . Using the gauge constraint  $h_{,\nu}^{\mu\nu} = 0$ , it follows that  $A_{\mu\nu} k^\mu = 0$  which means the gravitational wave amplitude is orthogonal to the propagation vector. Further imposing transverse-traceless gauge and assuming that the wave is traveling in the  $x^3$  direction, it can be shown that the complex amplitude has physical significance expressed in the matrix

$$A_{\mu\nu} = \begin{pmatrix} 0 & 0 & 0 & 0 \\ 0 & A_{xx} & A_{yx} & 0 \\ 0 & A_{xy} & -A_{xx} & 0 \\ 0 & 0 & 0 & 0 \end{pmatrix} \quad (1.4)$$

Oftentimes, the four non-zero components of equation 1.4 can be categorized into two distinct polarizations: plus and cross where  $h_+ = A_{xx} = -A_{yy}$  and  $h_\times = A_{xy} = A_{yx}$ .

Consider the four-velocity,  $U^\alpha$ , in the transverse traceless gauge where the coordinate itself is attached to the particles and incorporates any small wiggles that would shake the coordinates. Of course, any free particles will follow the geodesic equation

$$\nabla U^\alpha = \frac{d}{d\tau} U^\alpha + \Gamma_{\mu\nu}^\alpha U^\mu U^\nu = 0 \quad (1.5)$$

where  $\Gamma_{\mu\nu}^\alpha = \frac{1}{2}g^{\gamma\alpha}(g_{\gamma\mu,\nu} + g_{\gamma\nu,\mu} - g_{\mu\nu,\gamma})$  are the famous Christoffel symbols. By evaluating the first term of the acceleration in equation 1.5,

$$\left( \frac{dU^\alpha}{d\tau} \right)_0 = -\Gamma_{00}^\alpha = \frac{1}{2}\eta_{\mu\nu}(h_{\beta 0,0} + h_{0\beta,0} + h_{00,\beta}) \quad (1.6)$$

However, comparing equation 1.4 and equation 1.6, it is clear that if the particle is initially at rest, then a moment later it is still at rest! The term "at rest" is actually used liberally here since the coordinate system varies along with the gravitational wave. To understand the physical interpretation of equation 1.4, imagine the gravitational wave propagating towards a ring of free floating particles in space. The spacetime will be modulated in a squeezed and stretched motion as shown in Figure 1.1.

Alternatively, one can ask if a gravitational wave passes by a pair of particles separated by length  $L$ , what would be the effect on the distance between two points [78]? The proper distance is defined as

$$\delta l = \int g_{\mu\nu} dx^\mu dx^\nu = \int_0^L g_{xx} dx \approx |g_{xx}(x=0)|^{1/2} \approx [1 + \frac{1}{2}h_{xx}(x=0)]L \quad (1.7)$$

which shows two very important points about the nature of gravitational waves: Firstly, the effect is very small since the length variation,  $h_{xx}$ , is a small perturbation on flat space-time. Secondly, the change in length is proportional to the initial separation between the particles. This means a detector which is large will have a better chance to measure these small effects, an important point that drove the design of the Laser Interferometer Gravitational-Wave Observatory.

## 1.2 Measuring Gravitational Waves with Light

During the famous Chapel Hill Conference in 1957 [8], which included some of the great minds of the era such as Wheeler, Schwinger, and Feynman, the experimental search for

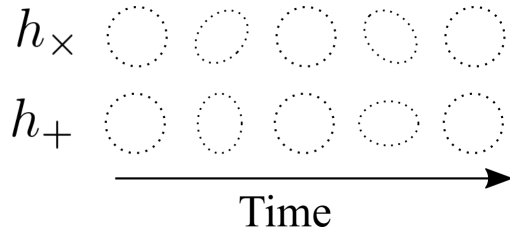


Figure 1.1: **A ring of free floating particles being stretched and squeezed by a passing gravitational wave.** In this picture, the wave is traveling in the transverse direction to the rings (in/out of the page) and the two pictures represent the plus and cross polarizations.

gravitational waves began to take hold. One interesting thought experiment that was proposed by Feynmann [24] where he considered a bead sliding on a string with friction as a gravitational wave passes. As the bead slides back and forth due to the wave described by equation 1.7, there will be some heat dissipated which means the gravitational wave must carry some energy. Even with the theoretical formulation of gravitational waves resolved by the 1970s [72], developing a method of detecting gravitational waves with ground-based instruments was still a controversial topic among scientists [31]. The earliest attempts at detecting these small signals were famously done by Joseph Weber [87] using large aluminum bars and piezoelectric transducers to extract the energy from gravitational waves at the resonant frequencies. However, these bars are limited by thermal noise and could only detect GWs in very narrow frequency bands.

With the development of lasers in the 1960s, which created coherent and spatially confined light that could propagate long distances, another prospect for measuring gravitational waves was born. As light travels in space, it picks up an important quality called *phase* as a function of distance. Interferometers are transducers that measure small displacements by using a laser that is split by a partially transmitting mirror, which allows 50% of the light to get reflected and 50% to be transmitted. Each of the beams travel down the arms and reflect off of mirrors and return to the beamsplitter. Upon reaching the optic, the two beams recombine and by the principle of superposition the electromagnetic waves will add linearly

at the output port (or antisymmetric port), Figure 1.2. The laser beams will gather phase as they propagate down each individual arm, and when recombining, the intensity of the light will be proportional to the phase differences between each beam. This will correspond to a differential length that is described by

$$l_- = l_x - l_y \quad (1.8)$$

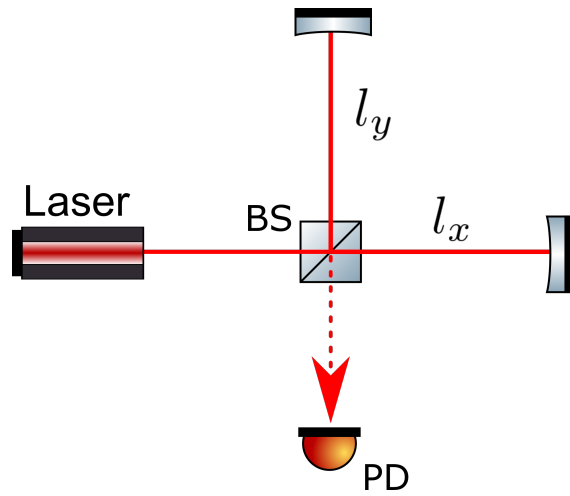


Figure 1.2: **A Michelson Interferometer.** A laser is split between with a partially transmitting optic called a beamsplitter (BS), then propagate down each arm to reflect off mirrors, sometimes called test masses (TM). The beams return to the beamsplitter and recombine, photodetectors are placed at the antisymmetric port (AS).

As shown in equation 1.7, the effect of gravitational waves on the proper length between two free falling objects is proportional to the initial separation. From Figure 1.1, it is intuitively clear that interferometry is an ideal technique to sense signals from a gravitational wave and one can explicitly derive the detector's response to a GW from an astrophysical object.

First, denote the detector's coordinates using  $\hat{x}$  and  $\hat{y}$  to co-align with the interferometer arms respectively such that the  $\hat{z}$  axis points directly towards the zenith. Now consider a gravitational wave source arbitrarily located in the sky with respect to the Earth with the axis of propagation pointed in the  $\hat{z}'$  direction. Using the well known Euler angles, a relation

from the detector frame to the source frame with coordinates  $\{\hat{x}', \hat{y}', \hat{z}'\}$  can be seen in Figure 1.3. If a gravitational wave at the source has emitted GWs with plus and cross polarizations as denoted by equation 1.4, then the detector time series can be regarded as [1] [41]

$$h(t) = F_+(\theta, \phi, \psi) h_+(t) + F_\times(\theta, \phi, \psi) h_\times(t) \quad (1.9)$$

where  $F_+(\theta, \phi, \psi)$  and  $F_\times(\theta, \phi, \psi)$  are the antenna pattern functions that project the gravitational wave amplitudes onto the detector frame shown,

$$F_+(\theta, \phi, \psi) = -\frac{1}{2}[1 + \cos^2(\theta)]\cos(2\phi)\cos(2\psi) - \cos(\theta)\sin(2\phi)\sin(2\psi) \quad (1.10)$$

$$F_\times(\theta, \phi, \psi) = +\frac{1}{2}[1 + \cos^2(\theta)]\sin(2\phi)\cos(2\psi) - \cos(\theta)\sin(2\phi)\sin(2\psi) \quad (1.11)$$

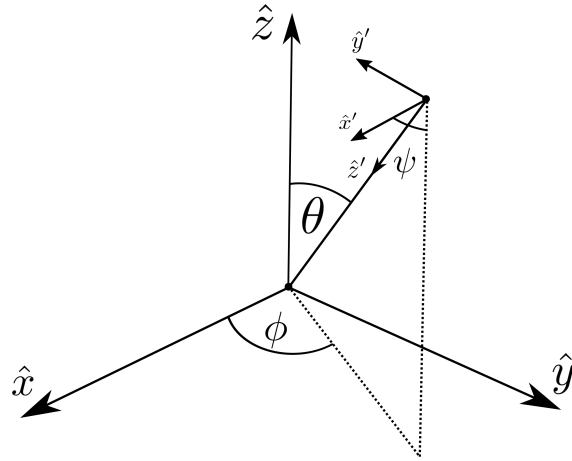


Figure 1.3: **Euler angles of gravitational radiation to the detector frame.** The  $\hat{x}$  and  $\hat{y}$  coordinates line up with the arms of the interferometer whereas  $\hat{z}'$  corresponds to the gravitational wave pointing.

If the gravitational wave is located directly above the interferometer such that  $\theta = 0$  and setting  $\psi = 0$ , then the magnitude of the antenna pattern is equal to unity. Furthermore, by rotating about the  $\phi$  angle such that the detector arms align with the plus polarization,

the null geodesic equation (ie the path of a photon) in the interferometer frame becomes

$$ds^2 = g_{\mu\nu}dx^\mu dx^\nu = -dt^2 + [1 + h_+]dx^2 + [1 - h_+]dy^2 + dz^2 = 0 \quad (1.12)$$

Now, if the photon is traveling along the x-arm, this means that  $dy^2 = dz^2 = 0$  and the metric equation transforms to

$$\frac{dt}{dx} = \sqrt{1 + h_+} \approx 1 + \frac{1}{2}h_+ \quad (1.13)$$

The amount of time required for the photon to reach the x-end mirror (starting at  $t = 0$ ) is equal to

$$t_1 = \int_0^{l_x} [1 + \frac{1}{2}h_+(x)]dx \quad (1.14)$$

where  $l_x$  is the total length of the x-arm. Upon returning to the beamsplitter, the photon's total time of flight for the x and y arms are, respectively,

$$t_2 = 2l_x + \frac{1}{2} \int_0^{l_x} [h_+(x) + h_+(x + l_x)]dx \quad (1.15)$$

$$t'_2 = 2l_y - \frac{1}{2} \int_0^{l_y} [h_+(y) + h_+(y + l_y)]dy \quad (1.16)$$

If the gravitational wave period is much longer than the time of flight, then  $h_+$  does not change much during the measurement, which means  $h_+(\eta_i) \approx h_+(\eta_i + l_i) \approx constant$ . By subtracting the flight times of the photons for each arm and setting  $l = l_x = l_y$ , the difference is proportional to the gravitational wave perturbation multiplied by the sum of arm lengths (with a factor of  $c$  to get the units right),

$$\Delta t = t_2 - t'_2 = \frac{2l}{c}h_+ \quad (1.17)$$

By recasting the expression for time of flight in terms of the phase picked up laser light as

it travels through space, the differential phase shift is

$$\Delta\Phi = \Phi(t_2) - \Phi(t'_2) = \frac{4\pi}{\lambda} h_+ l \quad (1.18)$$

The equation above is simple, however, it only works for gravitational wave signals that are not frequency dependent and it assumes that the path length can be arbitrarily long. Both points are actually not true [75] but we can alleviate these discrepancies by considering a gravitational wave signal of the form  $h(t) = h_0 e^{i2\pi f_{GW} t}$  and repeating the calculation between equations 1.14 and 1.18:

$$\Delta\Phi(t) = h(t) \tau_{RT} \frac{2\pi c}{\lambda} \text{sinc}(f_{GW}\tau_{RT}) e^{i\pi f_{GW}\tau_{RT}} \quad (1.19)$$

where  $\tau_{RT} = 2l/c$ . The response for a detector has null points from the sinc function that is dependent on the gravitational wave frequency and the round trip time constant. This means that the instrument cannot be arbitrarily long, however, it is very expensive and difficult to make a terrestrial detector of this size. On the other hand, space-based detectors such as the LISA project will have to account for this effect. Figure 1.4 compares the response of an interferometer with 4 km arms versus 100 km, there is larger low frequency response for the longer detector but has large dips when approaching the kilohertz regime where solar mass compact binaries tend to merge. Laying out the response to gravitational waves is one thing but practically measuring  $\Delta\Phi$  to detect astrophysical objects requires much more complex systems, so building modern detector is explained in Chapter 2.

### 1.3 Detection of Gravitational Waves

The purpose of LIGO is to observe gravitational waves emanating from astrophysical objects [38], so it is natural to wonder how well a single detector can probe the universe. It is worthwhile to explicitly derive the inspiral horizon distance, which is how far a single detector

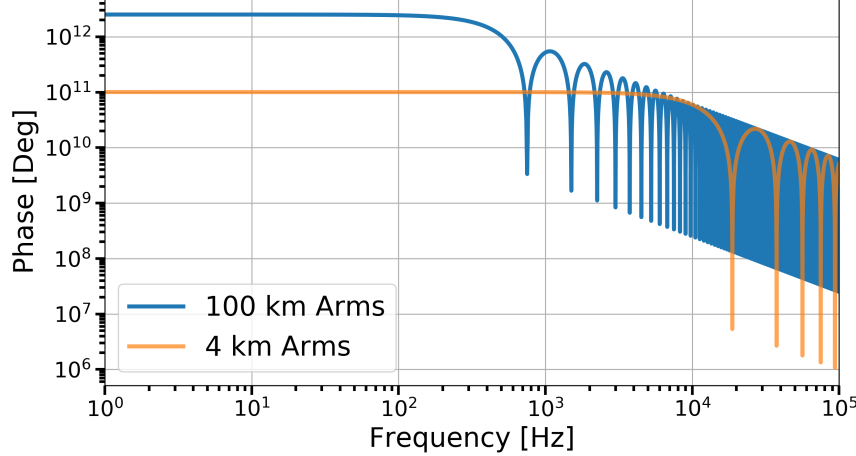


Figure 1.4: **The phase response of an interferometer to a gravitational wave.** The horizontal axis is in GW frequency and the vertical axis is the accumulated phase shift.

can detect a binary system comprised of two equal mass compact objects optimally oriented in the sky relative to the detector. Signal-to-noise (SNR) is the comparison of foreground triggers to the background noise, which can be expressed as

$$\rho = 2 \int_{-\infty}^{\infty} \frac{\tilde{s}(f)\tilde{s}^*(f)}{S_n(f)} \quad (1.20)$$

where  $S_n(f)$  is the one-sided average power spectral density of the detector noise and  $\tilde{s}(f)$  is the Fourier transform of the detectors' response to a gravitational-wave signal.

Consider two dense objects which are approximated by points sources with mass  $m_1$  and  $m_2$  spiraling around each other. They are separated by a distance  $R$  such that the quadrupole equation from 1.2 still holds (i.e. flat space-time with small perturbations). The detector response, in units of strain, to the gravitational waves emitted by this type of source is [41],

$$s(t) = \frac{\mathcal{M}}{d_L} \Theta(\theta, \phi, \psi, i) [\pi f(t) \mathcal{M}]^{2/3} \cos[\Phi(t) + \text{constant}] \quad (1.21)$$

where

$$\mathcal{M} = (1+z) \frac{(m_1 m_2)^{3/5}}{(m_1 + m_2)^{1/5}} \quad (1.22a)$$

$$\Theta(\theta, \phi, \psi, i) &= 2\sqrt{[F_+(\theta, \phi, \psi)(1 + \cos^2(i))]^2 + [2F_\times \cos(i)]^2} \quad (1.22b)$$

and  $F_+$  and  $F_\times$  are the antenna response of the interferometer in equations 1.10 and 1.11. By convention,  $\mathcal{M}$  is called the chirp mass and  $d_L$  is the luminosity distance. The orientation response,  $\Theta(\theta, \phi, \psi, i)$ , is a function that depends entirely on the detector orientation relative to the angular momentum vector of the binary. As the system emits gravitational waves, the orbit will shrink as a function of time, in turn, the orbital frequency will increase by

$$f(t) = \frac{1}{\pi \mathcal{M}} \left[ \frac{5}{256} \frac{\mathcal{M}}{T-t} \right]^{3/8} \quad (1.23)$$

Defining the binary phase as  $f(t) = \frac{1}{2\pi} \frac{\partial \Phi}{\partial t}$ , it is easy to recognize that it also evolves with time.

$$\Phi(t) = 2\pi \int_T^t f(t) dt = -2 \left( \frac{T-t}{5\mathcal{M}} \right)^{5/8} \quad (1.24)$$

What this means is that the gravitational wave signal from the binary will increase in amplitude and frequency as a function of time up until the coalescence time,  $T$ . There is actually a subtle difference between the coalescence time and the moment when adiabatic approximations fail which allows usage of the quadrupole formulation. Plugging equation 1.21 into 1.20,

$$\rho = 8\Theta(\theta, \phi, \psi, i) \frac{r_0}{d_L} \left( \frac{\mathcal{M}}{1.2M_\odot} \right)^{5/6} \zeta(f_{\max}) \quad (1.25)$$

There are two important functions in the equation above that reflect the detector's performance in sensing gravitational radiation from a binary inspiral,  $r_0$  and  $\zeta(f_{\max})$ . The characteristic distance,  $r_0$  is how far the detector can see for a fixed binary's mass distribution,

$$r_0^2 = \frac{5}{192\pi^{4/3}} \left( \frac{3M_\odot}{20} \right)^{5/3} \int_0^\infty \frac{1}{S_n(f)} \frac{df}{f^{7/3}} \quad (1.26)$$

Due to the integrand's dependence on  $f^{-7/3}$ , lower frequency improvements in the detector's

noise spectrum will contribute more to the distance.

$$\zeta(f_{\max}) = \frac{\int_0^{2f_{\max}} \frac{1}{S_n(f)} \frac{df}{f^{7/3}}}{\int_0^{\infty} \frac{1}{S_n(f)} \frac{df}{f^{7/3}}} \quad (1.27)$$

The sensitivity can be different for various mass distributions;  $\zeta(f_{\max})$  is a normalized function that describes how well the detector's bandwidth overlaps the binary's frequency evolution. If  $f_{\max}$  sweeps across the detector's most sensitive frequency band (generally between 80 and 400 Hz), there can be relatively good overlap and  $\zeta(f_{\max}) \approx 1$ . However, if the masses are sufficiently large,  $f_{\max}$  will be lower because coalescence occurs before the objects reach a high enough frequency regime and this will result in  $\zeta(f_{\max}) \approx 0$ .

The process of two compact objects coalescing starts at lower frequencies and terminate at a maximal frequency,  $f_{\max}$ , that depends on when the objects reach their inner-most stable circular orbit,  $f_{\text{ISCO}}$ . If  $m_1 = m_2$ , then the maximum frequency is [41]

$$f_{\max} = \frac{f_{\text{ISCO}}}{1+z} = \frac{99\text{Hz}}{1+z} \frac{20M_{\odot}}{M} \quad (1.28)$$

where  $M = m_1 + m_2$ . This is what gives a compact binary coalescence its wonderful characteristic chirp!

# Chapter 2

## The LIGO Instrument

When gravitational waves were first detected, the first question on everybody's mind was: **"Is it real?"**.

The next was, **"How do we get more?"**.

The previous chapter dealt with gravitational waves and briefly touched on how a laser interferometer is particularly well-suited for detecting them. In its simplest form, the LIGO instrument is an incredibly large Michelson interferometer. However, to make a practical gravitational-wave observatory, the complexity had to be extended far beyond what Michelson and Morley used. The next sections will explore the various instrument configurations that improve LIGO's sensitivity and a few fundamental noise sources.

### 2.0.1 Simple Michelson

As shown in Figure 1.2, the interferometer begins with a laser which is incident on a partially-reflecting and partially-transmitting beamsplitter that sends half of the laser light down each arm. The individual beams gather phase as they propagate down the arms and then reflect off of two end mirrors and eventually recombine at the same beamsplitter. Whether the light constructively or destructively interferes will depend on their relative accumulated phase from propagating down each arm. A photodetector is placed at the output and measures

the total power which converts the total amount of light into an electronic signal. In Section 1.2, it was shown that the differential time of flight between photons traveling down the individual arms carry gravitational wave information. The difference in flight times,  $\Delta t$ , can be converted into how much phase,  $\Delta\phi$ , is accumulated by the photons as they propagate through space.

But the question remains, how does an interferometer explicitly measure  $\Delta\phi$ ? If the input electric field of the interferometer is  $E_0$ , the beamsplitter will transmit  $iE_0/\sqrt{2}$  down the x-arm and reflect  $E_0/\sqrt{2}$  towards the y-arm. By setting the beamsplitter to be the origin, the two plane waves traveling down their respective arms will have gathered a phase  $\phi_i$ , where the individual arms are denoted by the subscripts. Then, upon reflecting off the end mirrors and returning to the beamsplitter the resultant fields are transmitted to the antisymmetric port. Each of the electric fields from the arms can be described by these equations

$$\begin{aligned} E_x &= \frac{iE_0}{2} e^{2i\phi_x} \\ E_y &= \frac{iE_0}{2} e^{2i\phi_y} \end{aligned} \quad (2.1)$$

Since the electromagnetic waves are linear, the resultant sum of waves at the antisymmetric port will be  $E_{out} = E_x + E_y$ . The photodiode at the output (or antisymmetric) port detects the integrated power which is related to the total electric field by

$$\begin{aligned} P_{AS} &= \int_{\text{Area}} I \, dA \\ &= \int_{\text{Area}} |E_x + E_y|^2 \, dA \\ &= P_{in} \cos^2(\Delta\phi) \end{aligned} \quad (2.2)$$

where  $\Delta\phi = \phi_x - \phi_y = k_x l_x - k_y l_y$  and  $P_{in} = \int_{\text{Area}} |E_0|^2 \, dA$  is the input power. By using equation 1.18 and the common (or average) arm length  $l_+ = \frac{l_x + l_y}{2}$ , the power due to a

differential phase shift is

$$P_{AS}|_{\text{Bright}} \approx P_{in} (1 - 2\Delta\phi) = P_{in} (1 - 2kl_+h_+) \quad (2.3)$$

There is a large DC term that is dependent on the input power and generally, it is very difficult to measure small changes in a large signal. This configuration can be referred to as being on a bright fringe. So the next obvious method is to shift the arm lengths such that the output port is operating on a dark fringe, normally this is called a null-point operation. However, there are difficulties associated with this method as well. Consider shifting the phase of equation 2.2 by  $\pi/2$ , which would result in

$$P_{AS}|_{\text{Dark}} = P_{in} \sin^2(\Delta\phi) \approx P_{in} (kl_+h_+)^2 \quad (2.4)$$

This results in a second-order dependence on a gravitational-wave signal that is already approximated to be very small. So a good solution to the issue of how to *read out* a gravitational wave signal can be remedied using radio frequency (RF) detection methods. By changing the interferometer input from a single laser to adding an electro-optical modulator (EOM) that sinusoidally modulates the laser frequency and expanding to first order using the Bessel functions,

$$\begin{aligned} E_{in} &= E_0 e^{i(wt + \beta \cos(\Omega t))} \\ &\approx E_0 e^{iwt} [J_0(\beta) + J_1(\beta)e^{i\Omega t} + J_1(\beta)e^{-i\Omega t}] \\ &= E_{C,in} + E_{SB+,in} + E_{SB-,in} \end{aligned} \quad (2.5)$$

where  $\Omega$  and  $\beta$  are the modulation frequency and depths, respectively. The first term is commonly called the carrier field whereas the second and third terms are referred to as the (upper or lower) sidebands. Because there are multiple electric fields, it is useful to define

an optical transfer function which maps the interferometer's input fields to its output,

$$E_{out} = E_C + E_{SB+} + E_{SB-} = \begin{pmatrix} t_C \\ t_{SB+} \\ t_{SB-} \end{pmatrix} \begin{pmatrix} E_{C,in} & E_{SB+,in} & E_{SB-,in} \end{pmatrix} \quad (2.6)$$

The carrier transfer function,  $t_C$  has already been calculated by equations 2.2 - 2.4 and the sideband transfer functions are not much different.

$$t_{SB\pm} = r_{x,\pm} e^{i\phi_{\pm,x}} - r_{y,\pm} e^{i\phi_{\pm,y}} \quad (2.7)$$

where  $\phi_{\pm,i} = (k \pm k_\Omega) \ell_i = (\frac{w+\Omega}{c}) \ell_i$ . In the current example, the sidebands and carrier fields reflect off the mirrors identically, however, this will not be true in general when dealing with resonators that are highly frequency dependent. Plugging equation 2.7 into 2.6, the output electric field becomes

$$E_{out} = ie^{iwt}[J_0(\beta)k\ell_+h_+ + J_1(\beta)\sin(k\Delta\ell + k_\Omega\Delta\ell)(e^{i\Omega t} + e^{-i\Omega t})] \quad (2.8)$$

where  $\Delta\ell = \frac{l_x - l_y}{2}$  is the average differential arm length. The frequency offset of the sidebands allow them to accumulate phase differently than the carrier field. Thus, by choosing a static offset between the arm lengths such that the carrier signal is on a dark fringe,  $k\Delta\ell = \pi/2$ , but the sideband are slightly off the null point (Figure [2.1]) and leak into the anti-symmetric port. This technique is colloquially known as the *Schnupp Asymmetry* and the electric field reduces to

$$E_{out} = ie^{iwt}[J_0(\beta)k\ell_+h_+ + J_1(\beta)\sin(k_\Omega\Delta\ell)(e^{i\Omega t} + e^{-i\Omega t})] \quad (2.9)$$

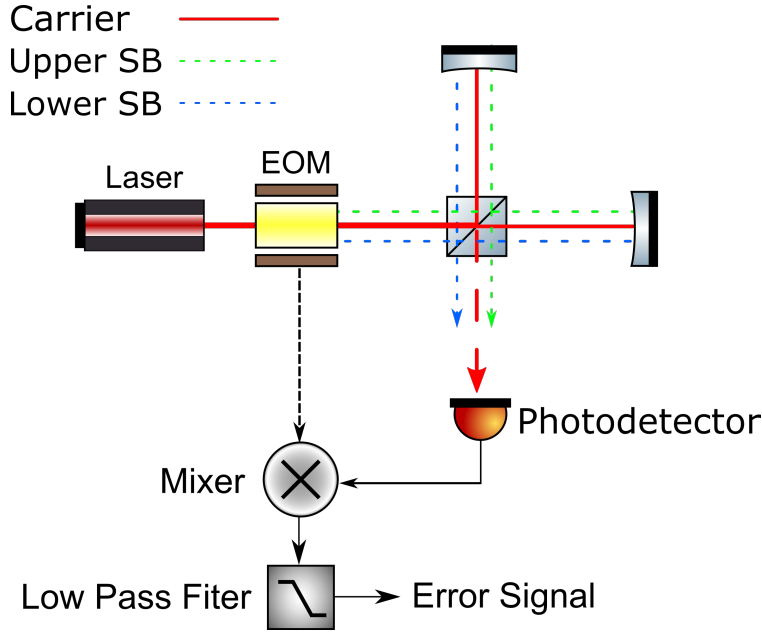


Figure 2.1: **A heterodyne detection scheme for interferometers.** The laser enters an electro-optical modulator which creates three fields described by equation 2.5 and read out by a photodetector. The error signal at the output is then filtered and described by equation 2.12.

The intensity, which is equal to the electric field squared can be described by

$$\begin{aligned}
 I = |E_{out}|^2 = & |E_C|^2 + |E_{SB+}|^2 + |E_{SB-}|^2 \\
 & + 2\text{Re}\{ E_{SB+}E_{SB-}^* e^{2i\Omega t} \} \\
 & + 2\text{Re}\{ (E_C E_{SB-}^* + E_{SB+} E_C^*) e^{i\Omega t} \}
 \end{aligned} \tag{2.10}$$

The last term is referred to as the *beat note* between the carrier signal and the sidebands. To extract the term at the modulation frequency, one can use a mixer which is an analog device that outputs the product of two inputs. Usually, the same oscillator that was used to modulate the input beam can be one of the mixer inputs,  $\cos(\Omega t)$ , so that the demodulated signal is

$$\begin{aligned}
 I_{\text{Demod}} \propto & [4\pi J_0(\beta) J_1(\beta) \frac{\ell_+}{\lambda} \sin(k_\Omega \Delta \ell) h_+] [\cos(\Omega t) \sin(\Omega t + \phi_{\text{Demod}})] \\
 \propto & [4\pi J_0(\beta) J_1(\beta) \frac{\ell_+}{\lambda} \sin(k_\Omega \Delta \ell) h_+] [\sin(\phi_{\text{Demod}}) + \sin(2\Omega t + \phi_{\text{Demod}})]
 \end{aligned} \tag{2.11}$$

where  $\phi_{\text{Demod}}$  is the phase that can be set by the user in order to account for extra phase shifts (ie. longer cables). After the mixer, there will be signals at DC,  $\Omega$ ,  $2\Omega$  and so on. However, the part that is linear in the gravitational wave amplitude will be at DC so a low-pass filter will allow the final signal to dominate [9]:

$$S = 4\pi J_0(\beta) J_1(\beta) \frac{\ell_+}{\lambda} \sin(k_\Omega \Delta\ell) \sin(\phi_{\text{Demod}}) h_+ \quad (2.12)$$

This shows that a RF detection technique will be linear in GW signal with no large DC offset. Setting the carrier on a null point means  $\Delta\ell = \frac{k_\Omega \pi}{k}$  and allows the designer to optimize the Schnupp asymmetry length to get the best signal for some modulation frequency. This type of readout scheme was used in Enhanced LIGO and is called heterodyne detection, where the sideband fields are produced by an EOM and its efficacy depends on the local oscillator's stability [45]. In contrast, the Advanced LIGO scheme uses a homodyne detection [53] method called "DC-Readout". Here, the oscillator field is produced by slightly offsetting the arms away from the dark fringe and letting a small amount of carrier light through the antisymmetric port. A gravitational wave will induce sidebands on the carrier and this will allow the same mathematics as above to achieve a linear signal in gravitational wave strain. This method benefits from naturally being co-aligned and mode matched with the signal field. All techniques follow the same logic of beating the field containing useful information with a reference field to extrapolate a linear signal but the differences come from technical noise such as laser intensity fluctuations and effective quantum noise.

## 2.0.2 Fabry-Perot Cavities

There are two ways to improve the LIGO detectors: one is to increase the response from gravitational waves and the other is to decrease the noise contributions. From equation 1.18, the gravitational wave signal is proportional to the optical path length that the photon travels, which means the most straightforward method of increasing the sensitivity is to make

the arms as long as possible (up to the null point described by equation 1.19). There are two methods to achieve this: a Herriott delay line or a Fabry-Perot resonator, the differences between each method is shown in Figure 2.2. At the time of writing this thesis, all modern gravitational wave detectors use the latter method.

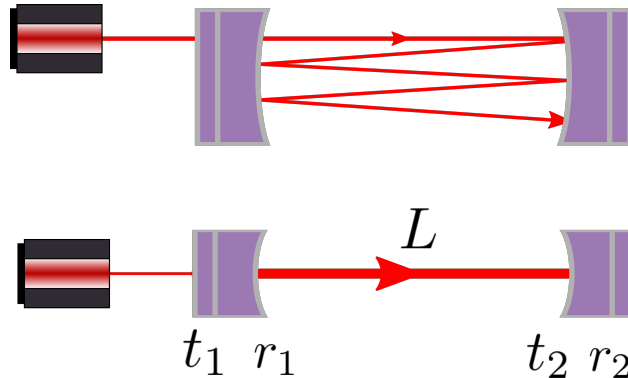


Figure 2.2: Delay Line (top) vs Fabry Perot (bottom)

A Fabry-Perot cavity is an optical system comprised of two or more partially transmitting mirrors with one laser input. To create such a resonator, the user must design a system so that once the electric field has made one round trip within the optical system, the phase of the beam is the same as when it started such that it constructively interferes. This is done by changing the cavity length, which may seem simple conceptually but in practice, controlling and sensing any optical cavity comes with a few challenges.

To start understanding the longitudinal degree of freedom, consider a two mirror system in Figure 2.2 which is separated by a length  $L$  with reflection and transmission coefficients:  $r_1$ ,  $t_1$ ,  $r_2$ ,  $t_2$ . Starting with a plane wave at the input mirror with amplitude  $E_0$ , the beam will enter the cavity and propagate back between the two mirrors. The reflected, transmitted, and circulating fields [75], which are a result of the geometric series, can be described as

$$E_{\text{REFL}} = r_{FP} E_0 = \left( -r_1 + \frac{t_1^2 r_2 e^{-i2kL}}{1 - r_1 r_2 e^{-i2kL}} \right) E_0 \quad (2.13)$$

$$E_{\text{TRAN}} = t_{FP} E_0 = \left( \frac{t_1 t_2 e^{ikL}}{1 - r_1 r_2 e^{-i2kL}} \right) E_0 \quad (2.14)$$

$$E_{\text{CIRC}} = c_{FP} E_0 = \left( \frac{t_1}{1 - r_1 r_2 e^{-2ikL}} \right) E_0 \quad (2.15)$$

The above fields are all highly dependent on the round trip phase accumulated within the cavity which becomes resonant when the length is  $L = n\lambda/2$ . While on resonance, the circulating coefficient in the cavity is maximized such that the gain is

$$\text{Gain} = c_{FP}^2 |_{\text{resonating}} = \left( \frac{t_1}{1 - r_1 r_2} \right)^2 \quad (2.16)$$

Notice that the fields are dependent on the cavity length and laser frequency,  $2kL$ , so one

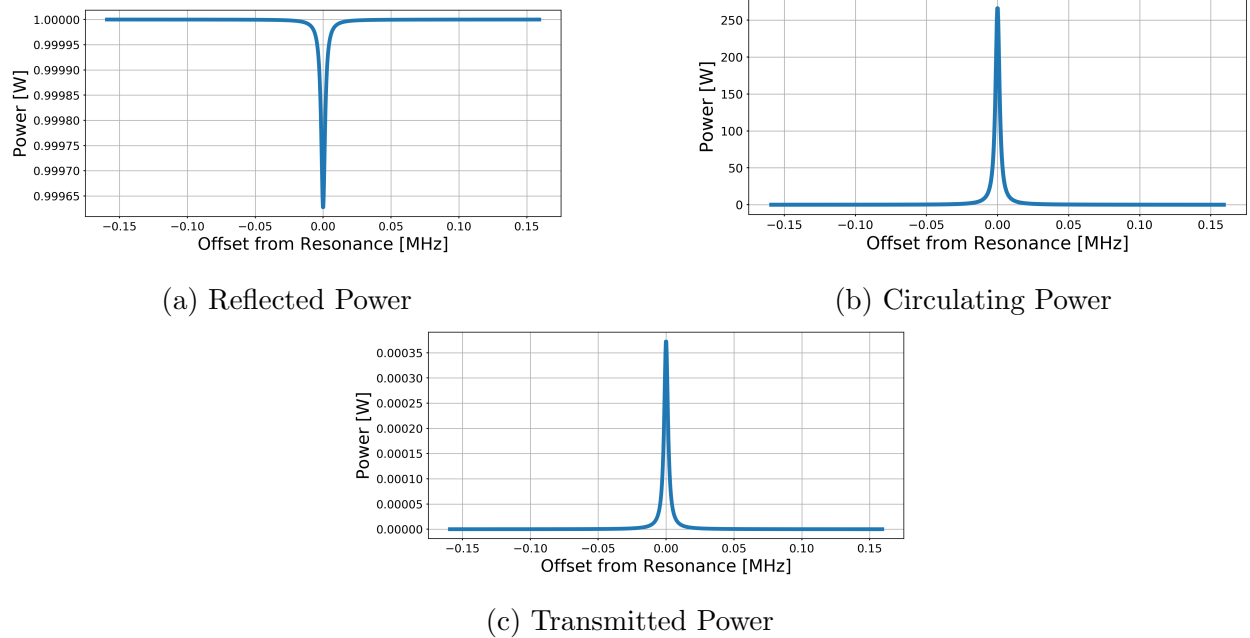
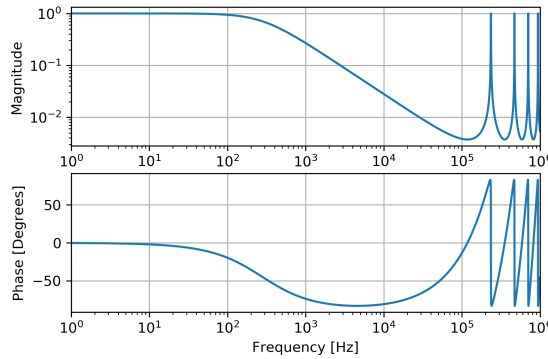


Figure 2.3: The has properties in Table [] to represent one of the LIGO 4km arms which are highly over-coupled cavities so almost all of the light reflects toward the beamsplitter. The input power is normalized to 1 Watt to show the relative gain of the circulating power.

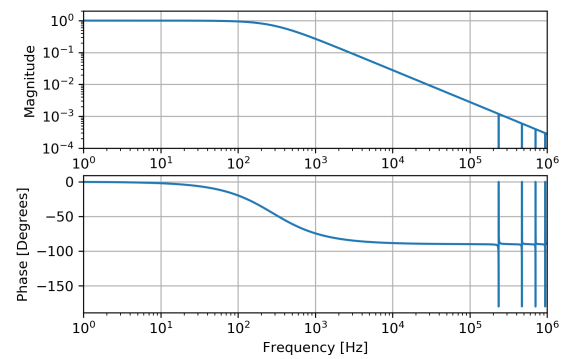
might naively determine that modulating the two parameters independently cause the same effect. However, when both are changing by large amounts, they are related by a frequency dependent transfer function [61]

$$C(\omega) \frac{\Delta\omega}{\omega} = -\frac{\Delta L}{L} \quad (2.17)$$

where  $C(\omega) = \frac{1-e^{-2i\omega L/c}}{2i\omega L/c}$ . It is only when the cavity is on resonance that the frequency and length variations are related by  $\frac{\Delta\omega}{\omega} = -\frac{\Delta L}{L}$ . Depending on the relative reflection coefficients of the input and output mirrors, the fields on resonance will be different in amplitude. For example, in the LIGO 4 km arms, the end test masses are highly reflective with a transmission of about 4 parts per million while the input test masses have a transmission of about 0.015. This means that the arm cavities are very much over-coupled and almost all of the light reflects back towards the beamsplitter. It is important to understand the



(a) Transfer function with respect to L



(b) Transfer function with respect to F

Figure 2.4: Bode Plots of a linear Fabry-Perot response in reflection.

Fabry-Perot response while sweeping through either the laser frequency or cavity length and measuring the reflected (or transmitted) fields, there are features of the power spectrum which relate directly to the cavity's physical properties.

The finesse describes the line width of the resonant peak and is function of  $r_1$  and  $r_2$ . A higher finesse will mean the line width is smaller and taller:

$$\mathbb{F} = \frac{\pi\sqrt{r_1 r_2}}{1 - r_1 r_2} \quad (2.18)$$

The cavity storage time,  $\tau_s$ , describes how long it takes the power circulating in the cavity to decay by a factor of  $1/e$  if the laser suddenly turns off,

$$\tau_s = \frac{L}{c\pi} \mathbb{F} \quad (2.19)$$

The pole frequency,  $f_{\text{pole}}$ , is when the magnitude of the cavity's transfer function (see Figure 2.4 ) reaches 3db below the DC level:

$$f_{\text{pole}} = \frac{1}{4\pi\tau_s} \quad (2.20)$$

The free spectral range, $f_{\text{FSR}}$ , is the frequency span from one resonant peak to the next.

$$f_{\text{FSR}} = \frac{c}{2L} \quad (2.21)$$

It is useful to understand the power circulating as a function of our defined parameters slightly off resonance by a length of  $\Delta L$

$$P_{\text{cav}} = |c_{FP}|^2 = \frac{\text{Gain}}{1 + \left(\frac{2F}{\pi}\right)^2 \sin^2(k\Delta L)} \quad (2.22)$$

In order to prove that an optical cavity is stable, it is useful to introduce the matrices that describe a periodic optical system which is explicitly derived in appendix A. A Fabry Perot cavity that is separated by distance  $L$  with spherical mirrors that have radii of curvature  $R_1$  and  $R_2$  will need to satisfy

$$0 \leq \left(1 - \frac{L}{R_1}\right) \left(1 - \frac{L}{R_2}\right) \leq 1 \quad (2.23)$$

in order to be geometrically stable.

LIGO uses the frequency response of optical cavities for a number of reasons: Firstly, the round trip phase of the gravitational wave is amplified by the finesse (equation 2.18) of the 4 kilometer arm cavities, therefore increasing the sensitivity. Secondly, the input and output of the interferometer's Gaussian beam mode can be refined by only allowing the fundamental mode of the laser to resonate (input and output mode cleaners). Thirdly, Advanced LIGO uses a dual-recycled Michelson interferometer which means the symmetric

port has a mirror inserted to resonate the light reflected from the Fabry Perot arms (power recycling) and another mirror shapes the frequency response of the differential cavity pole at the anti-symmetric port (signal recycling).

### Achieving Resonance in an Optical Cavity

Described above are the theoretical constructs for a Fabry-Perot cavity, but the question remains, how does one practically construct a resonant optical cavity? The answer comes from using a heterodyne sensing scheme similar to the one described in Section 2.0.1. Except the optical system is not a Michelson interferometer but rather a two mirror cavity and can apply to a number of different geometries such as triangular or bow-tie cavities.

Starting with an input laser and EOM (electro-optical modulator) that imparts upper and lower sidebands at a modulation frequency  $\Omega$ , the user injects three beams into the optical system described in Equation 2.5. When placing a photodetector on the reflection port, one should see the cavity's effect on each of the three electric fields.

$$E_{FP,out} = E_C + E_{SB+} + E_{SB-} = \begin{pmatrix} r_C \\ r_{SB+} \\ r_{SB-} \end{pmatrix} \begin{pmatrix} E_{C,in} & E_{SB+,in} & E_{SB-,in} \end{pmatrix} \quad (2.24)$$

where the reflection coefficients follow equation 2.13. Because sidebands are frequency shifted, they will effectively *see* a different cavity than the carrier and the total phase accumulated by the two fields will be different. To make a good reference for the resonant carrier beam, the modulation frequency  $k_\Omega$ , is chosen such that sidebands are be anti-resonant which effectively means they are rejected from entering the cavity.

$$r_C = -r_1 + \frac{t_1^2 r_2 e^{-i2kL}}{1 - r_1 r_2 e^{-i2kL}} \quad (2.25)$$

and

$$r_{SB\pm} = -r_1 + \frac{t_1^2 r_2 e^{-i2(k+k_\Omega)L}}{1 - r_1 r_2 e^{-i2(k+k_\Omega)L}} \quad (2.26)$$

The formalism to read out the error signal is shown in Equation 2.10 where a photodetector in reflection (see Figure 2.5) reads out the sum of fields squared and demodulates to get the error signal which will be linearly proportional to the laser frequency and cavity length [9].

$$\text{Error Signal} \propto \frac{L\mathbb{F}}{\lambda} \left[ \frac{\delta w}{w} + \frac{\delta L}{L} \right] \quad (2.27)$$

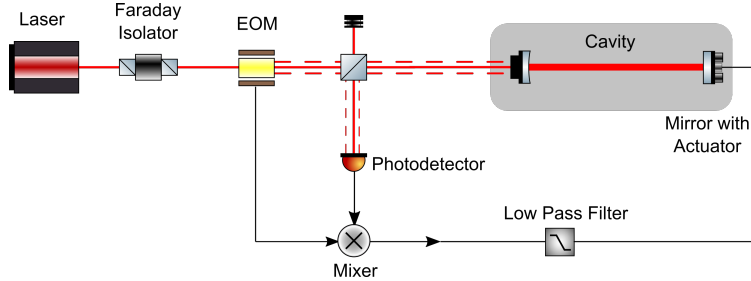
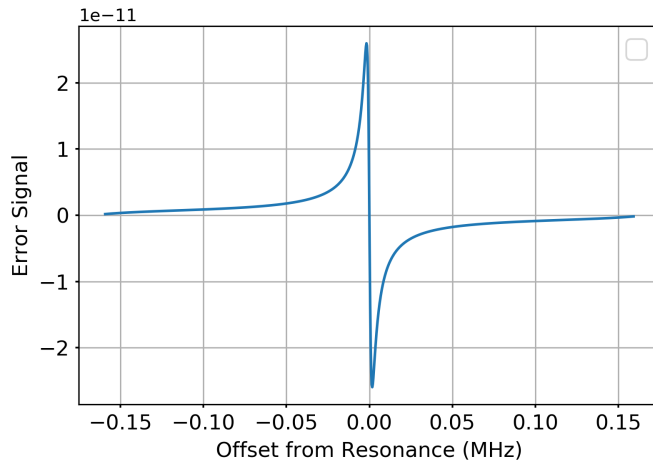


Figure 2.5: **Control scheme for an optical cavity.** The electric fields in reflection provide the error signal when mixed with the local oscillator and then gets low-passed for a DC signal to drive the end mirror which will control the length of the cavity, see Figure 2.6.

### 2.0.3 Fabry-Perot Michelson

Using an optical cavity to increase the number of bounces along the 4 kilometer arms will amplify the gravitational wave signal but it will also shape the frequency dependence of the sensitivity as well. This has already been alluded to in section 1.2 where the overall increase in arm length will tune the response function of equation 1.19. The same concept applies to integrating the use of Fabry-Perot arms with a Michelson interferometer and looking at the signal at the antisymmetric port as a function of gravitational wave frequency. Previously in section 2.0.1, it was shown that the heterodyne RF detection technique required beating the sidebands with a carrier field containing the gravitational wave information. However, this is not the only way because the signal sidebands beating with a reference carrier field could



**Figure 2.6: Pound-Drever-Hall (PDH) error signal in reflection of a Fabry Perot cavity.** By modulating the frequency (or length) close to the zero offset point, the error signal is linear. However, if the actuation is too far away from the lock point, the signal becomes highly non-linear. Which means the drive output must wait until the error signal comes close enough to zero before triggering on.

also be a valid way of measuring a signal of interest. In fact, Advanced LIGO employs a specific type of homodyne detection called DC readout [45][30]. The idea is that the carrier field will resonate in the arms but will be slightly modulated due to a gravitational wave which will create audio frequency sidebands imparted on the field.

Figure 2.7 shows an input electric field of  $E_0$  incident on a 50/50 beamsplitter which then enters two orthogonal arm cavities of length  $L_x$  and  $L_y$ . Notice that the distance from the beamsplitter to the input couplers for both arms is denoted by  $l_x$  and  $l_y$ , this is to account for the DARM offset which is analogous to the Schnupp asymmetry described in section 2.0.1. After partially transmitting and reflecting at the beamsplitter, the fields will resonate in each of the arm cavities and obey the reflectivity relations described by equation 2.13. Upon recombining at the beamsplitter, the antisymmetric port electric field will be related to the arm fields by,

$$E_{\text{AS}} = \frac{1}{\sqrt{2}}[E_x^{\text{ARM}} + E_y^{\text{ARM}}] \quad (2.28)$$

where  $E_i^{\text{ARM}} = E(\omega) \pm [E(+\omega_{\text{GW}}) + E(-\omega_{\text{GW}})] \sin k\delta l$  is the reflected fields for the x and y

arms which contain the carrier(first term) and GW signal sidebands(last two terms). In this case, the gravitational wave sidebands are a single frequency for simplicity but this analysis will work for all frequencies spanning the LIGO sensitivity band. The antisymmetric port will only be sensitive to the differential motion between the arm cavities, which means the gravitational wave sidebands in the x-arm will be out of phase with the y-arm. Also it is important to note that inserting a DC microscopic length shift of a few picometers represented by  $\delta l = l_x - l_y$  allows for some carrier leakage field to propagate towards the antisymmetric port which creates the static reference to form a beat note with the signal sidebands. In practice, this is achieved by introducing a static offset between the x and y arm cavity lengths,  $L_x \neq L_y$ , this is referred to as a differential arm (DARM) offset.

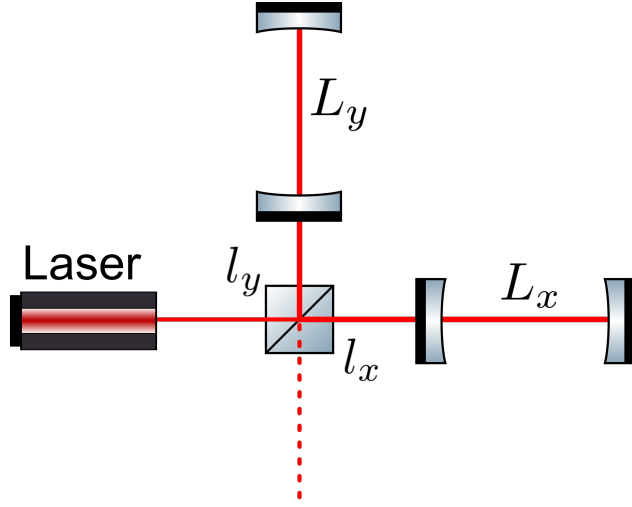


Figure 2.7: Michelson with Fabry Perot arms

For the carrier field, the amplitude of reflection is simple because the LIGO arms are a strongly over-coupled cavity operating on resonance therefore

$$E(\omega) = \frac{E_0}{\sqrt{2}} \left( -r_1 + \frac{t_1^2 r_2}{1 - r_1 r_2} \right) \approx -\frac{E_0}{\sqrt{2}} \quad (2.29)$$

The sidebands are a different story because the modulation caused by the gravitational wave slightly moves the field off resonance. Imagine the carrier circulating in the arms and then suddenly, a disturbance due to a gravitational wave differentially displaces the

end mirrors at a frequency  $\omega_{\text{GW}}$  by an amount  $\Delta L_-$ . By using the same formalism as the expansion of a modulated field in equation 2.5, the sideband fields can be described by,

$$\begin{aligned} E(\pm\omega_{\text{GW}}) &= \left[ \frac{t_1}{1 - r_1 r_2 e^{-2ikL_+}} \right] \frac{E_0}{\sqrt{2}} \left[ \frac{t_1}{1 - r_1 r_2 e^{-2i(kL_+ \pm \omega_{\text{GW}} \frac{L_\pm}{c})}} \right] ik\Delta L_- \\ &= \left[ \frac{t_1^2}{1 - r_1 r_2} \right] \frac{E_0}{\sqrt{2}} \left[ \frac{1}{1 - r_1 r_2 e^{\pm 2i\omega_{\text{GW}} \frac{L_\pm}{c}}} \right] ik\Delta L_- \end{aligned} \quad (2.30)$$

The first bracket is the circulating field of the carrier signal amplified by the Fabry Perot cavity and the second bracket is the circulating field slightly off resonance due to the gravitational wave frequency offset. Notice that the static arm length is denoted by  $L_+ = \frac{L_x + L_y}{2}$ , which refers to the common arm length for the two Fabry-Perot arms. Setting the fields to resonate already simplifies the equation but it is also reasonable to approximate the gravitational wave as a weak signal and expand the exponential  $e^{-2i\omega_{\text{GW}} \frac{L_\pm}{c}} \approx 1 - 2i\omega_{\text{GW}} \frac{L_\pm}{c}$ . This transforms the signal sideband field into a simpler form,

$$E(\pm\omega_{\text{GW}}) \approx \left[ \frac{t_1}{1 - r_1 r_2} \right]^2 \frac{E_0}{\sqrt{2}} \left[ \frac{1}{1 \pm i\frac{\omega_{\text{GW}}}{\omega_p}} \right] ik\Delta L_- \quad (2.31)$$

where  $\omega_p = \frac{1 - r_1 r_2}{r_1 r_2} \frac{c}{2L_+}$  is the differential pole frequency; notice that it matches the single arm cavity pole so a Fabry-Perot Michelson interferometer has the same frequency dependence.

The photodiode signal at the antisymmetric port is proportional to the beat note between the carrier and signal sideband in the audio frequency band with a demodulation phase  $\phi_D$ ,

$$\begin{aligned} S &\propto 2[E(\omega)E^*(-\omega_{\text{GW}}) + E(-\omega_{\text{GW}})E^*(\omega)] \sin(k\delta l) \sin(\phi_D) \\ &\propto E_0^2 \frac{8\pi L_+}{\lambda} \left[ \frac{t_1}{1 - r_1 r_2} \right]^2 \left[ \frac{1}{1 - i\frac{\omega_{\text{GW}}}{\omega_p}} \right] \sin(k\delta l) \sin(\phi_D) h_{\text{GW}} \end{aligned} \quad (2.32)$$

where the length disturbance  $\Delta L_-$  was transformed to originate from a gravitational wave signal  $k\Delta L_- = \frac{2\pi L_-}{\lambda} h_{\text{GW}}$ . The response of this particular interferometer to differential arm length motion is linearly proportional to the gravitational wave amplitude as well as the input power  $P_0 \propto E_0^2$ , but there is also a frequency dependent component which is the same

as a single Fabry-Perot cavity. This acts like a low pass filter above the corner frequency colloquially called the DARM cavity pole. By adding resonators, there is also a DC amplification of the signal by a factor of  $\left[\frac{t_1}{1-r_1r_2}\right]^2$ , which is the gain of a linear Fabry-Perot cavity ( $\approx 268$  for Advanced LIGO optics [27]).

#### 2.0.4 Power-Recycled Fabry-Perot Interferometers

If the interferometer is operating such that the intensity at the antisymmetric port is close to null, conservation of energy requires that the arm powers will reflect back towards the input laser. Fritschel et al [46] [43] showed the effects of adding a partially reflecting mirror increases the Michelson optical gain for both the sideband and carrier fields. Section 2.0.3 showed that the Michelson interferometer with Fabry Perot arms can be represented by a single cavity response. Therefore it is useful to model a power recycled interferometer by using a coupled cavity approach where one of the mirrors is replaced with the total reflected field of the Fabry-Perot Michelson on a bright fringe. Here the reflectivity and transitivity of the power recycling mirror (PRM) is denoted by  $r_p$  and  $t_p$ , respectively.

In this configuration, the effective length of the cavity is the average path between the power recycling mirror and the high reflectivity surfaces of the input test masses,

$$l_{\text{PRC}} = l_p + \frac{l_x + l_y}{2} \quad (2.33)$$

The circulating power in the cavity is given by equation 2.15 but uses the reflectivity of arm cavities,

$$E_{\text{PRC}} = \frac{t_p}{1 - r_p r_{\text{FPM}} e^{-2ikl_{\text{PRC}}}} E_{\text{in}} \quad (2.34)$$

where  $r_{\text{FPM}} \approx 1 - \frac{\mathbb{F}}{\pi} \mathcal{L}_{\text{ARM}}$  for high finesse ( $\mathbb{F}$ ) arm cavities and the round trip arm losses are denoted by  $\mathcal{L}_{\text{ARM}}$ . This is a valid approximation for the advanced LIGO since their values for arm finesse can be around 450 or higher depending on the losses. This means the

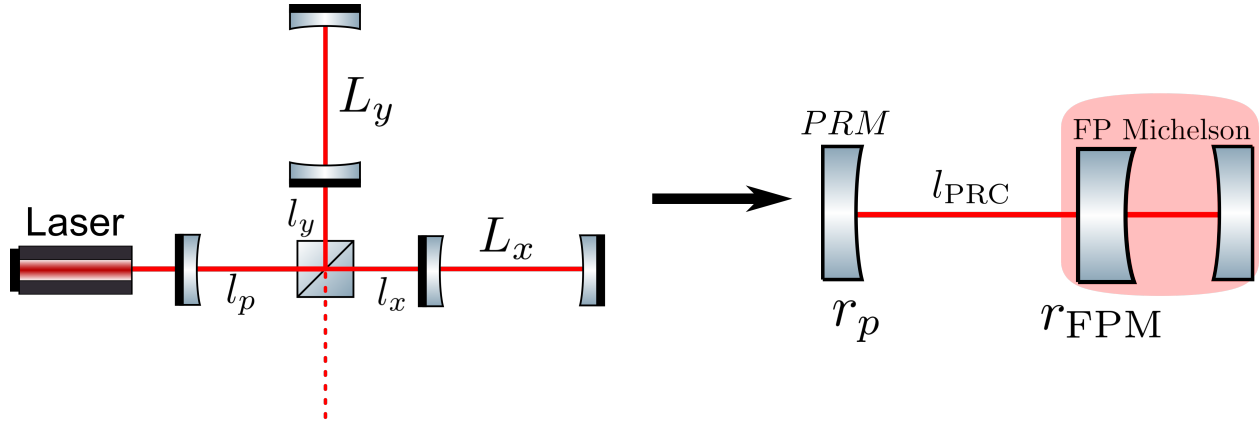


Figure 2.8: **A power recycled Fabry-Perot interferometer.** Adding a mirror at the symmetric port forms another resonator called the power recycling cavity (PRC) where the distance between from the power recycling mirror (PRM) to the beamsplitter is denoted by  $l_p$  and the reflectivity is  $r_p$ . The interferometer usually operates with the symmetric port on the bright fringe and the reflection from a Fabry-Perot Michelson can be represented by a single reflectivity,  $r_{\text{FPM}}$  while the length  $l_{\text{PRC}}$  is the average distance from PRM to the ITMs. This model makes handling the mathematics of a coupled cavity much more tangible.

circulating power in the recycling cavity while on resonance can be expressed by

$$P_{\text{PRC}} = \frac{1 - r_p^2}{\left[1 - r_p(1 - \frac{F}{\pi} \mathcal{L}_{\text{ARM}})\right]^2} P_{\text{in}} \quad (2.35)$$

By taking the derivative with respect to  $r_p$  and setting to zero, the optimal power recycling tuning is linearly proportional to the round trip loss,

$$r_{\text{opt}} = 1 - \frac{F}{\pi} \mathcal{L}_{\text{ARM}} \quad (2.36)$$

so it important to keep the arm cavity losses as low as possible and this also limits the ability to increase the finesse.

Adding a power recycling mirror will be equivalent to introducing higher power into the arm cavities but it will not shape the gravitational wave sideband frequency dependence in any other way. This can be reasoned qualitatively by imagining the signal sidebands that

get created in the arm cavities and propagate to the beam splitter where they will combine, however, the stretching and squeezing from the gravitational wave pattern will make the x-arm shorter while lengthening the y-arm and vice versa. This makes the anti-symmetric port transmissive to the signal sidebands but the carrier field which mostly gets reflected to the symmetric port will see the power recycling amplification. This means the beat note between the static carrier field and gravitational wave signal for a power recycled Fabry-Perot interferometer is

$$S_{\text{PRFP}} \propto E_0^2 \frac{8\pi L_+}{\lambda} \sqrt{g_{\text{PRC}}} \left[ \frac{t_1}{1 - r_1 r_2} \right]^2 \left[ \frac{1}{1 - i \frac{\omega_{\text{GW}}}{\omega_p}} \right] \sin(k\delta l) \sin(\phi_D) h_{\text{GW}} \quad (2.37)$$

where  $g_{\text{PRC}} = P_{\text{PRC}}/P_{\text{in}}$  is the power recycling gain.

### 2.0.5 Dual-Recycled Fabry-Perot Interferometers

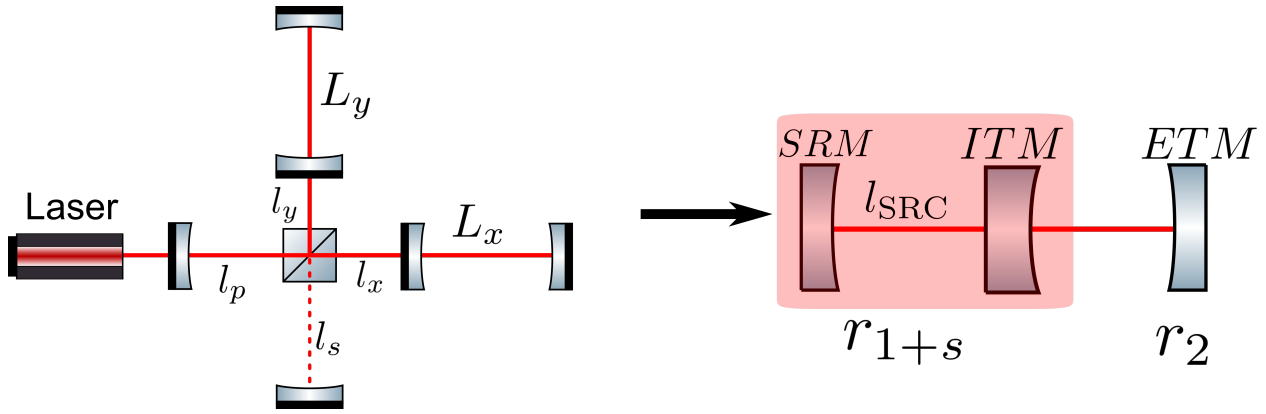


Figure 2.9: **A dual recycled Fabry-Perot interferometer.** The left diagram is similar to Figure 2.8 but with a signal recycling mirror (SRM) placed at the anti-symmetric port a distance  $l_s$  away from the beamsplitter. Similar to the analysis done when adding power recycling, collapsing the SRM and ITM into a single mirror system that has one reflectivity,  $r_{1+s}$  and an average length  $l_{\text{SRC}} = (l_s + \frac{l_x + l_y}{2})$  will simplify the coupled cavity picture. The round trip phase of the SRC will effectively increase or decrease  $r_{1+s}$  which will shape the frequency dependence of the interferometer's optical gain for gravitational-wave sidebands.

One of the biggest changes made between initial and advanced LIGO was the addition of

a signal recycling mirror at the antisymmetric port (see Figure 2.9 ). In the previous section, it was shown that the gravitational wave sensitivity was improved by adding a power recycling cavity to increase the effective input power entering the arm cavities. Adding another partially reflecting optic called the signal recycling mirror (SRM) at the antisymmetric port to create a resonant cavity will shape the interferometer’s response to gravitational waves. This allows for some flexibility in optimizing the instrument for specific sources such as binary neutron stars, but it also creates a more broadband response at higher frequencies while allowing the arm cavity finesse and/or power recycling to impart more power.

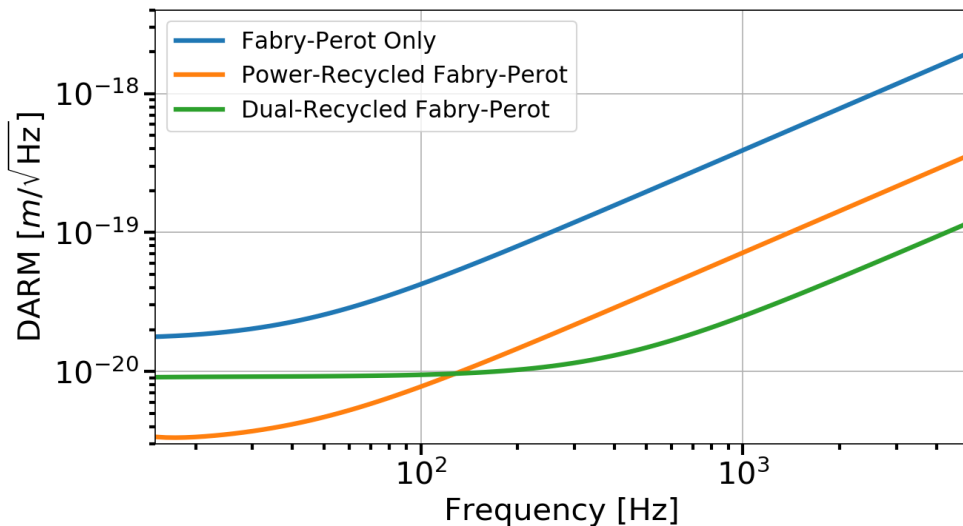


Figure 2.10: **Comparing the shot noise limited differential arm spectra for different interferometer configurations.** Here, the simulation was ran with FINESSE [69] using the advanced LIGO optical parameters [12].

A nice way to model the effect of signal recycling on the gravitational wave sidebands is to combine the SRM and arm cavity input test mass to create a combined mirror that is dependent on the round trip phase,  $\phi_s$  of the signal recycling cavity. The SRM will have a reflectivity and transmissivity equal to  $r_s$  and  $t_s$ , respectively, so the combined mirror will have a reflectivity and transmissivity equal to

$$r_{1+s} = \frac{r_1 - r_s e^{-2i\phi_s}}{1 - r_1 r_s e^{-2i\phi_s}} \quad (2.38)$$

$$t_{1+s} = \frac{t_1 t_s e^{i\phi_s}}{1 - r_1 r_s e^{-2i\phi_s}} \quad (2.39)$$

where  $\phi_s = k(l_s + \frac{l_x + l_y}{2}) = k l_{\text{SRC}}$  is the average signal recycling length. Plugging this into equation 2.30 in place of the input test mass reflectivity shows that the cavity pole is directly affected by the signal recycling properties, namely, the SRM reflectivity and the microscopic detuning of the length. The field propagating to the true antisymmetric port is in transmission of the signal recycling cavity which is accounted for with the last bracketed term.

$$\begin{aligned} E_{\text{AS}}(\pm\omega_{\text{GW}}) &= \left[ \frac{t_1^2}{1 - r_1 r_2} \right] \frac{E_0}{\sqrt{2}} \left[ \frac{1}{1 \pm r_{1+s} r_2 e^{-2i\omega_{\text{GW}} \frac{L_+}{c}}} \right] \left[ \frac{t_1 t_s e^{i\phi_s}}{1 - r_1 r_s e^{-2i\phi_s}} \right] i k \Delta L_- \\ &\propto \left[ \frac{\text{Constant}}{1 \pm 2i \frac{r_{1+s} r_2}{1 - r_{1+s} r_2} \omega_{\text{GW}} \frac{L_+}{c}} \right] \\ &\propto \left[ \frac{\text{Constant}}{1 \pm i\omega_{\text{GW}} / \omega_{\text{DR}}} \right] \end{aligned} \quad (2.40)$$

Here, the frequency dependence of the differential cavity pole with dual recycling is denoted by

$$\begin{aligned} \omega_{\text{DR}} &= \frac{1 - r_{1+s} r_2}{r_{1+s} r_2} \frac{c}{2L_+} \\ &= \frac{1 - r_1 r_s e^{-2i\phi_s}}{(r_1 - r_s e^{-2i\phi_s}) r_2} - 1 \end{aligned} \quad (2.41)$$

The carrier field will also see a gain from the signal recycling cavity equal to

$$\sqrt{g_{\text{SRC}}} = \frac{t_s}{1 + r_s r_{\text{FPM}} e^{-2i\phi_s}} \quad (2.42)$$

It is clear from the equations above that the gravitational wave sideband and carrier fields will see the signal recycling cavity effects differently and the responses are highly sensitive to the length detuning of  $\phi_s$ . Putting all the pieces together to get the dual recycled Fabry-Perot interferometer response to gravitational waves,

$$S_{\text{DRFP}} \propto E_0^2 \frac{8\pi L_+}{\lambda} \sqrt{g_{\text{PRC}}} \sqrt{g_{\text{SRC}}} g_{\text{ARM}} \left[ \frac{1}{1 - i \frac{\omega_{\text{GW}}}{\omega_{\text{DR}}}} \right] \sin(k\delta l) \sin(\phi_D) h_{\text{GW}} \quad (2.43)$$

The previous sections only considered the effect of Fabry-Perot cavities and recycling mirrors at the antisymmetric port (AS) due to the differential length change (DARM) of the 4 kilometer arms but the Advanced LIGO interferometer has a few lengths which are actively controlled. The other degrees of freedom include the common arm length (CARM), the power recycling length (PRCL), and signal recycling length (SRCL). These signals are sensitive at ports other than AS, such as in reflection of PRM (REFL) and a pick off port in the power recycling cavity (POP). A good reference for what signals are expected at these important readout points can be found in [55] [56] [57].

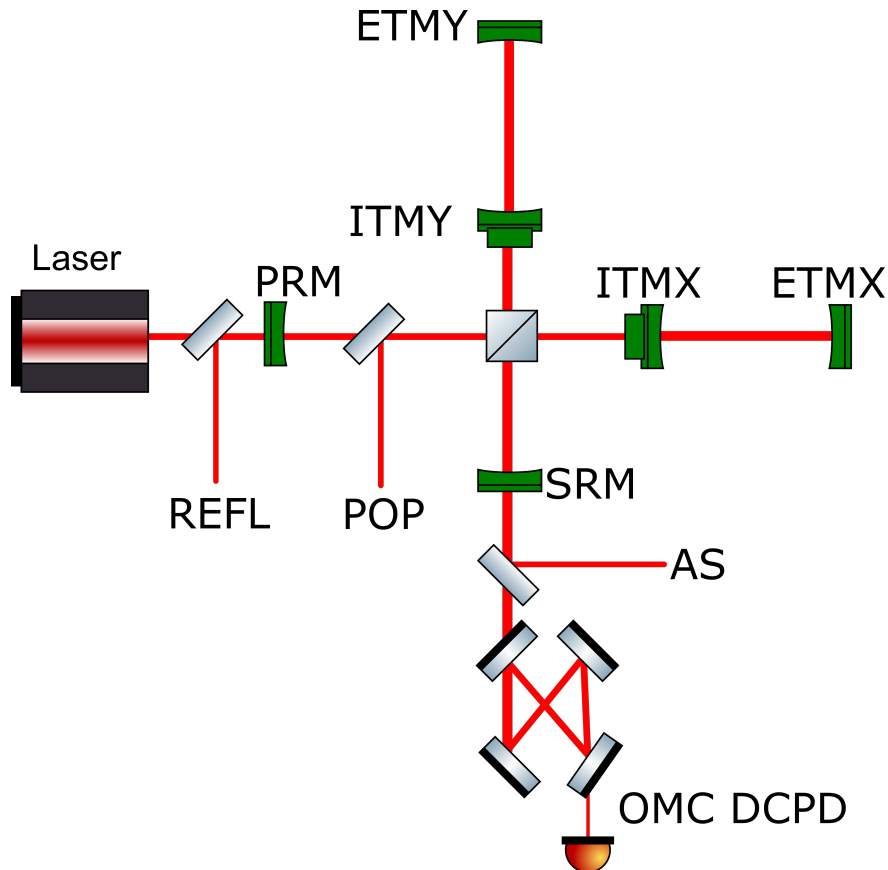


**Figure 2.11: Important sensor ports for Advanced LIGO** The green optics are used to distinguish the main interferometer mirrors from pick off mirrors which sense various degrees of freedoms for sensing and controls.

### 2.0.6 Fundamental Noise Sources

The preceding sections described ways to increase the response of LIGO to gravitational waves; equally as important is the science of characterizing and reducing the noise contributions from everything that is not gravitational waves to optimize the sensitivity.

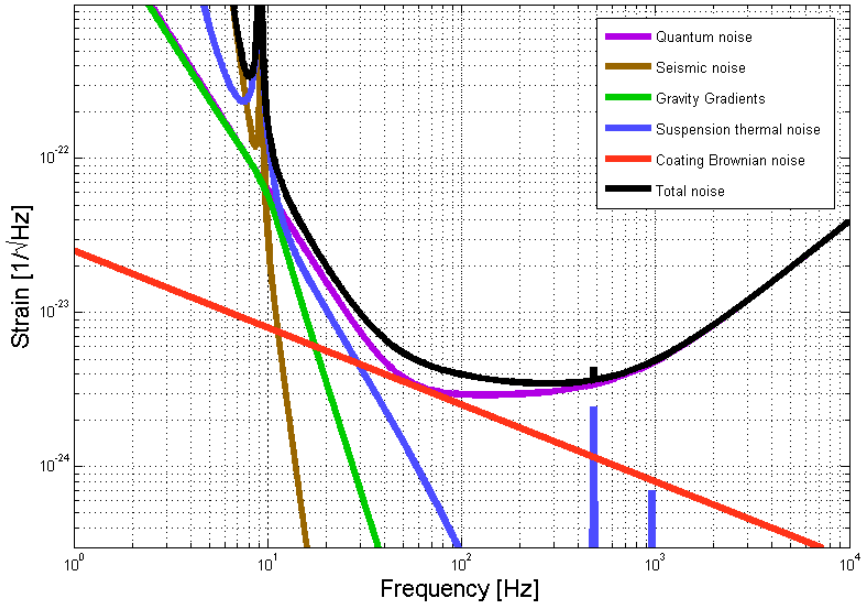


Figure 2.12: Noise budget from GWINC (Gravitational Wave Interferometer Noise Calculator)

#### Quantum Noise

Virtually all undergraduate quantum mechanics textbooks include a section on the harmonic oscillator [[81]]. A particularly interesting result when solving the Schrödinger equation using creation ( $\hat{a}^\dagger$ ) and annihilation ( $\hat{a}$ ) operators is the existence of a non-zero energy ground state which has variances in momentum and position related by the Heisenberg uncertainty principle. When it comes to electromagnetic fields, the pair associated with the uncertainty principle is the amplitude and phase of the laser beam.

As a result, one of the main noise sources that is limiting LIGO's sensitivity comes from the fluctuations of quantum vacuum entering the anti-symmetric port and coupling to the

input laser. A quantum mechanical description of an interferometer was constructed by Caves [21][22] [23], where he used electric field operators to show that vacuum fluctuations are the cause of radiation pressure and shot noise in a simple interferometer (no resonant cavities). The following analysis below will also be simplified in this way but is reasonably close in estimating the amount radiation pressure and shot noise. For studies that take into account more complicated interferometer configurations with resonant cavities, refer to Buonanno, Chen, and Kimble [19] [25] [58].

**Quantum states:** It is well known in physics [81] [49] that a solution to the quantum harmonic oscillator in the energy eigenbasis employs the annihilation and creation operators,  $\hat{a}^\dagger$  and  $\hat{a}$ , to factorize the Hamiltonian

$$\hat{H} = \hbar\omega(\hat{N} + 1/2) \quad (2.44)$$

where  $\hat{N} = \hat{a}^\dagger\hat{a}$  is the number operator. When using this formalism to create a coherent electromagnetic field, it is useful to define a unitary operator that displaces the vacuum state [47]:

$$\hat{D} \equiv \hat{D}(\alpha) \equiv \exp(\alpha\hat{a}^\dagger - \alpha^*\hat{a}) = e^{-\frac{|\alpha|^2}{2}} e^{\alpha\hat{a}^\dagger} e^{\alpha^*\hat{a}} \quad (2.45)$$

and has the properties,

$$\begin{aligned} \hat{D}(\alpha) &= \hat{D}^{-1}(\alpha) = \hat{D}(-\alpha) \\ \hat{D}^\dagger \hat{a} \hat{D} &= \hat{a} + \alpha \\ \hat{D}^\dagger \hat{a}^\dagger \hat{D} &= \hat{a}^\dagger + \alpha^* \end{aligned} \quad (2.46)$$

When applying the displacement operation on the vacuum state, the resultant vector has an amplitude  $\alpha$  and follows the same uncertainty distribution as an unperturbed vacuum vector as shown in Figure[StickandBall],

$$|\alpha\rangle = \hat{D}|0\rangle = e^{-\frac{|\alpha|^2}{2}} e^{\alpha\hat{a}^\dagger} |0\rangle \quad (2.47)$$

## Radiation Pressure

One might naively think that power fluctuations in the main laser causes radiation pressure effects on the test masses which will result in noise. However, if the 50/50 beamsplitter is perfect, then the momentum transfer to each test mass will result in a common length change and will not vary the intensity at the antisymmetric port (or the symmetric port for that matter). However, the baseline laser power will be important when considering a full quantum mechanical picture of radiation pressure.

Consider plane wave waves entering the interferometer from both the symmetric and anti-symmetric ports. This method is similar to the input-output methods of section 2.0.1, however, the difference being that the beamsplitter will couple the electric fields from the input laser and quantum vacuum.

The electric fields combine at the beamsplitter from both ports and add linearly,

$$E_x = \frac{1}{\sqrt{2}} \left[ iE_0 + E_{AS,in} \right] \quad (2.48a)$$

$$E_y = \frac{1}{\sqrt{2}} \left[ E_0 + iE_{AS,in} \right] \quad (2.48b)$$

where  $E_0$  is the input field from the laser and  $E_{AS,in}$  is the field from the anti-symmetric port. The electric fields will travel down each arm and strike the mirrors with intensities denoted by,

$$|E_x|^2 = \frac{1}{2} \left[ |E_0|^2 + |E_{AS,in}|^2 + i(E_0 E_{AS,in}^* - E_0^* E_{AS,in}) \right] \quad (2.49a)$$

$$|E_y|^2 = \frac{1}{2} \left[ |E_0|^2 + |E_{AS,in}|^2 - i(E_0 E_{AS,in}^* - E_0^* E_{AS,in}) \right] \quad (2.49b)$$

Therefore, differential momentum transfer between the two masses will be equal to the

differences in intensities between the two arms:

$$\begin{aligned}\mathbf{P} &= \frac{2\hbar\omega}{c} \left( |E_x|^2 - |E_y|^2 \right) \\ &= \frac{2\hbar\omega}{c} \left( E_0 E_{AS,in}^* - E_0^* E_{AS,in} \right) \\ \Rightarrow \hat{\mathbf{P}} &= \frac{2\hbar\omega}{c} \left( \hat{a}_1^\dagger \hat{a}_2 - \hat{a}_2^\dagger \hat{a}_1 \right)\end{aligned}\quad (2.50)$$

The last part of equation 2.50 replaces the classical electric fields with creation and annihilation operators for the symmetric input mode ( $\hat{a}_1^\dagger, \hat{a}_1$ ) and antisymmetric input mode ( $\hat{a}_2^\dagger, \hat{a}_2$ ) modes. Recall that there is a well established convention denoting the wave function of the two dimensional modes of the quantum harmonic oscillator [47],  $|\alpha, \beta\rangle$ , where  $\alpha$  denotes the input symmetric mode and  $\beta$  refers to the input antisymmetric mode:

$$|\alpha, 0\rangle = \hat{D}_1(\alpha) |0, 0\rangle \quad (2.51)$$

The interesting results arising from this formulation is the expectation value turns out to be null,

$$\langle \hat{\mathbf{P}} \rangle = \langle \alpha, 0 | \hat{\mathbf{P}} | \alpha, 0 \rangle = 0 \quad (2.52)$$

However, the variance of the momentum transfer is non-zero,

$$\begin{aligned}\Delta \mathbf{P}^2 &= \langle \hat{\mathbf{P}}^2 \rangle - \langle \hat{\mathbf{P}} \rangle^2 \\ &= \left( \frac{2\hbar\omega}{c} \right)^2 \langle \alpha, 0 | \hat{a}_1^\dagger \hat{a}_2 \hat{a}_1 \hat{a}_2^\dagger + \hat{a}_2^\dagger \hat{a}_1 \hat{a}_2 \hat{a}_1^\dagger - \hat{a}_2^\dagger \hat{a}_1 \hat{a}_1 \hat{a}_2^\dagger - \hat{a}_1^\dagger \hat{a}_2 \hat{a}_2 \hat{a}_1^\dagger | \alpha, 0 \rangle \\ &= \left( \frac{2\hbar\omega}{c} \right)^2 |\alpha|^2\end{aligned}\quad (2.53)$$

For some time interval  $\Delta T$ , the input laser power consisting of  $\langle N \rangle = |\alpha|^2$  photons is

$$P_{in} = \frac{\hbar\omega}{\Delta T} |\alpha|^2 \quad (2.54)$$

To solve for the amplitude spectral density of the displacement, Newton's second law can be applied in the frequency domain

$$M(2\pi f)^2 \tilde{x}(f) = \tilde{F}(f) = \frac{\Delta \mathbf{P}}{\Delta T} \quad (2.55)$$

Here, the quantum radiation force spectrum,  $\tilde{F}(f)$ , is actually flat in frequency because the impacting photons have a randomly distributed amplitude but this gives a straightforward pathway to calculate the displacement spectrum ,

$$\tilde{x}_{RP}(f) = \sqrt{\frac{\hbar\omega}{\Delta T} P_{\text{in}}} \frac{1}{2Mc(\pi f)^2} \quad (2.56)$$

This means the noise spectral density of radiation pressure for an interferometer with a mirror of mass  $M = 40$  kg, input power  $P_{\text{in}} = 125$  Watts, and laser frequency  $\lambda = 1064$  nm

$$\tilde{h}_{RP}(f) = 2.04 \times 10^{-20} \frac{1}{f^2} \left[ \frac{\text{Strain}}{\sqrt{\text{Hz}}} \right] \quad (2.57)$$

So it is shown that the contribution of quantum radiation pressure in a simple interferometer increases with the square root of the input power.

### Shot Noise

Another way that quantum fluctuations at the antisymmetric port can vary the sensitivity is by adding phase noise. Imagine holding the test masses rigidly such that the only effects on the output light is due to a phase change in the laser light in the arms. By using the same formulation for radiation pressure but propagating the fields back to the beam splitter, equations 2.48 will have extra phase that depends on the arm lengths are denoted by  $l_x$  and  $l_y$  in a simple Michelson interferometer,

$$E_{x,\text{out}} = \frac{1}{\sqrt{2}} \left[ iE_0 + E_{AS,\text{in}} \right] e^{-i2kl_x} \quad (2.58a)$$

$$E_{y,\text{out}} = \frac{1}{\sqrt{2}} \left[ E_0 + iE_{AS,\text{in}} \right] e^{-i2kl_y} \quad (2.58b)$$

Therefore the antisymmetric port field is described by

$$\begin{aligned} E_{AS,\text{out}} &= \frac{1}{\sqrt{2}} (E_{x,\text{out}} + iE_{y,\text{out}}) \\ &= ie^{-ikl_x - ikl_y} [\cos(\Delta\phi)E_0 - \sin(\Delta\phi)E_{AS,\text{in}}] \end{aligned} \quad (2.59)$$

where  $\Delta\phi = k(l_x - l_y)$  is used for brevity. The intensity is once again found by squaring the electric field,

$$\begin{aligned} \mathbf{I}_{AS,\text{out}} &= |E_{AS,\text{out}}|^2 \\ &= \left[ \cos^2(\Delta\phi)|E_0|^2 + \sin^2(\Delta\phi)|E_{AS,\text{in}}|^2 - \sin(\Delta\phi)\cos(\Delta\phi)[E_0E_{AS,\text{in}}^* + E_0^*E_{AS,\text{in}}] \right] \\ \Rightarrow \hat{\mathbf{I}}_{AS,\text{out}} &= \left[ \cos^2(\Delta\phi)a_1^\dagger a_1 + \sin^2(\Delta\phi)a_2^\dagger a_2 - \sin(\Delta\phi)\cos(\Delta\phi)[a_1^\dagger a_2 + a_2^\dagger a_1] \right] \end{aligned} \quad (2.60)$$

The expectation value for the intensity using an input coherent laser with  $\alpha$  and quantum vacuum input at the antisymmetric port is

$$\begin{aligned} \langle \hat{\mathbf{I}} \rangle &= \langle \alpha, 0 | \hat{\mathbf{I}}_{AS,\text{out}} | \alpha, 0 \rangle \\ &= \cos^2(\Delta\phi)|\alpha|^2 \end{aligned} \quad (2.61)$$

which matches the classical description of a Michelson output described in section 2.0.1. Following the same methods to calculate the radiation pressure, photon number variance is

$$\begin{aligned} \Delta \mathbf{I} &= \sqrt{\langle \hat{\mathbf{I}}^2 \rangle - \langle \hat{\mathbf{I}} \rangle^2} \\ &= |\alpha| [\cos^2(\Delta\phi)] \end{aligned} \quad (2.62)$$

In order to cast the variance into an expected phase noise, consider the derivative of the

intensity with respect to the phase and plugging in the input power,

$$\frac{\partial I}{\partial \phi} = -2|\alpha|^2 \cos(\Delta\phi) \sin(\Delta\phi) \quad (2.63)$$

$$\delta\phi = \sqrt{\frac{\hbar\omega}{P_{\text{in}}}} \cot(\Delta\phi) \quad (2.64)$$

Here  $\delta\phi$  is the microscopic change in phase due to shot noise, whereas  $\Delta\phi$  is the DC offset in the arm lengths to begin with. So in general, the shot noise contribution is dependent on the amount of light present at the anti-symmetric port and this will vary depending on what type of signal readout scheme is implemented. To calculate the shot noise sensitivity, the phase shift in shot noise can be scaled by a factor of  $\frac{\lambda}{2\pi} \frac{1}{L}$  where  $\lambda$  is the laser wavelength and  $L$  is the DC length of the Michelson arms,

$$\tilde{h}_{SN}(f) = 8.2 \times 10^{-22} \left[ \frac{\text{Strain}}{\sqrt{\text{Hz}}} \right] \quad (2.65)$$

Unsurprisingly, the shot noise is proportional to  $1/\sqrt{P_{\text{in}}}$  and the initial phase difference between the interferometer arms. There are a few subtleties associated with measuring shot noise, this model assumes that the interferometer is a simple Michelson and the readout is a single photodetector located at the antisymmetric port. As shown in section 2.0.5, there is freedom to choose the readout scheme of the interferometer (heterodyne or homodyne) which will also affect the overall quantum sensitivity and introducing Fabry-Perot cavities will shape the shot noise for frequencies above the differential cavity pole in equations 2.31 and 2.41.

## Seismic Noise

The main contributions to seismic noise are primarily caused by either natural occurrences (tectonic plates, wind driven microcosms, oceanic storms etc) or man-made disturbances (heavy automotive traffic, industrial machinery, etc) which contribute to the background hum

of motion. Table 2.1 shows the large In general, this will be the low frequency barrier for all terrestrial gravitational-wave detectors. One of the biggest upgrades from eLIGO to aLIGO was the increase in complexity for seismic isolation and suspensions. Using multiple stages of actively controlled platforms [63] [64] [65][4], the noise contribution can be attenuated for frequencies larger than 1Hz; in addition, the use of quadruple pendulums to hang the main arm cavity optics further reduces the motion above the pendulum's resonance frequency[32][10]. This is a tremendous upgrade from the mostly passive isolation methods used in initial LIGO. An interesting point to note is that the estimate of noise contributions from seismic activities to the strain sensitivity is negligible for frequencies above 10 Hz, but absolutely vital for lock acquisition and resonator stability [90] [44].

Frequency Band	Causes
0.03 - 0.10 Hz	Wind and EQs
0.10 - 0.30 Hz	Wave driven micro-seismic motion
3.00 - 10.0 Hz	Anthropogenic and trucks

Table 2.1: **Frequency bands of common seismic noise at LHO.**

## Thermal Noise

Brownian motion [36] is the random movement of particles suspended in a fluid. The LIGO test masses that make up the 4 kilometer long Fabry-Perot cavities are large macroscopic objects but their constituent atoms can be excited by the ambient temperature which leads to random motion. Those atoms are interconnected which allow for the propagation of an infinite number of elastic wave modes that contain random relative phases and the linear superposition of the modes create distortions that result in thermal noise.

A good way to start analyzing thermal noise is to consider a simple harmonic oscillator with mass  $m$  that is in a thermal bath with a damping force,  $F = -b\dot{x}(t)$ :

$$\ddot{x}(t) + \gamma\dot{x}(t) + \omega_0^2x(t) = F/m \quad (2.66)$$

where  $\gamma = b/m$  and the force can be described by white noise. In this case,  $F$  represents work being done on the system by the external world, whereas the damping factor is the release of the system's energy to the outside world. By taking the Fourier transform, the equation of motion becomes

$$\tilde{x}(f) = \frac{\tilde{F}(f)}{m} \frac{1}{\omega^2 + i\gamma\omega + \omega_0^2} \quad (2.67)$$

This implies that the spectral density for viscous damping is

$$S_{\text{vis}} = \frac{S_F}{m^2} \frac{1}{(\omega^2 - \omega_0^2)^2 + (\gamma\omega)^2} \quad (2.68)$$

Because the noise is due to a thermal bath, the integrated power over all frequencies must satisfy this equation

$$\frac{1}{2} \int_{-\infty}^{\infty} S_{\text{vis}}(\omega) \frac{d\omega}{2\pi} = \frac{k_B T}{m\omega_0^2} \quad (2.69)$$

where  $k_B$  is the familiar Boltzmann's constant and  $T$  is the ambient temperature. Solving the integral and plugging the result for  $S_F$  back into the equation 2.68 gives the power spectrum for viscous damping,

$$S_{\text{vis}} = \frac{4k_B T \gamma}{m} \frac{1}{(\omega^2 - \omega_0^2)^2 + (\gamma\omega)^2} \quad (2.70)$$

This equation shows that for three different frequency regimes, the response can vary wildly,

$$\omega \ll \omega_0 \rightarrow S_{\text{vis}} = \frac{4k_B T}{m Q \omega_0^3} \quad (2.71a)$$

$$\omega \approx \omega_0 \rightarrow S_{\text{vis}} = \frac{4k_B T}{m \omega_0^3} Q \quad (2.71b)$$

$$\omega \gg \omega_0 \rightarrow S_{\text{vis}} = \frac{4k_B T}{m Q} \frac{\omega_0}{\omega^4} \quad (2.71c)$$

where  $Q = \omega_0/\gamma$  is commonly known as the quality factor of a resonator. Qualitatively,

this is directly proportional to the resonance height and its thinness. Figure 2.13 shows the resultant frequency dependent amplitude spectral density for a few different quality factors, for higher  $Q$  systems the amount of noise contribution from thermal noise is reduced at frequencies above the resonance. Another commonly used definition of the quality factor is the amount of energy loss per cycle, if the  $Q$  of a system is high, then the amount of energy loss per oscillation is very small and will take a longer time returning to equilibrium. A good description of the quality factor and its application to gravitational wave detectors can be found in section 7.5 of [75].

As system's mode number increases, the previous analysis becomes very difficult to solve analytically. However, the connection between a damped harmonic oscillator's energy loss and power spectrum can be described generically using the Fluctuation Dissipation Theorem,

$$S_x(f) = \frac{k_B T}{\pi^2 f^2} |\operatorname{Re}(Y(f))| \quad (2.72)$$

where  $Y(f)$  is the complex mechanical admittance (inverse of the impedance) of a system. The physical interpretation of equation 2.72 can be viewed as a tunnel of energy between a system of interest and the outside world. If there is an ability to couple energy from one system to another via some process, then the reverse must be true as well. This subtle but powerful statement can be applied generally. For example, a resistor which is able to dissipate thermal energy when current is flowing through it will convert random external temperature fluctuations into stray currents that results in *Johnson Noise*. Another principle which the FD theorem relies upon is that when the system is in thermal equilibrium, its response to fluctuations will be the same as applying a small force randomly.

Using this method, the mechanical admittance of a system is defined as  $Y(f) = \dot{x}(f)/F(f)$

which can be written down directly for a damped harmonic oscillator using equation 2.67,

$$\begin{aligned} \frac{\dot{x}(f)}{F} &= \frac{i\omega}{m} \frac{1}{\omega_0^2 - \omega^2 + i\gamma\omega} \\ &= \frac{i\omega}{m} \frac{(\omega_0^2 - \omega^2 - i\gamma\omega)}{(\omega_0^2 - \omega^2)^2 + (\gamma\omega)^2} \end{aligned} \quad (2.73)$$

and by plugging this into the fluctuation dissipation theorem, the power spectral density matches equation 2.70 for the viscous damping. To extend the usage further, consider the thermal noise from a solid which has some thermoelastic dissipation from an internal mode given by  $F_{diss} = -k(1 + \phi_L)x(t)$  where the phase term comes from the lag between applied force and the system's response to said force. By solving Newton's second law with this new damping term, the displacement spectrum becomes

$$\tilde{x}(f) = \frac{\tilde{F}}{m} \frac{1}{(1 + i\phi_L)\omega_0^2 - \omega^2} \quad (2.74)$$

Unlike the previous example of viscous damping, the integral for thermoelastic dissipation only holds for some frequency regime but implementing the fluctuation dissipation theorem leads directly to the noise power spectrum,

$$S_{TN}(f) = \frac{4k_B T \omega_0^2 \phi_L}{m\omega} \frac{1}{(\omega^2 - \omega_0^2)^2 + (\omega_0 \phi_L)^2} \quad (2.75)$$

The frequency response will also be different compared to viscoelastic dissipation,

$$\omega \ll \omega_0 \rightarrow S_{vis} = \frac{4k_B T}{mQ\omega\omega_0^2} \quad (2.76a)$$

$$\omega \approx \omega_0 \rightarrow S_{vis} = \frac{4k_B T}{m\omega_0^3} Q \quad (2.76b)$$

$$\omega \gg \omega_0 \rightarrow S_{vis} = \frac{4k_B T}{mQ} \frac{\omega_0^2}{\omega^5} \quad (2.76c)$$

The structural damping formalism can also be applied to the suspension fibers which hold the

40 kilogram test masses [48], [75] which yield a noise spectral density that contains resonances at a variety of frequencies. In Advanced LIGO, the violin modes and their harmonics could get rung up from earthquakes and saturate the output mode cleaner's DC photodiodes so they must be actively damped in order to obtain nominal low noise.

The largest contribution to the total thermal noise for current interferometers do not stem from viscous damping [77], thermoelastic damping of the substrate [75], or internal friction of the suspension fibers. The most dominant type of thermal noise is from the mechanical loss of the dielectric coatings [50] [39] which cause phase noise at the high reflectivity surface of the mirrors.

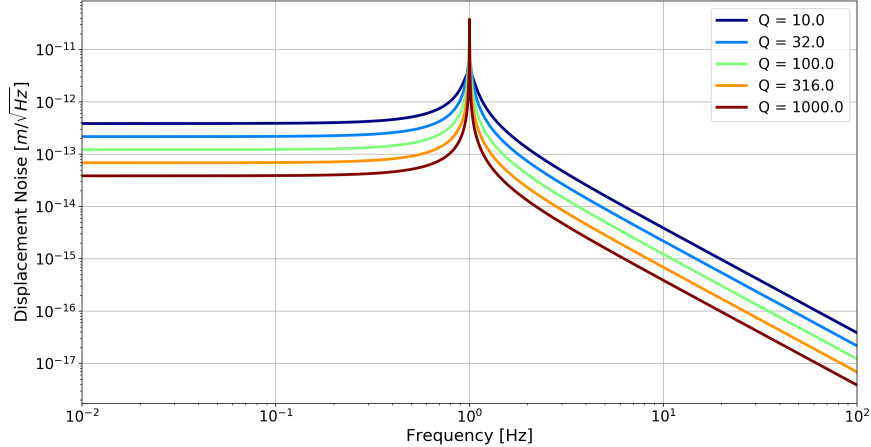


Figure 2.13: **Displacement spectrum for thermal noise.** By varying the resonance width of a system, the thermal noise at frequencies above the resonant peak will be decreased for higher Q's.

### Newtonian Noise

Described in the previous sections are noise sources which can be reduced using increasingly complicated techniques such as increased isolation stages for seismic or using squeezed states of light for quantum noise. However, for Newtonian noise caused by fluctuating gravitational fields from the wave motion of the ground cannot easily be reduced but possibly be measured

and fed-forward or subtracted off-line [33][76][54].

## 2.1 Mode Matching with Squeezed States of Light

In Section 2.0.6, the quantum limited sensitivity for a Michelson interferometer was shown to be composed of shot noise and radiation pressure. Although quantum fluctuations are a fundamental noise source, their effects can be modified by manipulating the vacuum state with correlated photons and injecting these states of light into the antisymmetric port of the interferometer. Within the LIGO community, this procedure of modifying quantum vacuum is called squeezing. The production of squeezed states with nonlinear devices is a well understood subject and was successfully tested in the sixth LIGO science run [28][29]. An extension of the formalism described in Section 2.0.6 was developed by Caves-Schumaker [22] which describes two-photon quantum optics and squeezing, but it is outside of the scope in terms of mode matching.

However, it is useful to understand the quantum noise in a way that scales the interferometer sensitivity in terms of the *Standard Quantum Limit* (SQL). The radiation pressure and shot noise add in quadrature to form the quantum noise and both are affected by the input power but inversely from each other as shown in 2.0.6. The SQL refers to the input power minimizes the total quantum noise and is the minimum achievable noise without squeezing. The radiation-pressure back-action coupling constant,  $\kappa$ , is given by [58]

$$\kappa = \frac{4P_0\omega_0}{mc^2f^2} \quad (2.77)$$

where  $P_0$  is the input power on the beamsplitter,  $\omega_0$  is the laser angular frequency,  $m$  is the optic mass, and  $f$  is the Fourier domain frequency. The SQL for a simple Michelson is given by [58],

$$S_{SQL} = \frac{4\hbar}{mL^2f^2} \quad (2.78)$$

With these two equations above, the total single-sided power spectral density for a simple Michelson is

$$S_{SM} = \frac{S_{SQL}}{2} \left( \frac{1}{\kappa} + \kappa \right) \quad (2.79)$$

Here the first term represents the shot noise while the second term is the radiation pressure contribution. Extending the Michelson quantum noise to the full Fabry Perot power recycled Michelson interferometer is essentially the same steps as Section 2.0.3, which showed that the gravitational wave signal became frequency dependent with respect to the cavity pole of the arms. In addition, adding a power recycling mirror was analogous to increasing the input power by a PRC gain factor. The coupling constant for this configuration is

$$\Upsilon = 2I_0 \frac{4\omega_0}{mL^2} \frac{1}{f^2(\gamma^2 + f^2)} \quad (2.80)$$

where  $\gamma = \frac{Tc}{2L}$  represents the cavity's full width half maximum and  $T$  is the input test mass transmissivity.

Modifying the field entering the antisymmetric port by replacing the quantum vacuum with a squeezed state has interesting effects on the strain sensitivity and reduces the noise floor below the standard quantum limit. The power spectral density for a power recycled Fabry Perot interferometer with injected squeezing is described by [58],

$$\begin{aligned} S_{PR} &= \frac{S_{SQL}}{2} \left( \frac{1}{\Upsilon} + \Upsilon \right) [\cosh 2R - \cos(2(\phi_s + \theta_s)) \sinh 2R] \\ &= \frac{S_{SQL}}{2} \left( \frac{1}{\Upsilon} + \Upsilon \right) e^{-2R} \quad \text{for } \theta_s = -\phi_s x \end{aligned} \quad (2.81)$$

where  $R$  is the squeeze factor,  $\theta_s$  is the squeeze angle, and  $\phi_s = \cot^{-1}(\Upsilon)$ . The squeeze angle can change the regime of strain which is affected, for example, when injecting for optimal shot noise reduction one would choose  $\theta_s = \pi/2$ . However, when trying to reduce the radiation pressure noise, then choosing  $\theta_s = 0$  is optimal. For the second line in the equation above, to achieve broadband squeezing, the squeeze angle must be rotated as a function of frequency.

Fortunately, this can be achieved by reflecting the squeezer beam off a filter cavity before injecting into the interferometer [68] [40]. Various configurations for squeezing is shown in Figure ???. The addition of optical losses play a large role in the interferometer sensitivity for a number of reasons:

1. The arm cavities and output optical train have associated losses which couple vacuum fluctuations and contribute shot noise. Generally, the former will have associated frequency dependence and be proportional to the round trip loss in the arm cavities.
2. A back-action coupling will also increase as a function of the round trip loss and contribute to the radiation pressure.
3. Vacuum fluctuations originating from the antisymmetric port of the interferometer will also add losses.
4. And finally, the squeezing degradation will be affected by the losses injected into the interferometer and mode matching.

An equation found in Kimble [58] can describe the first three points by defining the loss coefficient as  $\mathcal{L} = 2\mathcal{L}_{\text{ARM}}/T$  where  $\mathcal{L}_{\text{ARM}}$  is the round trip arm loss so the fractional power loss will be

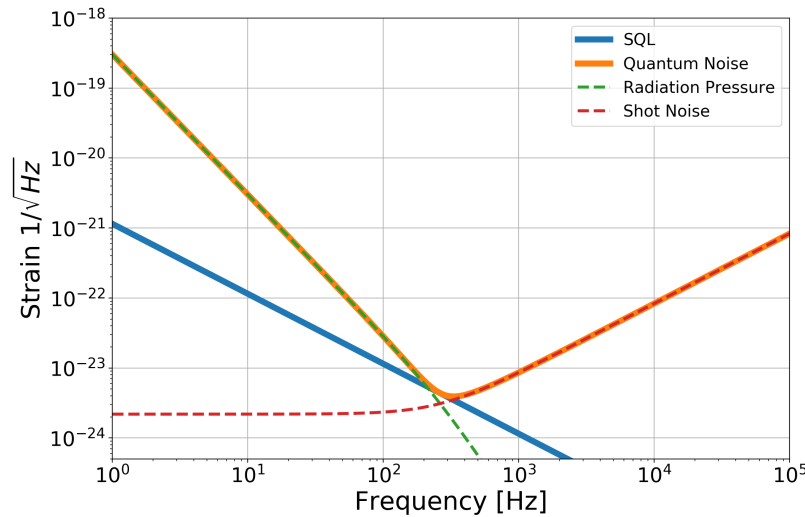
$$\varepsilon = \frac{2\mathcal{L}}{(1 + (f/\Upsilon)^2)} \quad (2.82)$$

which leads to a more complete equation for the quantum limited sensitivity with losses and optimal squeezing

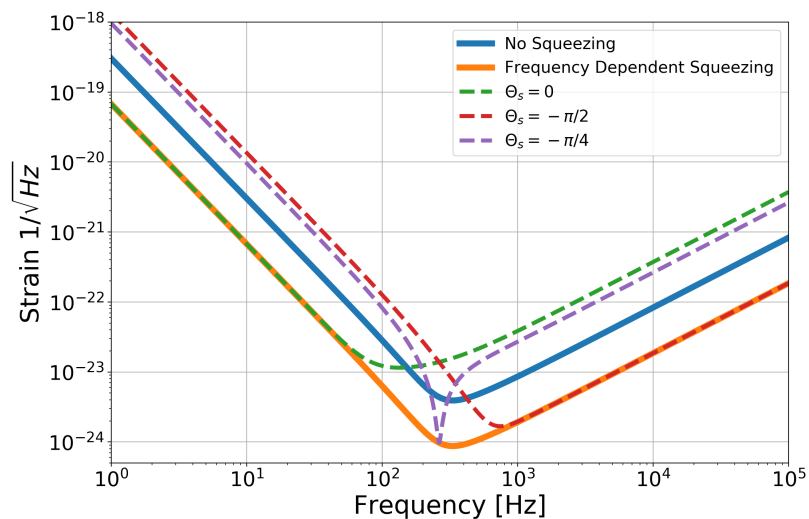
$$S_{\text{PR}_L} = \frac{S_{SQL}}{2} \left[ \frac{\varepsilon + \varepsilon_{OT}}{\Upsilon} + \frac{\mathcal{L}}{2} \Upsilon + \left(1 - \frac{1}{2}\varepsilon\right) \left(\frac{1}{\Upsilon} + \Upsilon\right) e^{-2R} \right] \quad (2.83)$$

Here,  $\varepsilon_{OT}$  represents losses from the interferometer optical readout train due to mode mismatch between the IFO and the output mode cleaner. The fourth point for optical losses is handled differently because it has to deal with mode mismatched coupling between the

squeezed light and the interferometer which reduces the effective squeezing level. It is shown in Chua's thesis [26] that quantum vacuum combines with the squeezed state through losses and forces the optical field variance back to the vacuum state, thereby degrading the squeezing benefits. By coupling the fundamental field that is squeezed to a combination of higher order modes, this will also act as a direct loss. Figure 1 of Dwyer et al [34] shows that squeezing efficacy depends strongly on total losses and the squeeze quadrature fluctuations. The details of mode mismatch will come in the next chapters but it is clear that reducing losses will play an important role for the operation of both a squeezed or non-squeezed interferometer.



(a) Power recycled Fabry Perot Michelson quantum noise



(b) Power recycled Fabry Perot Michelson quantum noise with various squeezing angles

# Chapter 3

## The Fundamentals of Mode-Matching

When dealing with the length sensing degrees of freedoms in Chapter ??, the plane wave approximation is sufficient for describing the resonator dynamics. However, when trying to understand the misalignment and mode mismatch signals, it is necessary to incorporate Gaussian beams and their associated higher order modes. This formalism plays a pivotal role in the LIGO detectors because the gravitational wave is sensed using the fundamental eigenmode of the arm cavities and any coupling to higher order modes results in a loss of signal at the antisymmetric port. Equally as important, the reduction of angular motion to remain locked relies on robust sensing of the cavity misalignment from external disturbances [44] and torque-to-angle coupling [82]. Mode matching is a second order effect but it will be shown in Chapter 6 that mismatches play an important role in the practical operation of a large scale interferometer.

### 3.1 Gaussian Beam Optics

To show that a Gaussian beam is a valid electromagnetic wave, consider the famous Maxwell's equations:

$$\begin{aligned}\nabla \times \mathbf{E} &= -\frac{\partial \mathbf{B}}{\partial t} \\ \nabla \cdot \mathbf{B} &= 0 \\ \nabla \times \mathbf{B} &= \mu \mathbf{J} + \frac{1}{c^2} \frac{\partial \mathbf{E}}{\partial t} \\ \nabla \cdot \mathbf{E} &= \frac{\rho}{\epsilon}\end{aligned}\tag{3.1}$$

Concentrating on the electric field in vacuum, we arrive at the Helmholtz Equation

$$(\nabla^2 + k^2)\mathbf{U}(\mathbf{r}, t) = 0\tag{3.2}$$

where  $k = \frac{2\pi\nu}{c}$  is the wave number and  $\mathbf{U}(\mathbf{r}, t)$  is the complex amplitude which can describe either the electric or magnetic fields. There are a variety of solutions to equation 3.2 which include the plane and spherical waves [74]. These two types of solutions are the extremes when considering the angle and spatial distribution as a function of propagation. The plane wave which has been used in chapter 1 is a beam whose rays have no variance in the spatial direction as it propagates through space, whereas the spherical wave starts at a point and spreads as a function of distance from the origin. Somewhere in between these two extrema is the paraxial wave which is a wave pattern that consists of rays at small angles relative to the direction of propagation. It is possible to express the paraxial solution to equation 3.2 as a plane wave with a modulated complex envelope  $\mathbf{A}(r)$ ,

$$\mathbf{U}(\mathbf{r}) = \mathbf{A}(\mathbf{r})e^{-ikz}\tag{3.3}$$

However, in order for the paraxial wave to exist,  $\mathbf{U}(r)$  must satisfy the Helmholtz equation. Alternatively, the  $\mathbf{A}(r)$  must satisfy a separate differential equation known as the paraxial Helmholtz Equation which can be derived explicitly by imposing constraints that force the

envelope to vary slowly with respect to the z-axis within the distance of one wavelength  $\lambda = 2\pi/k$ :

$$\left| \frac{\partial^2 \mathbf{A}}{\partial z^2} \right| \ll \left| k \frac{\partial \mathbf{A}}{\partial z} \right| \quad (3.4a)$$

$$\left| \frac{\partial^2 \mathbf{A}}{\partial z^2} \right| \ll \left| k \frac{\partial^2 \mathbf{A}}{\partial x^2} \right| \quad (3.4b)$$

$$\left| \frac{\partial^2 \mathbf{A}}{\partial z^2} \right| \ll \left| k \frac{\partial^2 \mathbf{A}}{\partial y^2} \right| \quad (3.4c)$$

The partial differential equation which arises is called the Paraxial Helmholtz Equation:

$$\nabla_T^2 A(r) - i2k \frac{\partial A(r)}{\partial z} = 0 \quad (3.5)$$

where  $\nabla_T^2 = \frac{\partial^2}{\partial x^2} + \frac{\partial^2}{\partial y^2}$  is the transverse Laplacian. A simple solution for equation 3.5 is the complex paraboloidal wave,

$$A(\mathbf{r}) = \frac{A_0}{q(z)} e^{\frac{-ikr^2}{2q(z)}}, \quad q(z) = z + iz_0 \quad (3.6)$$

The parameter  $z_0$  is referred to as the Rayleigh range and is directly proportional to the waist size squared. In order to separate the amplitude and phase portions of the wave, it is useful to rewrite  $q(z)$  as

$$\frac{1}{q(z)} = \frac{1}{R(z)} - i \frac{\lambda}{\pi W^2(z)} \quad (3.7)$$

Plugging equation 3.7 into 3.6 leads directly to the complex amplitude for a Gaussian Beam

$$U(r, z) = A_0 \frac{W_0}{W(z)} e^{-\frac{r^2}{W^2(z)}} e^{-ikz - ik\frac{r^2}{2R(z)} + i\zeta(z)} \quad (3.8)$$

where

$$W(z) = W_0 \sqrt{1 + \left( \frac{z}{z_0} \right)^2} \quad (3.9a)$$

$$R(z) = z \left[ 1 + \left( \frac{z}{z_0} \right)^2 \right] \quad (3.9b)$$

$$\zeta(z) = \tan^{-1} \left( \frac{z_0}{z} \right) \quad (3.9c)$$

$$W_0 = \sqrt{\frac{\lambda z_0}{\pi}} \quad (3.9d)$$

The Gaussian beams are named as such because of the intensity distribution,

$$I(r, z) = |U(r, z)|^2 = I_0 \left[ \frac{w_0}{w(z)} \right]^2 \exp \left[ \frac{-2r^2}{w^2(z)} \right] \quad (3.10)$$

where  $I_0 = |A_0|^2$  and has a peak at  $r = 0$  and  $z = 0$ . The width increases as the beam propagates along the  $\hat{z}$  axis away from the waist position and the intensity maximum on the beam axis decreases (see Figure 3.3),

$$I(0, z) = \frac{I_0}{1 + (z/z_0)^2} \quad (3.11)$$

### Hermite-Gauss Modes

The fundamental Gaussian beam is not the only solution which can be used to solve equation 3.5. In fact, there exists a complete set of solutions that can solve the paraxial Helmholtz Equation in rectangular coordinates, which are referred to as the Hermite Gauss modes

$$U_{mn}(x, y, z) = A_{mn} \left[ \frac{W_0}{W(z)} \right] \mathbb{G}_m \left( \frac{\sqrt{2}x}{W(z)} \right) \mathbb{G}_n \left( \frac{\sqrt{2}y}{W(z)} \right) \times \exp \left\{ -ikz - \frac{ik(x^2 + y^2)}{2R(z)} + i(m+n+1)\zeta(z) \right\} \quad (3.12)$$

where,

$$\mathbb{G}(u) = \mathbb{H}(u) \exp(-u^2/2) \quad (3.13)$$

and  $\mathbb{H}(u)$  are the well known Hermite polynomials. It is important to mention that the

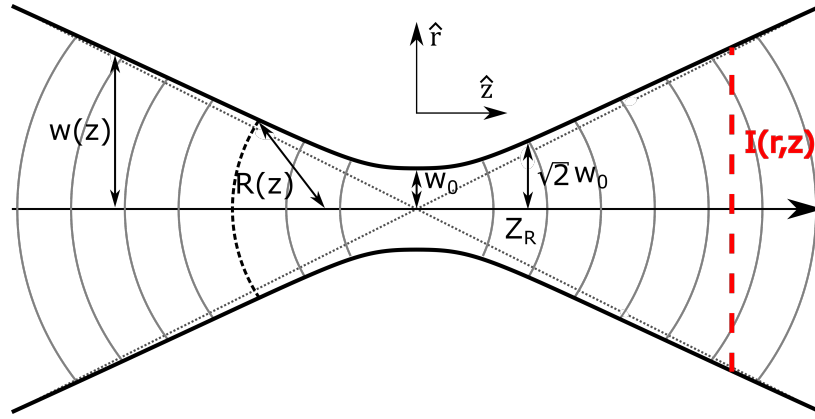


Figure 3.1: **A depiction of the Gaussian beam properties with respect to cylindrical coordinates.** Because the beam is axially symmetric, the two coordinates are denoted by  $\hat{r}$  for the radial and  $\hat{z}$  for the axis of propagation with the origin located at the center. The thick dark lines represent the beam size,  $w(z)$ , which is minimal at the waist,  $w(z) = w_0$  when  $z = 0$  and asymptotic towards  $\lambda/\pi w_0$  when  $z \approx \text{inf}$  as shown by the dotted gray lines. The red dashed line represents the intensity cross section of the beam which changes to a wider and flatter profile as a function of distance from the waist.

Gouy phase of the complex amplitude is different than the fundamental Gaussian beam by a factor of  $(m+n+1)$  and that the intensity distribution of these higher order modes are much different. Both of these facts will become extremely important in the following wavefront sensing discussion.

### Laguerre Modes

Another complete set of alternative solutions to equation 3.5 exists which are called the Laguerre-Gauss modes

$$V_{\mu\nu}(\rho, \theta, z) = A_{\mu\nu} \left[ \frac{W_0}{W(z)} \right] \mathbb{L}_\nu^\mu \left( \frac{\sqrt{2}x}{W(z)} \right) \times \exp \left\{ -ikz - \frac{ik\rho^2}{2R(z)} + i(\mu + 2\nu + 1)\zeta(z) \right\} \quad (3.14)$$

where  $\mathbb{L}_\nu^\mu \left( \frac{\sqrt{2}x}{W(z)} \right)$  is the Laguerre polynomial function. Both equations 3.12 and 3.14 are able to fully describe any complex electromagnetic amplitude; and because they both form complete sets, there is a rotation which can map from one basis to the other [7] [70]

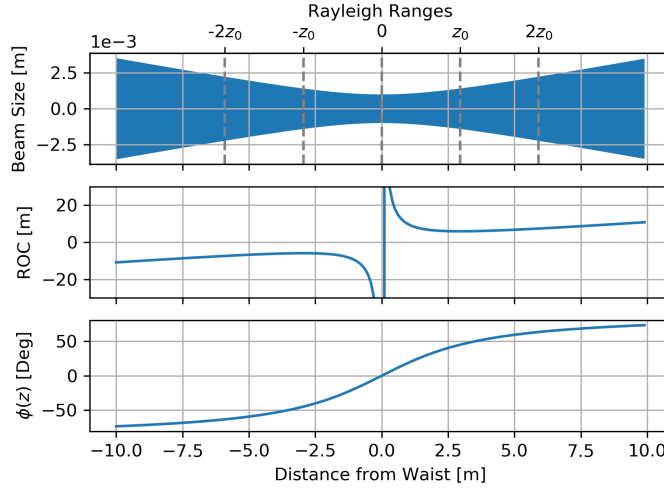


Figure 3.2: **Beam size, radius of curvature, and Gouy phase as a function of distance propagation from the waist.** The vertical dashed gray lines represent the integer number of Rayleigh ranges. At the point  $z = z_0$ , the beam size is  $\sqrt{2}$  of the waist size and the radius of curvature is minimal. At this point, the Gouy phase propagation is lagging the plane wave by  $\pi/4$  and the beam intensity is half of that at the waist.

$$U_{\mu\nu}^{LG}(x, y, z) = \sum_k^N i^k b(n, m, k) U_{N-k, k}^{HG}(x, y, z) \quad (3.15)$$

where

$$b(n, m, k) = \sqrt{\left(\frac{(N-k)!k!}{2^N n! m!}\right)} \frac{1}{k!} \frac{d^k}{dt^k} [(1-t)^m (1+t)^m]|_{t=0} \quad (3.16)$$

### 3.1.1 Misalignment and Higher Order Modes

Morrison and Anderson [6] [66] derived a simplistic way of how small misalignments and mode mismatch in cavities can couple the fundamental Gaussian beam into various higher order modes. This is done by taking a linear cavity and using its perfectly matched Gaussian beam as a reference, and then varying the input electric field with small perturbations and expanding in terms of the higher order modes. So long as the mismatches are small, it is possible to consider only the first few terms of the expansion which have gained most of their power from the fundamental mode. Between various texts, the terms misalignment and

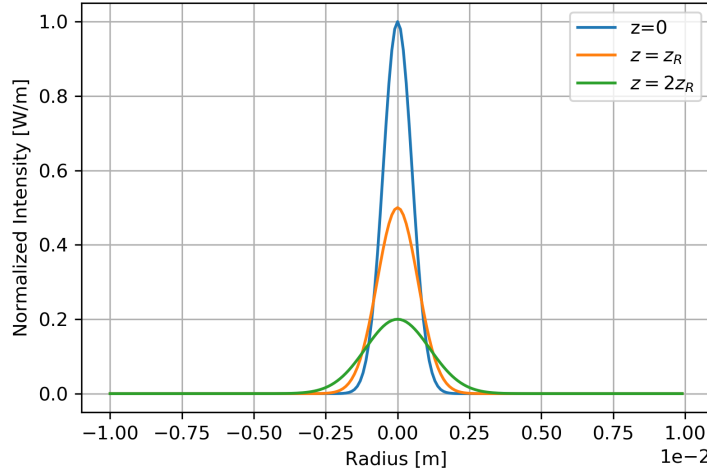


Figure 3.3: Intensity

mode mismatch are used interchangeably, which is not incorrect but creates some confusion. This thesis will try to distinguish the two effects because the actuators and sensors used for correction can be quite different.

Consider the first three Hermite-Gauss modes of equation 3.12 in one dimension and normalized to set the total optical power to unity:

$$\begin{aligned} U_0(r) &= \left( \frac{2}{\pi w^2(z)} \right)^{1/4} e^{-r^2/w^2(z)} \\ U_1(r) &= \left( \frac{2}{\pi w^2(z)} \right)^{1/4} \frac{2r}{w(z)} e^{-r^2/w^2(z)}, \\ U_2(r) &= \left( \frac{2}{\pi w^2(z)} \right)^{1/4} \frac{1}{\sqrt{2}} \left( \frac{4r^2}{w^2(z)} - 1 \right) e^{-r^2/w^2(z)} \end{aligned} \quad (3.17)$$

### Beam Axis Tilted

If the input beam entering an optical cavity is tilted by an angle  $\alpha$  with respect to the nominal cavity axis, the wave front of the input beam will have an extra phase propagation relative to the cavity that is approximately proportional to  $e^{ik\alpha r}$ . By implementing the small angle approximation, which is valid if the misalignment is much smaller than the divergence

angle of the fundamental mode  $k\alpha r \ll 1$ , the resultant input beam is

$$\Psi \approx U_0(r)e^{ik\alpha r} \approx U_0(r)(1 + ik\alpha r) = U_0(r) + \frac{ik\alpha w(z)}{\sqrt{2\pi}}U_1(r) \quad (3.18)$$

Here, the factor associated with the first higher order mode is complex, indicating there is a 90 degree phase difference between the fundamental and off-axis mode.

### Beam Axis Displaced

If the input beam is displaced in the transverse direction by a quantity  $\Delta r$ , the resultant waveform will be

$$\begin{aligned} \Psi &= U_0(r + \Delta r) \\ &= \left( \frac{2}{\pi w^2(z)} \right)^{1/4} e^{-(r+\Delta r)^2/w^2(z)} \\ &= \left( \frac{2}{\pi w^2(z)} \right)^{1/4} e^{-(r^2+2r\Delta r+\Delta r^2)/w^2(z)} \\ &\approx \left( \frac{2}{\pi w^2(z)} \right)^{1/4} e^{-r^2/w^2(z)} e^{-2r\Delta r/w^2(z)} \\ &\approx \left( \frac{2}{\pi w^2(z)} \right)^{1/4} e^{-r^2/w^2(z)} \left( 1 - \frac{2r\Delta r}{w^2(z)} \right) \\ &= \left( U_0(r) - \sqrt{\frac{2}{\pi}} \frac{\Delta r}{w(z)} U_1(r) \right) \end{aligned} \quad (3.19)$$

Similar to a tilted input beam axis, the displaced beam axis couples power to the first higher order mode, however, the latter does not have a 90 degree phase difference. This point is extremely important when trying to discern between the two effects. Although comparing the two cases in Figure 3.4b, one can already see the difference between wavefronts in the near field,  $z \ll z_R$ , and the far field,  $z \gg z_R$ . In the near field, there is no wavefront phase difference between the original beam and the displaced beam, but there is one for a tilted beam. Conversely in the far field, there is no phase difference due to a tilted beam, but there is one from a displaced beam. In order to implement a closed loop feedback system,

the wavefront sensors discussed in Section 3.2 will use this precise logic to extract an error signal.

### 3.1.2 Mode Mismatch and Higher Order Modes

Using the same formalism as above, determining the second order mode coupling from mode mismatch is repeated.

#### Waist Size Shifted

By considering the effect of evaluating the fundamental mode at the waist position,  $z = 0$ , but changing the waist size by a small amount  $\epsilon$ , it is possible to see coupling into higher order modes by expanding to first order.

$$\begin{aligned}
 \Psi &= U_0(r, w(z) = w_0/(1 + \epsilon)) \\
 &= \left( \frac{2}{\pi w_0^2} \right)^{1/4} \sqrt{1 + \epsilon} \quad e^{-r^2(1+\epsilon)^2/w_0^2} \\
 &\approx \left( \frac{2}{\pi w_0^2} \right)^{1/4} (1 + \epsilon/2) \quad e^{-r^2/w_0^2} \quad e^{-2r^2\epsilon/w_0^2} \\
 &\approx \left( \frac{2}{\pi w_0^2} \right)^{1/4} (1 + \epsilon/2) \quad e^{-r^2/w_0^2} \quad (1 - 2r^2\epsilon/w_0^2) \\
 &\approx \left( \frac{2}{\pi w_0^2} \right)^{1/4} \left( 1 + 2\epsilon \left( \frac{1}{4} - \frac{r^2}{w_0^2} \right) \right) \quad e^{-r^2/w_0^2} \\
 &= U_0(r) - \frac{\epsilon}{\sqrt{2}} U_2(r)
 \end{aligned} \tag{3.20}$$

By changing the waist size by a small amount, the mismatch will couple the fundamental mode to the in-phase second order Hermite Gauss mode.

#### Waist Position Shifted

To repeat the process from above with a waist position shift, it is useful to start with a more general equation that includes the phase that is gained from including the radius of

curvature,

$$\Psi = \left( \frac{2}{\pi w^2(z)} \right)^{1/4} e^{-r^2/w^2(z)} e^{-ikr^2/2R(z)} \quad (3.21)$$

where  $R(z)$  is from equation 3.9b. It is also useful to approximate the shift in waist position along the longitudinal axis is small compared to the Rayleigh range of the beam,  $\Delta z \ll z_0$ , which leaves the waist size approximately the same and the radius of curvature inversely proportional to the shift.

$$w^2(\Delta z) = w_0^2 \left[ 1 + \left( \frac{\Delta z}{z_0} \right)^2 \right] \approx w_0^2 \quad (3.22a)$$

$$R(\Delta z) = \Delta z \left( 1 + \left( \frac{z_0}{\Delta z} \right)^2 \right) \approx \frac{z_0^2}{\Delta z} \quad (3.22b)$$

Plugging the equations above into 3.21,

$$\begin{aligned} \Psi &\approx \left( \frac{2}{\pi w_0^2} \right)^{1/4} e^{-r^2/w_0^2} e^{-ikr^2\Delta z/2z_0^2} \\ &\approx \left( \frac{2}{\pi w_0^2} \right)^{1/4} e^{-r^2/w_0^2} \left( 1 - \frac{ikr^2\Delta z}{2z_0^2} \right) \\ &= U_0(r) - \left( \frac{2}{\pi w_0^2} \right)^{1/4} e^{-r^2/w_0^2} \frac{ikr^2\Delta z}{2z_0^2} \\ &= U_0(r) - i \frac{\Delta z}{2kw_0^2} \left( 4U_2(r) + U_0(r) \right) \end{aligned} \quad (3.23)$$

The equations above show that a fundamental Gaussian mode that is shifted in waist position will couple power to the second order Hermite Gauss mode. Although changes in the waist size or position couple power to the same mode, they differ by a 90 degrees in phase as denoted by the extra factor of  $i$  in the coupling coefficient. By recognizing the two effects are in different quadrature phases will allow a user to design a system to distinguish between the different types of physical couplings, this is shown in Section 3.2.

In order to be physically valid one would need to consider the full two dimensional space so that the equation would encapsulate the full transverse mode, however, the x and y components would follow the exact same derivation. On that point, it is important to note

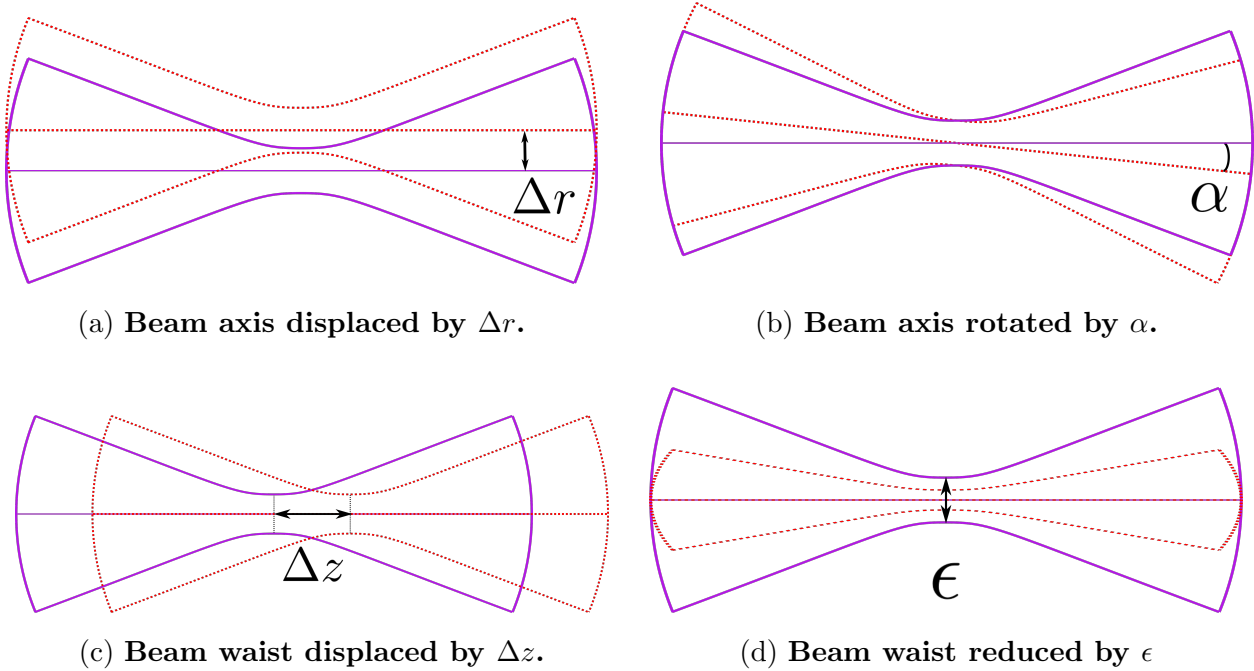


**Figure 3.4: Misalignment and mode mismatch between two different Gaussian beams.** The purple solid curves represent the original Gaussian shape and the red dotted curves are beams which have been augmented in one degree of freedom. It is important to note that using this representation uses the eigenmode of the cavity as a starting basis, if one were to create these misalignments using the actual optics, there needs to be a linear combination of rotations or curvature changes.

that only the mode mismatch couplings from either a varying waist position or size has higher order modes that are circularly symmetric.

## 3.2 Wavefront Sensing

In Chapter 2.0.1 and 2.0.5, a heterodyne detection scheme was used to sense the longitudinal degree of freedom for optical cavities. Analogously, a technique using sidebands can employ a modal decomposition of the full electric field which allows the use of wavefront sensors to extract an error signal. Hefetz et.al [51] created a formalism to describe the use of wavefront sensors by creating frequency sidebands which accumulate a different Gouy phase than the electric field at the carrier frequency when passed through the optical system. By

observing the demodulated signal of the intensity, it is possible to obtain a linear signal that corresponds to a physical misalignment or mode mismatch. Fundamentally, the purpose of wavefront sensing is to detect the content of higher order modes due to physical disturbances of the optical cavity and by extension, it is examining the difference between the incoming beam and the cavity eigenmodes.

Consider a general equation for an electric field which is a linear combination of all higher order modes of the complex amplitude

$$E(x, y, z) = \sum_{m,n}^{\infty} a_{mn} U_{mn}(x, y, z) \quad (3.24)$$

where  $U_{mn}(x, y, z)$  are the eigenmodes described in equation 3.12 (or 3.14) and  $a_{mn}$  is the complex amplitude. It is also convenient in the following analysis to use vectors when describing the composition of the electric fields.

$$|E(x, y, z)\rangle = \begin{pmatrix} E_{00} \\ E_{01} \\ E_{10} \\ E_{20} \\ E_{02} \end{pmatrix} \quad (3.25)$$

When creating a theory that involves laser beams, it is useful to define operators that are important in describing physical situations. For example, laser beams propagate through space and pick up phase according to equation 3.12 which can be represented by the spatial propagation operator,

$$\hat{P}_{mn,kl} = \delta_{mn}\delta_{kl} \exp[-ik(z_2 - z_1)]\exp[i(m + n + 1)\zeta(z)] \quad (3.26)$$

However, it is useful to compare how the fundamental Gaussian mode propagates compared

to the higher order modes,

$$\hat{\eta}_{\mu\nu} = \begin{pmatrix} e^{i\zeta} & 0 & 0 & 0 & 0 \\ 0 & e^{2i\zeta} & 0 & 0 & 0 \\ 0 & 0 & e^{2i\zeta} & 0 & 0 \\ 0 & 0 & 0 & e^{3i\zeta} & 0 \\ 0 & 0 & 0 & 0 & e^{3i\zeta} \end{pmatrix} \quad (3.27)$$

From the above diagonal elements, it is clear that the higher order modes have an extra phase compared to the fundamental 00 mode, this effect will be extremely important on how an error signal can be derived from the optical system.

$$|E(x, y, z_2)\rangle = \hat{M}(x, y, z_1, z_2) |E(x, y, z_1)\rangle \quad (3.28)$$

where  $\hat{M}(x, y, z_1, z_2)$  is the misalignment operator. Since we are using the paraxial approximation, the z-components of the misalignment operator are small so we can approximate  $\hat{M}(x, y, z_1, z_2) \approx \hat{M}(x, y)$  and the expectation value is

$$M_{mn,kl} = \langle U_{mn}(x, y, z_1) | M(x, y) | U_{kl}(x, y, z_2) \rangle \quad (3.29)$$

where the product is an integral over the transverse space  $\iint_{D(x,y)} dx dy$

$$\hat{\Theta}_{\mu\nu} = \begin{pmatrix} 1 & 2i\theta_x & 2i\theta_y & 0 & 0 \\ 2i\theta_x & 1 & 0 & 0 & 0 \\ 2i\theta_y & 0 & 1 & 0 & 0 \\ 0 & 0 & 0 & 1 & 0 \\ 0 & 0 & 0 & 0 & 1 \end{pmatrix} \quad (3.30)$$

$$\hat{\mathbb{D}}_{\mu\nu} = \begin{pmatrix} 1 & \alpha_x/\omega_0 & \alpha_y/\omega_0 & 0 & 0 \\ \alpha_x/\omega_0 & 1 & 0 & 0 & 0 \\ \alpha_y/\omega_0 & 0 & 1 & 0 & 0 \\ 0 & 0 & 0 & 1 & 0 \\ 0 & 0 & 0 & 0 & 1 \end{pmatrix} \quad (3.31)$$

$$\hat{\mathbb{Z}}_{\mu\nu} = \begin{pmatrix} 1 & 0 & 0 & \Delta z_x & \Delta z_y \\ 0 & 1 & 0 & 0 & 0 \\ 0 & 0 & 1 & 0 & 0 \\ \Delta z_x & 0 & 0 & 1 & 0 \\ \Delta z_y & 0 & 0 & 0 & 1 \end{pmatrix} \quad (3.32)$$

where  $\Delta z_{(x,y)} = \frac{i}{\sqrt{2}} \frac{\lambda b}{2\pi\omega_0}$

$$\hat{\mathbb{Z}}_{0,\mu\nu} = \begin{pmatrix} 1 & 0 & 0 & \Delta z_{0,x} & \Delta z_{0,y} \\ 0 & 1 & 0 & 0 & 0 \\ 0 & 0 & 1 & 0 & 0 \\ \Delta z_{0,x} & 0 & 0 & 1 & 0 \\ \Delta z_{0,y} & 0 & 0 & 0 & 1 \end{pmatrix} \quad (3.33)$$

where  $\Delta z_{0,(x,y)} = \frac{1}{\sqrt{2}} \frac{\omega' - \omega_0}{\omega_0}$

## Gouy Phase

Understanding the relationship between Gouy phase as defined by 3.9c and how the term is used colloquially within the LIGO experimental community is not very straightforward. Gouy phase given by equation 3.9c is the phase lag between a Gaussian beam and a perfect plane wave that occurs as a function of propagation along the  $\hat{z}$ -axis which ranges from  $\zeta(z) = \pm\pi/2$  for  $z = \pm\infty$ . Physically, this could be interpreted as the difference between the laser beam behaving like a plane wave when  $z \approx 0$  (or near field) and eventually evolving

into a spherical wave when  $z \approx \pm \infty$  (or far field), see Figure 3.2. Although this phenomenon is interesting mathematically, most texts do not consider how to practically use or measure the Gouy phase. In LIGO technical notes and electronic logs, the Gouy phase of sensors or actuators is often used to describe where along the beam path the piece of equipment is located. This will indicate what degree of freedom is being observed or adjusted. For example, in ray optics [74] a laser beam has two degrees of freedom, the displacement and angle from the optical axis. If an actuator such as a piezo-electric transducer with an attached reflective mirror is placed near the origin or focus of the laser beam, then the controlled degree of freedom is only the angle. Alternatively, if the actuator is placed in the far field then the controlled degree of freedom is almost entirely displacement. So to have full control over the alignment of a laser beam, it is required to have two actuators separated by 90 degrees in Gouy phase.

This is also true of sensors at various points along the  $\hat{z}$ -axis to determine the exact alignment of the optical beam. In practice, it is impossible to sense the true waist of an optical system because it could be inside a Fabry-Perot cavity. So the clever designer must insert a pick-off beam to sample the transmission or reflection of the interested optical system and use a combination of lenses to create a telescope for the sensors and infers the degrees of freedom. Then, by rotating to the two-dimensional space created by the sensors to represent the interested space spanned by the optical system's degrees of freedom; colloquially, this is known as a sensing matrix. Using this method, sensors do not have to be exactly at the near or far field because it is only required that the two sensors are separated by  $\pi/2$  in Gouy phase, in fact, it is usually easier to place one sensor at  $+\pi/4$  and the other at  $-\pi/4$ . Unfortunately, there is no transducer that directly measures the Gouy phase so in order to *determine* the Gouy phase of a particular sensor or actuator, one must model the beam propagation and fit the waist location.

Another way which Gouy phase is presented in many LIGO discussions is regarding the round trip accumulation of phase while propagating in an optical cavity. This plays an

important role because the round trip Gouy phase is directly proportional to the transverse mode spacing. Recall that the free spectral range of a cavity is equal to  $f_{\text{FSR}} = c/2L$  which sets the frequency separation between the fundamental modes, and that the Gouy phase propagation for higher order modes is equal to  $(m+n+1)\zeta(z)$  so these modes will effectively *see* a different cavity than the zeroth. Gouy phase can be calculated explicitly by using the ABCD formulation and relating the matrix elements to the round trip phase,

$$\zeta = \text{sgn}B \arccos \left( \frac{A+D}{2} \right) \quad (3.34)$$

where A, B, C, and D are the matrix elements of the optical system. The Gouy phase is related to the transverse mode spacing by

$$f_{\text{TMS}} = \frac{\zeta}{2\pi} f_{\text{FSR}} \quad (3.35)$$

The extra Gouy phase that a higher order mode accrues as a function of  $z$  shows up as in the frequency or cavity length domain as one sweeps through a full free spectral range using an offset in the length or frequency error signal. This can be directly used to measure the higher order mode separation and becomes important if the cavity has a low finesse which means the fundamental Gaussian mode has a spread comparable in frequency to the first order mode then it is easy to hop from one to the other (see Figure 3.5).

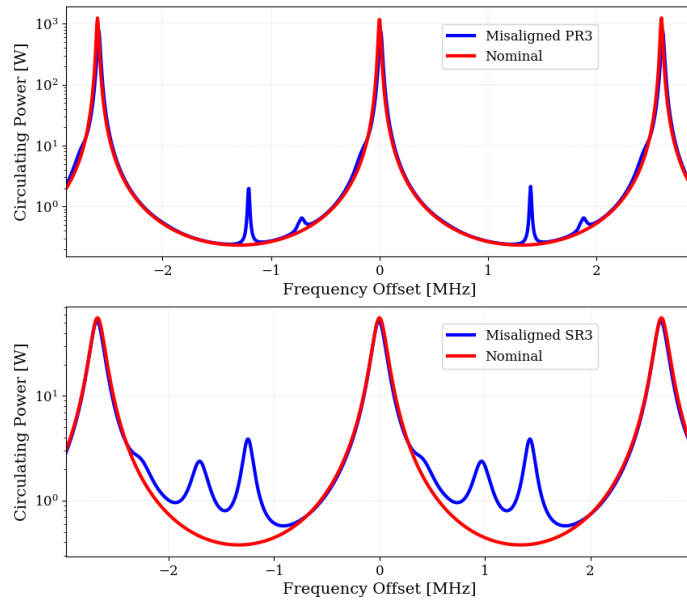


**Figure 3.5: A Finesse model of a longitudinal mode scan comparing the Advanced LIGO power recycling and signal recycling cavities** The upper and lower plots represents the PRC and SRC, respectively. The main difference between these two optical cavities is obvious when comparing the three large peaks corresponding to the 00 mode resonances. The power recycling cavity has a much higher and sharper peak which indicates a larger finesse where as the signal recycling cavity is a much lower finesse has a broader and shorter peak. The red traces are with nominal alignment compared with the blue lines corresponding to misalignments of PR3 and SR3 by  $1\mu\text{rad}$ . This allows higher order mode content to resonate as a function of length or frequency.

# Chapter 4

## Simulating Mode-Matching with FINESSE

In Chapter 2, the optical gain from differential arm motion was determined analytically with very few approximations but in actuality, LIGO has more degrees of freedom which make precise calculations very cumbersome. As with most simple concepts, the complexity scales very rapidly in application to the main interferometer and mode matching is no exception so it is useful to use a full scale numerical simulation to extract as much information as possible. FINESSE [69] [11] is one of the leading full-scale interferometer simulation tools which use the linear input-output relations of electromagnetic fields to model complex properties of the LIGO interferometer. The goal of this chapter is to apply FINESSE in order to model the quantum limited noise sensitivity with mode-mismatch at various positions in the interferometer and determine which actuation points are needed for optimal matching into the output mode cleaner. This is extremely important in the current generation of Advanced LIGO when squeezing is implemented because of the sensitivity to losses in between the optical parametric oscillator and the interferometer cavities. By using FINESSE's ability to incorporate higher order beams and RF sidebands, it is possible to quickly and accurately model mode matching.

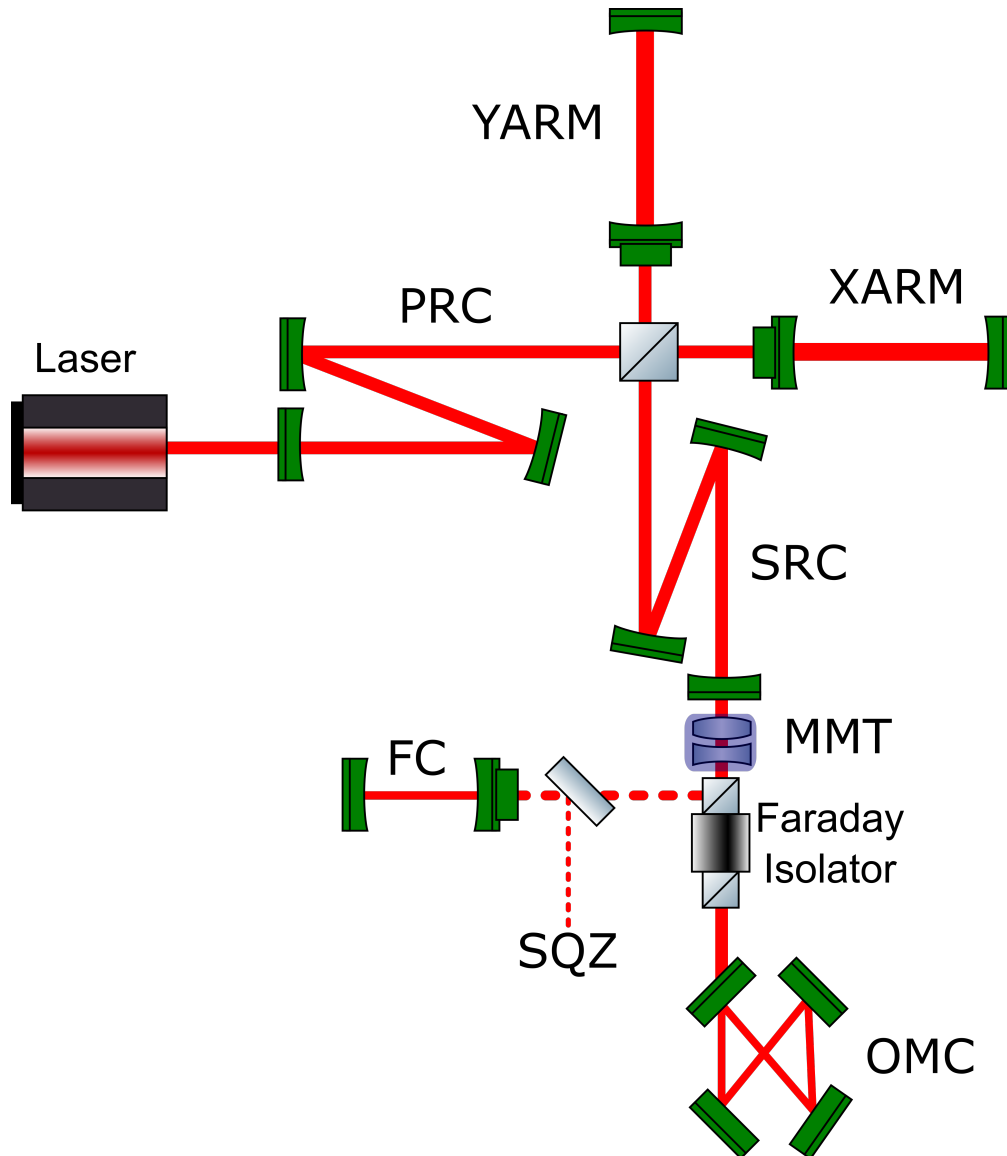


Figure 4.1: **Full interferometer simulation with FINESSE.** This includes squeezed light, a filter cavity, and an ideal mode matching telescope (highlighted in blue) at the signal recycling output port which can be turned on/off in order to understand the SRC mode mismatches without the lensing effects introduced when changing the SRM radius of curvature. For brevity, the input mode cleaner is omitted in the schematic but is also a resonant cavity in the simulation. Optical parameters are taken from the as-designed values for advanced LIGO and a few key variables are replaced with H1 specific constants.

## 4.1 FINESSE Simulations

The power of numerical simulations has an interesting dual advantage, firstly, optical parameters which are historically difficult to measure such as Gouy phase can be directly calculated and modeled to guide in designing systems. Secondly, in places where analytical calculations become unwieldy, numerical methods can accurately describe complex parameter spaces.

$$\begin{bmatrix} 0 & r_b e^{i\phi} & it_b & 0 \\ r_b e^{i\phi} & 0 & 0 & it_b \\ it_b & 0 & 0 & r_b e^{-i\phi} \\ 0 & it_b & r_b e^{-i\phi} & 0 \end{bmatrix} \begin{bmatrix} \text{In1} \\ \text{In2} \\ \text{In3} \\ \text{In4} \end{bmatrix} = \begin{bmatrix} \text{Out1} \\ \text{Out2} \\ \text{Out3} \\ \text{Out4} \end{bmatrix}$$

Figure 4.2: **How FINESSE sees a beamsplitter.** An example of the coupling matrix for an arbitrary beamsplitter with reflectivity,  $r_b$ , and transmissivity,  $t_b$ . Another free parameter for a beamsplitter is the phase shift  $\phi = 2\phi_u \frac{\omega}{\omega_0} \cos(\alpha)$ , where  $\phi_u$  is a user defined phase that can be varied for a simulation (such as dithering),  $\omega/\omega_0$  is the ratio of the reflected to incident angular wave frequency and  $\alpha$  is the angle between the beamsplitter front surface and the incident field vector In1. As it turns out, most of the resonators in the following simulations use beamsplitters to represent the cavity mirrors.

An Advanced LIGO configuration file [12] which utilizes the as-designed values for the lengths and optical parameters serves as a good starting point for simulating the entire interferometer. To incorporate more realistic numbers, in-situ measurements were taken at Hanford with a beam profile at HAM6 to understand the Gaussian beam shape entering the output mode cleaner. By defining the optical parameters and distances, FINESSE creates coupling matrices for individual components which are generally comprised of mirrors, spaces, or beamsplitters. Some specialized components are also useful such as modulators to create sideband fields, Faraday isolators, and detectors (both amplitude and power). For each component, there are corresponding nodes that link the entire optical system together. The coupling matrices are compiled into an interferometer matrix and the solutions are solved

numerically,

$$\hat{M}_{ij}^{\text{IFO}} |x_{\text{sol}}\rangle = |x_{\text{input}}\rangle \quad (4.1)$$

where  $|x_{\text{sol}}\rangle$  and  $|x_{\text{input}}\rangle$  are the solution and input vectors, respectively. Generally, the right hand side is made up of laser inputs, modulator sidebands, noise, and signal sidebands. This form has incredible efficiency and can represent the entire interferometer in a single matrix with direct access to all field amplitudes. In addition, changing optical parameters during a simulation is made easier by varying the coupling coefficients after the matrix has been calculated so the algorithm does not have to re-compute every term.

## 4.2 Effects of Signal Recycling Mismatch

Beam tracing in FINESSE starts by determining the q-parameters for each user defined cavity. If there are multiple cavities, it will calculate in the order written and the last cavity in the parameter file sets the basis of populating the rest of the interferometer. Table 4.3 shows the extracted cavity values for reference. The algorithm continues by automatically propagating the laser beam through each node via ABCD transformation methods. For a perfectly mode-matched interferometer, the q's at each node are the same no matter which cavity basis is chosen but this is not true when introducing thermal lensing or errors for individual resonators. At this point, it becomes extremely important to properly track the q-parameters because they are used to calculate the overall mismatch between cavities. To simplify the use of multiple coupled resonators, it is useful to turn all but one of the cavity commands off so that only one basis q-parameter is explicitly used and there is no ambiguity.

FINESSE has the ability to extract two parameters which calculate the sensitivity: noise and signal. By default, vacuum fluctuations are present at each unused port and associated optical losses. This methodology can be verified analytically using the full quantum mechanical description in Section 2.0.6 and the semi-classical Schottky shot noise estimation. For radiation pressure effects, the mechanical transfer function is defined by a simplified

pendulum with  $H(f) \propto \frac{1}{M f^2}$  dependence above the resonance frequency which is chosen to be approximately 0.1 Hz for these simulations. As previously shown in Section 2.0.6, the radiation pressure effects are proportional to the input laser power and converts amplitude fluctuations into phase noise. Naturally, this is a nonlinear equation when dealing with field amplitudes so FINESSE makes certain approximations which reduces the complexity,

1. Induced motion from radiation pressure is very small compared to the light wavelength so the equations of motion can be linearized.
2. Signal sideband frequencies are very small compared to the optical sidebands created by the modulator such that the carrier creates a much larger radiation pressure effect.
3. The amplitude of signal sidebands are much smaller compared to the carrier.

In terms of gravitational wave detectors, these approximations are reasonable because the machines tend to operate with closed-loop control systems and in steady-state equilibrium. Also, the signal sidebands never reach above 8 kilohertz for two reasons: astrophysical sources from compact binaries coalesce at around 1.5 kHz and the Nyquist frequency for the differential arm channel is sampled at 16 kHz so the Nyquist frequency is much smaller compared to the 9 MHz sideband from the electro-optical modulator.

To generate the signal, differential arm motion is created by varying the two arm cavity lengths 180 degrees out of phase and measuring the optical gain transfer function at the output mode cleaner transmission port. The results can be compared directly to the analytical transfer function described by equation 2.43 to verify the right DC amplitude and pole frequency. Figure 4.1 shows the results of mode mismatch affecting the quantum limited noise sensitivity.

With regards to the squeezer implementation, the model applies both squeezed light and a filter cavity before entering the interferometer to compare the effect of mode-matching losses on the quantum limited sensitivity. In FINESSE, the squeezer node employs classical sideband implementation while in reality, modified vacuum is generated using the optical

parametric oscillator (OPO) which is a bow-tie cavity with a nonlinear optic that is not yet handled by the available FINESSE components and the nonlinear crystal actually keeps the cavity from being geometrically unstable. So for now, it is enough to use quantum noise sidebands with defined phase and amplitude variances have two open parameters, the squeezing gain and phase angle.

LIGO's coupled optical cavities allow for a large parameter space when trying to match multiple resonators. Changing the curvature of an optic in the signal recycling cavity will obviously change its overlap with the output mode cleaner but the effect will also vary the arm mode propagation to the OMC as well. This will have a confusing result because it is impossible to discern whether the degradation in performance is due to the arm or SRC mismatch. One of the ways to get around this is to implement a perfect mode-matching telescope between the SRC and OMC to keep the arm modes consistent with the output mode cleaner so that the only effect on the interferometer is a non-optimal signal recycling cavity. The deterioration in sensitivity when mismatching the SRC has a two-fold effect, the introduction of vacuum fluctuations will degrade the squeezed field in a nonlinear fashion hence increasing the noise (even with perfect squeezing phase). On top of that, extra SRC losses will affect the total optical signal gain at the antisymmetric port, which means sacrificing some losses in the SRC to mode match the squeezer field will not actually improve the sensitivity. Comparatively, the extra losses introduced at the antisymmetric port before entering the output mode cleaner will only see increased losses that couple quantum vacuum. The comparison is shown in Figure 4.3.

	PRC w	PRC S	SRC w	SRC S	ARMs w	ARMs S	OMCs w	OMCs S
PRM	4.537	0.006	0.000	0.000	0.000	0.000	0.000	0.000
PR2	-45.004	-0.058	0.000	0.000	0.000	0.000	0.000	0.000
PR3	-3321.891	-4.315	0.000	0.000	0.000	0.000	0.000	0.000
SRM	0.000	0.000	-5.097	-0.006	0.000	0.000	0.875	1.114
SR2	0.000	0.000	-128.889	-0.160	0.000	0.000	-2.792	-99.513
SR3	0.000	0.000	-5460.964	-6.774	0.000	0.000	-19.564	-4294.447
ITMTL	-3188.263	4142.666	-5254.308	4140.289	0.000	0.000	0.000	0.000
ITM	-2310.433	3002.047	-3807.633	3000.325	-1827.435	3002.782	0.000	0.000
ETM	0.000	0.000	0.000	0.000	3774.807	4.682	0.000	0.000
OM1	0.000	0.000	0.000	0.000	0.000	0.000	0.164	0.552
OM2	0.000	0.000	0.000	0.000	0.000	0.000	0.511	-0.889
OM3	0.000	0.000	0.000	0.000	0.000	0.000	-0.222	-0.453

Table 4.1: **Mode matching actuation matrix for the transverse x direction.** Each of the row elements represent actuators and columns show the affected cavity defocus  $S$  or beam size  $w$  per diopter change, which are scaled by the initial perfect mode matching values. For small mismatches, the slope is assumed to be linear.

	PRC w	PRC S	SRC w	SRC S	ARMs w	ARMs S	OMCs w	OMCs S
PRM	5.092	0.006	0.000	0.000	0.000	0.000	0.000	0.000
PR2	-52.019	-0.062	0.000	0.000	0.000	0.000	0.000	0.000
PR3	-3852.041	-4.569	0.000	0.000	0.000	0.000	0.000	0.000
SRM	0.000	0.000	-6.870	-0.007	0.000	0.000	0.870	1.105
SR2	0.000	0.000	-178.704	-0.169	0.000	0.000	-2.783	-99.469
SR3	0.000	0.000	-7589.021	-7.189	0.000	0.000	-19.509	-4292.095
ITMTL	-3700.089	4142.316	-7309.182	4139.780	0.000	0.000	0.000	0.000
ITM	-2681.338	3001.794	-5296.743	2999.956	-1827.470	3002.700	0.000	0.000
ETM	0.000	0.000	0.000	0.000	3774.854	4.697	0.000	0.000
OM1	0.000	0.000	0.000	0.000	0.000	0.000	0.172	0.557
OM2	0.000	0.000	0.000	0.000	0.000	0.000	0.508	-0.887
OM3	0.000	0.000	0.000	0.000	0.000	0.000	-0.165	-0.344

Table 4.2: Mode matching actuation matrix for the transverse y direction.

Parameters	IMC	XARM	YARM	PRX	PRY	SRX	SRY	OMC
Rayleigh Range [m]	13.338	427.807	427.807	5.314	5.314	2.132	2.132	0.708
Waist to 1st Mirror [m]	-16.473	-1834.220	-1834.220	6.940	6.940	4.733	4.733	0.141
Cavity Length [m]	16.473	3994.500	3994.500	57.711	57.632	56.065	55.985	0.566
FSR [MHz]	9.099	0.038	0.038	2.597	2.601	2.674	2.677	264.975
RT Gouy Phase [deg]	102.008	-48.661	-48.661	51.724	51.722	38.311	38.309	78.979
Pole Frequency [kHz]	8.636	0.045	0.043	309.692	309.939	409.982	410.283	321.971
Finesse	526.837	413.523	436.867	4.193	4.196	3.261	3.263	411.488
A	1.000	-2.559	-2.559	-0.406	-0.406	-0.591	-0.591	-0.004
B	32.946	-6225.726	-6225.726	11.286	11.286	7.835	7.835	0.722
C	-0.073	0.002	0.002	-0.148	-0.148	-0.291	-0.291	-1.387
D	-1.416	3.880	3.880	1.645	1.645	2.161	2.161	0.386

Table 4.3: **Calculated cavity parameters for the advanced LIGO interferometer.** The values were obtained using FINESSE’s *cav* commands which are an integral part of the beam tracing algorithm. Here, the power (and signal) recycling cavity is split into two linear resonators made up of the PRM and HR surface of the respective ITMs. In an ideal world, the reflectivity of ITMX and ITMY are the same but can actually vary up to 5% in the case of H1 [27]. This mostly affects the arm cavity Finesse but can have small effects on the power recycling cavity as well.

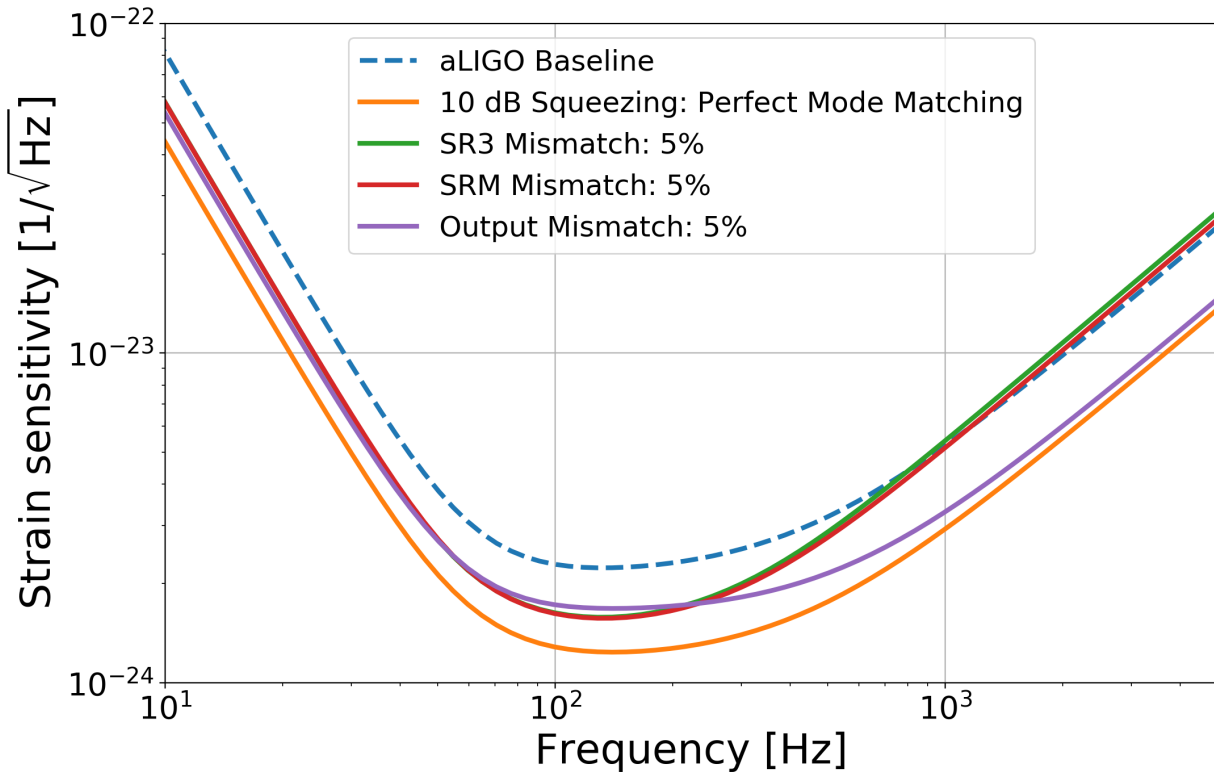
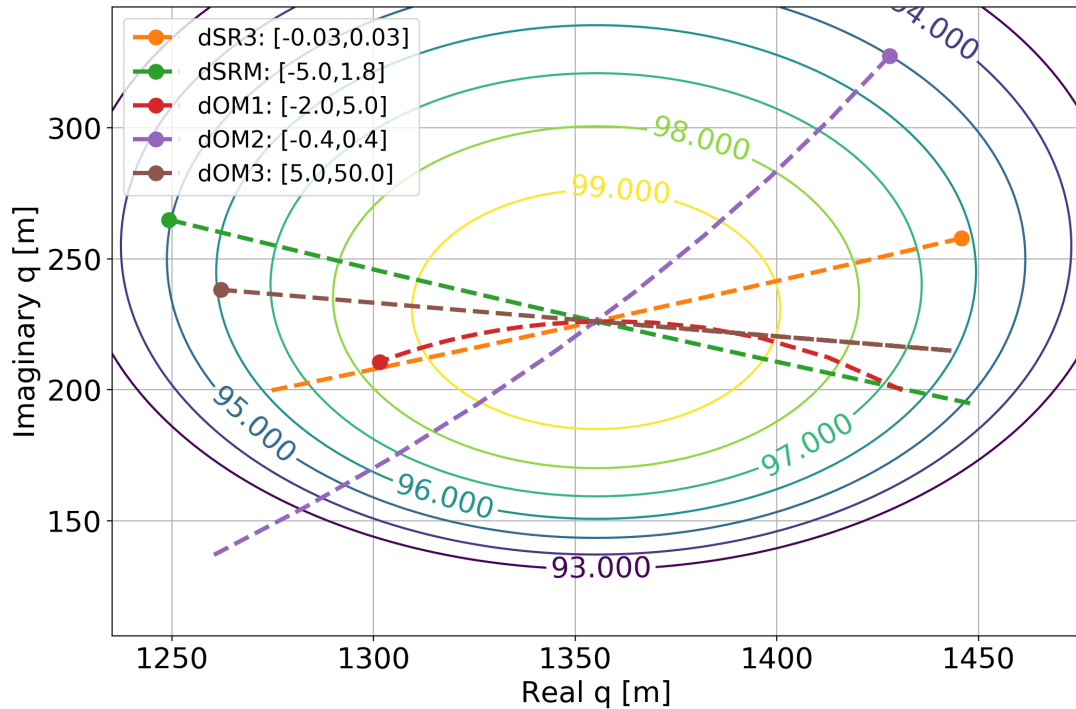


Figure 4.3: Quantum limited sensitivity simulation to compare mismatches in the presence of squeezed light. With 10 db of broadband squeezing, the simulation introduced mismatch at various actuators to change the mode shape at the output port. Although there is still 5% mismatch in each case, the introduction of quantum noise and the degradation of squeezing is much worse when introducing losses in the signal recycling cavity as opposed to the output train. In addition, mismatching the signal recycling cavity will change the relative phase angle between the interferometer and squeezed light which has to be re-optimized.



**Figure 4.4: Simulating the output actuator phase spaces projected onto the OMC mode basis.** By allowing FINESSE to do the ray tracing algorithm for the entire interferometer, it is relatively straightforward to change the radii of curvature for different optics and project the effect onto the OMC in order to understand the orthogonality when choosing mirrors for mode matching. Interestingly, the most orthogonal actuators for small mismatches happen to be SRM and OM2, however, OM1 becomes quadratic much more quickly which leads to increased range. The ending dots indicate the positive direction for changing radii of curvature as seen by the various optics. Also, the change in radii of curvature in units of meters is shown on the legend.

# Chapter 5

## Experimental Mode Matching

### Cavities at Syracuse

In conjunction with Sandoval et al [62], the table-top adaptive mode matching experiment was able to show the feasibility of a fully dynamical system at Syracuse University. Most of the work done by the author was focused on converting and upgrading the real-time digital system (RTCDS) from being used by the optical trap experiment [71] to adaptive mode matching and interfacing the RF sensors into the digital system. There is also a section on the usage of cylindrical lenses and quadrant photodiodes as a viable method of extracting a mode matching error signal.

#### 5.1 Commissioning the Real Time Digital System

Dynamic control systems require both actuators and sensors which are interfaced in a real-time manner and this requires the use of analog-to-digital (ADC) and digital-to-analog (DAC) converters. A LIGO standard system uses a front end computer that reads in data and processes the signals based off a Simulink graphical model that allows for simple logic, mathematical operations, and frequency dependent filtering. The real time data acquisition code is user-interfaced with a Motif Editor and Display Manager (MEDM) that is able to

report and execute variables such as gains and matrix elements.

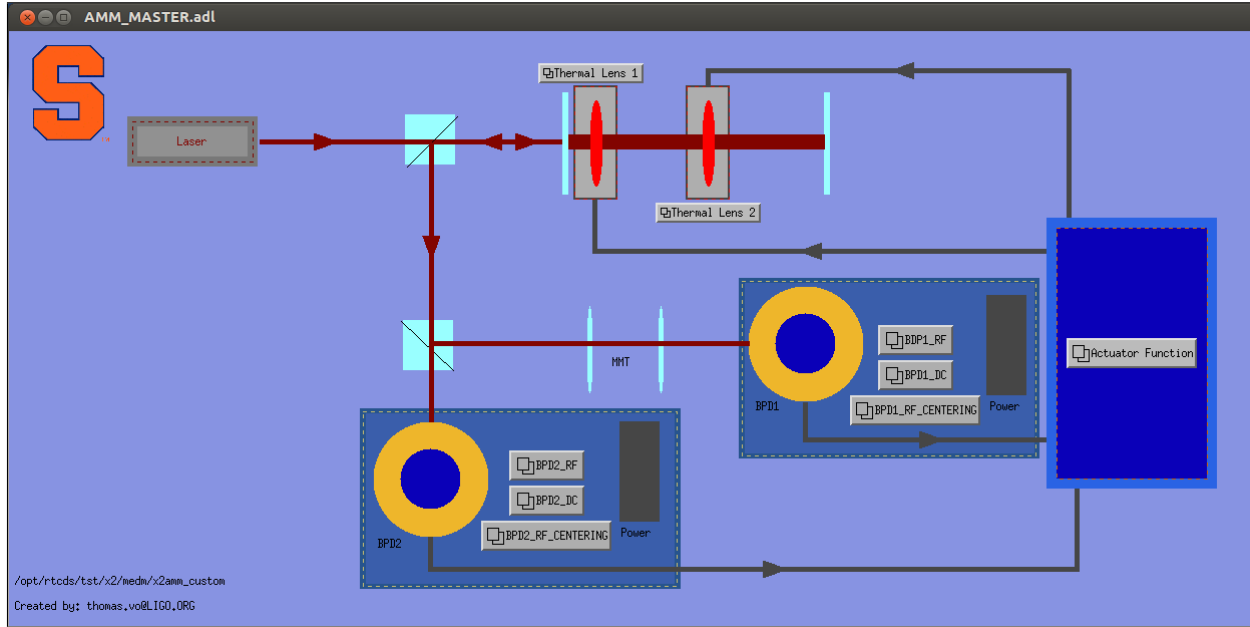


Figure 5.1: **MEDM master screen for adaptive mode matching at Syracuse.** Here, the demodulated error signal in reflection of the Fabry-Perot cavity is divided by a beam-splitter and fed into two RF detectors, one of which is depicted to have a mode matching telescope MMT to project a different Gouy phase to sense an orthogonal degree of freedom. Then the signal is sent to an actuator function which allows for diagonalizing the signals and can be sent to a set of thermal lens at different Gouy phases for actuation. The adaptive lenses are actually placed in the beam path before entering the cavity but for demonstrative purposes, they are portrayed at two different Gouy phases of the resonator.

## 5.2 Sensors

Recall in Section 3.2 that the RF modal decomposition technique relies on comparing the Gouy phase of higher order modes to the fundamental Gaussian mode with an array of RF photodiodes in order to extract an error signal. The complication arises when using this method to extract the beat note between the fundamental mode and symmetric donut mode because the photodetector arrays must match the higher order mode geometry. This is easier to deal with when trying to sense angular distortions from a misaligned cavity because

the 01 and 10 modes can be sensed with a split photodetector, however, using a quadrant photodiode will not work to sense mode mismatch due to the cylindrical symmetry of the 02 and 20 modes. Currently, Advanced LIGO uses no RF sensors to detect mode matching so the next sections will provide sensing methods which can be used for dynamic closed loop feedback control.

### 5.2.1 Bullseye Photodiodes (BPD)

It is clear that using a quadrant photodetector to measure the symmetric  $U_{20} + U_{02}$  mode which arises from mismatch is futile because the integrated power on each side will be exactly the same due to donut mode symmetry. So it is simplest to try subtracting the inner beam power from the outer ring of the electric field in order to measure a phase difference using a specialized RF photodiode called a Bullseye Photodetector shown in Figure []. This method is proven to already work in the Enhanced LIGO era [67] and is the most natural extension of the angular wavefront sensing/controls that is implemented in Advanced LIGO.

#### BPD Calibration

To use the BPDs, there are a few steps required in designing the optical setup which is different than the standard PDH or WFS method. Most notably, the beam size incident on the BPD must be tuned such that the zero crossing of the  $(U_{20} + U_{02})$  matches the boundary between the inner and outer segments. This condition is met if  $\omega_0 = \sqrt{2}r_0$  and Appendix C shows the power ratio of the outer to inner segments when this is true,

$$\text{Power Ratio} = \frac{P_2 + P_3 + P_4}{P_1} = \frac{e^{-2r_0^2/\omega_0^2}}{1 - e^{-2r_0^2/\omega_0^2}} \approx 0.582 \quad (5.1)$$

Picture of BPD

Pitch and Yaw sensing matrix

Another constraint on using this method is that the Gouy phase separation between

successive BPDs must be close to 45 or 135 degrees so that the error signals from each BPD can be orthogonalized, this is in contrast to angular wavefront sensors which require 90 degree Gouy phase separation.

### 5.2.2 Mode Converters

The bullseye photodiodes can be difficult to calibrate and manufacture so a particularly interesting method of sensing mode mismatch is to convert the axisymmetric fields with a cylindrical telescope such that an error signal can be extracted with quadrant photodiode. Using lenses which have two radii of curvature for each direction ( $x$  or  $y$ ) with one being flat and the orthogonal is curved with some focal length,  $f$ . The idea is to break the cylindrical symmetry of the donut mode (Figure 5.5) and convert the beam into a pringle mode by advancing the phase of one axis by a factor of  $\pi/2$  to create a relative sign flip. Then, an error signal can be extracted using the radio frequency quadrant photodiode that the angular wavefront sensors employ

#### Vector formalism for laser beams and optical cavities

Consider an optical cavity that is longitudinally resonant on the  $\text{TEM}_{00}$  mode using the Pound-Drever-Hall technique shown in Section 2.0.2 and also locked with angular wavefront sensors shown in Section 3.2. When there is a small mismatch between the waist size and position of the input beam relative to the cavity, this is equivalent to coupling the  $\text{TEM}_{00}$  mode into higher order modes. Since mode matching is only concerned with coupling to the second order modes, the resultant field in reflection ( $r_{FP}$ ) of a Fabry-Perot resonator will have the form

$$|U_{refl}\rangle = r_{FP} \begin{pmatrix} U_{00} \\ 0 \\ 0 \end{pmatrix} + \epsilon \begin{pmatrix} 0 \\ U_{20} \\ U_{02} \end{pmatrix} \quad (5.2)$$

$$\epsilon = \frac{1}{\sqrt{2}} \left( \frac{\delta w}{w_0} + i \frac{\delta z}{z_R} \right) \quad (5.3)$$

where  $\delta w$  and  $\delta z$  are the mismatches in waist size and position, respectively. O’Neil et al [70] wrote down a formalism that explicitly showed the effects of cylindrical telescopes on the full range of Hermite Gauss modes. An arbitrary mode conversion system,  $\hat{M}$ , is comprised of two cylindrical lenses and can be described by two distinct operators,

$$\hat{M} = \hat{R}\hat{C} \quad (5.4)$$

where  $\hat{R}$  is a rotation operator that depends on a angle  $\theta$  which can rotate about the axis of propagation and  $\hat{C}$  is the mode converting operator which depends on the amount of phase advance seen by higher order modes. Physically,  $\hat{R}$  can be shifted by rotating the entire cylindrical telescope about the axis of propagation whereas the phase advance can be changed by choosing various focal lengths. Since mode matching primarily couples power into the 02 and 20 modes of the cavity, we can use a 3x3 matrix. For rotations about the axis of propagation, the operator is

$$\hat{R}_{ij} = \begin{pmatrix} 1 & 0 & 0 \\ 0 & \cos(\Delta\theta) & \sin(\Delta\theta) \\ 0 & -\sin(\Delta\theta) & \cos(\Delta\theta) \end{pmatrix} \quad (5.5)$$

For the mode converter phase advance, the operator is

$$\hat{C}_{ij} = \begin{pmatrix} 1 & 0 & 0 \\ 0 & e^{-i\Omega_{20}} & 0 \\ 0 & 0 & e^{i\Omega_{02}} \end{pmatrix} \quad (5.6)$$

where  $\Omega_{mn} = (m + \frac{1}{2}) \tan^{-1} \left( \frac{d}{z_{R,x}} \right) + (n + \frac{1}{2}) \tan^{-1} \left( \frac{d}{z_{R,y}} \right)$  and  $d$  is the distance from one cylindrical lens to the waist.  $\Omega_{mn}$  is the amount of phase advance that a higher order mode

will experience due to the mode converter. It is important to note, the matrices above show that the Gaussian beam is only astigmatic within the region of between the cylindrical lenses and unchanged outside of the telescope. If the beam reflected from the cavity is well mode matched to the cylindrical telescope, then a mode converter will introduce an astigmatism and vary the separate Rayleigh ranges [7],

$$\frac{z_{R,x}}{z_{R,y}} = \frac{1 + d/f}{1 - d/f} \quad (5.7)$$

Of course, the tuning of  $\theta$ ,  $d$  and  $f$  is left up to the optical designer's choice. The obvious selection for  $\theta$  should rotate the output beam such that the pringle mode intensities are centered on the individual quadrant photodiodes. The choice of separation distance  $d$  and focal length  $f$  are a bit more subtle.

The second order coupling to higher order HG modes from mode mismatch creates a cylindrically symmetric intensity profile. This can be broken by creating a phase difference between HG20 and HG02 such that there is a relative sign flip. In Figure 5.3 of O'Neil [70], the only conversion that transforms the diagonal HG mode into a symmetric donut mode is with  $\Delta\Omega = \pi/2$ . This implies the converse is also true if one desires to transform the donut mode into an HG mode of the same order. Making this choice of phase propagation automatically constrains the optical setup and the second order mode along the lens axis will see a phase advance equal to

$$\frac{\pi}{2} = 2 \left[ \tan^{-1} \left( \frac{d}{z_{R,x}} \right) - \tan^{-1} \left( \frac{d}{z_{R,y}} \right) \right] \quad (5.8)$$

$$\Rightarrow \sqrt{2} - 1 = \frac{d}{z_{R,y}} = \frac{z_{R,x}}{d} \quad (5.9)$$

The equation above only shows a relation between the Rayleigh ranges and the lens separation. However, by imposing mode matching conditions it is possible also constrain the focal

length of the cylindrical lenses as well.

$$f = \left[ \frac{1}{R_x(d)} - \frac{1}{R_y(d)} \right]^{-1} = \frac{d}{\sqrt{2}} \quad (5.10)$$

where  $R_i(d) = d[1 + (\frac{z_{R,i}}{d})^2]$ .

### Extracting information from mode

Mueller et al [67] showed that the error signal from mode mismatch could be extracted by using an RF detection scheme. Using this formalism, the error signal on a quadrant photodetector from a mismatched cavity after a mode converter is

$$\begin{aligned} S &\propto \text{Im} \left\{ \epsilon^* \left[ \int_{A1,A3} \hat{M}_{00}^\dagger \langle U_{00} | [\hat{M}_{U_{20}}^\dagger |U_{20}\rangle + \hat{M}_{U_{02}}^\dagger |U_{02}\rangle] - \right. \right. \\ &\quad \left. \left. \int_{A2,A4} \hat{M}_{00}^\dagger \langle U_{00} | (\hat{M}_{20}^\dagger |U_{20}\rangle + \hat{M}_{02}^\dagger |U_{02}\rangle) \right] \right\} \\ &\propto \text{Im} \left\{ \epsilon^* \left[ \int_{A1,A3} \langle U_{00} | (|U_{20}\rangle - |U_{02}\rangle) - \int_{A2,A4} \langle U_{00} | (|U_{20}\rangle - |U_{02}\rangle) \right] \right\} \end{aligned} \quad (5.11)$$

where the surface integrals are over each segment. In the above equation,  $\hat{C}_{ij}$  was chosen with  $\Delta\Omega = \pi/2$  and  $\hat{R}_{ij}$  should rotate the beams such that the intensities in Figure ModeConverter are aligned with the quadrant photodiodes.

### 5.2.3 DC Mode Matching

The benefit to using the RF sensing scheme for generating an error signal is the automatic reduction of the higher order mode content which can use actuators to adjust the incoming mode of the beam to whatever the cavity requires. This is particularly useful in areas where the laser power density is high and absorption on the high reflectivity surfaces cause thermal distortions in the cavity mode. However, the output mode cleaner remains generally fixed in its eigenbasis such that the nominal input mode is static; in fact, the current alignment scheme uses DC quadrant photodiodes to feed back to the OMC suspensions and the con-

trol loop offsets are tuned to minimize the 10/01 modes. If there was a low-noise way to continually measure the beam size at two different Gouy phases prior to entering the output mode cleaner, then there could be an error signal which would be used for thermal actuators directly after the signal recycling cavity. This can be achieved with bullseye sensors that read power ratio relatively quickly. Another interesting way of measuring the mode is using a slowly rotating razer blade with known angular frequency in front of a single photodiode and inferring the error function which will directly give the beam size.

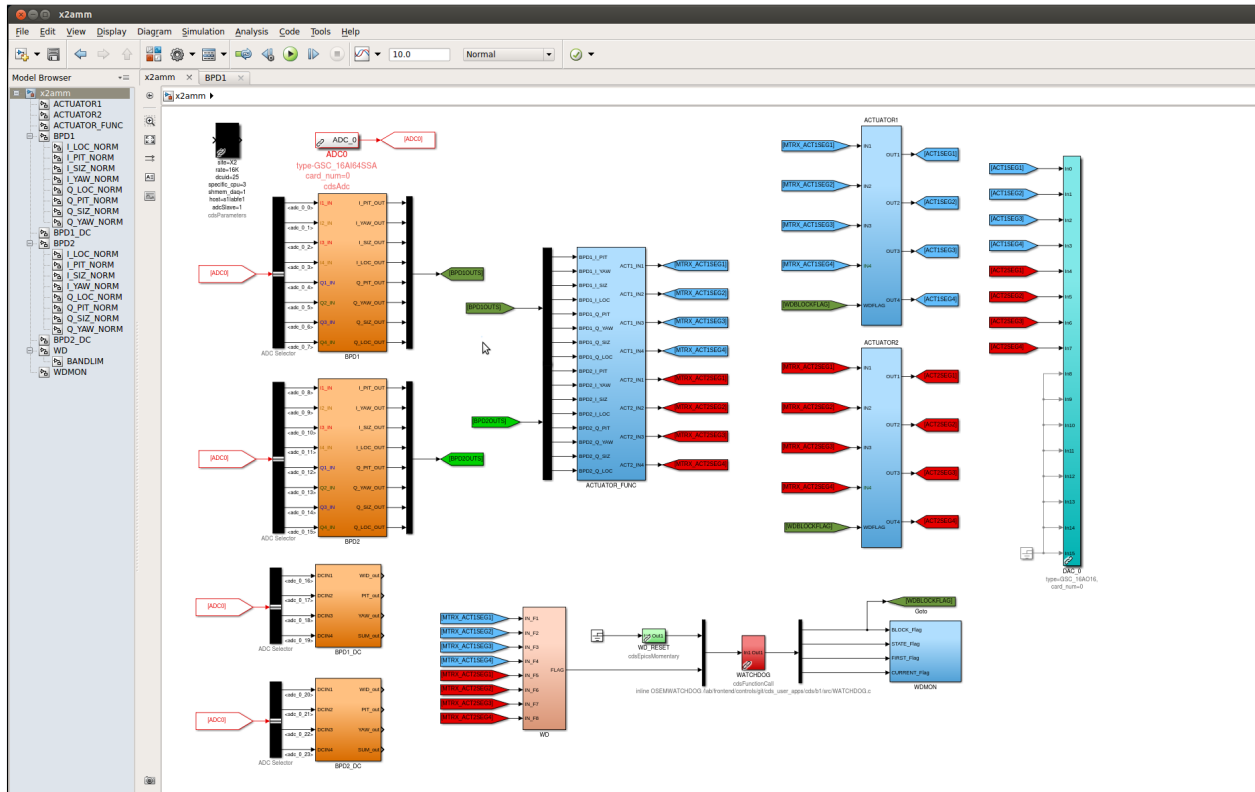


Figure 5.2: **Model overview for adaptive mode matching.** Using the LIGO digital system as a test bed for technology development has the advantage of easy integration at both LIGO sites. The Syracuse system uses a Simulink style model with LIGO standard modules to read in data from the analog-to-digital converter (ADC) that contain signals from each RF photodiode segments, apply a phase rotation to get the signal into one quadrature (nominally I for a linear cavity) and normalize by the total power on the sensor. Afterwards, the signals are sent to a master actuator function that diagonalizes the sensor signals into an actuators basis and sent to the digital-to-analog converter (DAC) to control the heater drivers.

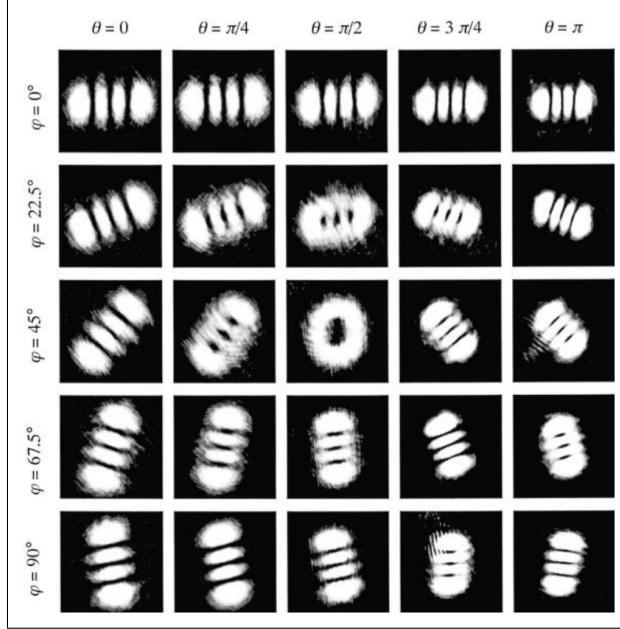


Figure 5.3: **Intensity profiles passing through a mode converter** [70]. The image in upper left corner represents the  $m = 3$  and  $n = 0$  Hermite Gauss (LG) mode which gets transformed through a converter for different rotations and phase advances. The only combination which gives a symmetric Laguerre Gauss (LG) mode is  $\phi = 45$  deg and  $\theta = \pi/2$ . This gives some intuition about how to reverse this process to take an input LG mode and breaks the cylindrical symmetry so that the modal content can be sensed by a quadrant photodiode.

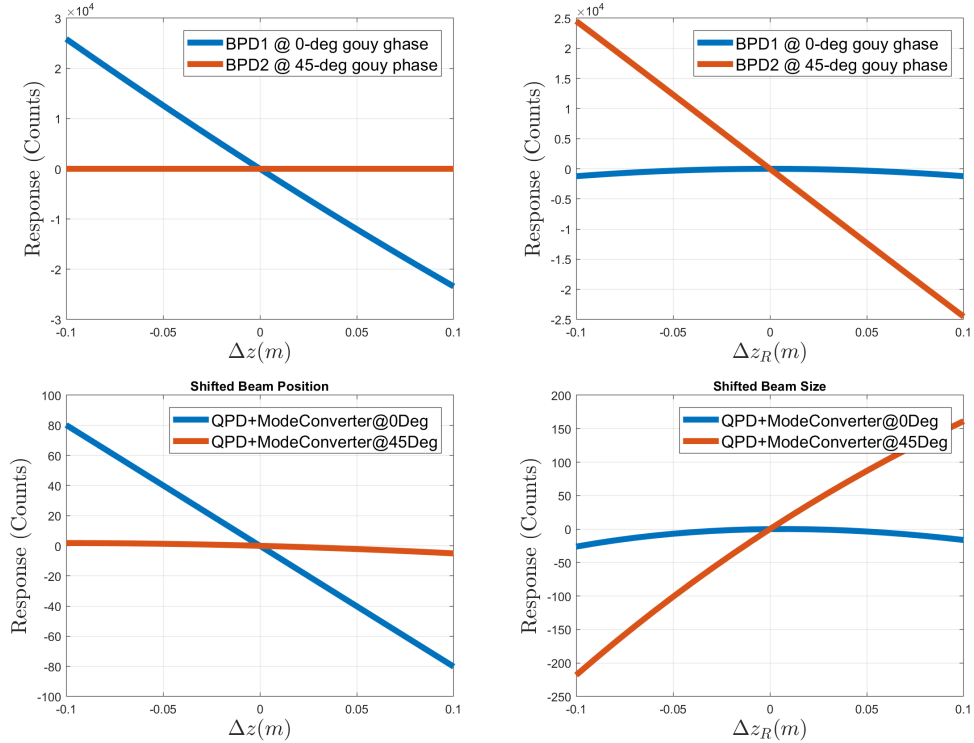


Figure 5.4: **Simulated error signals from MATLAB (QPD) and FINESSE (BPD).** A numerical simulation of the error signal in reflection from a linear Fabry Perot cavity with different detectors when varying either the waist position ( $\Delta z$ ) or Rayleigh range ( $\Delta z_R$ ). The error signal orthogonality at two different Gouy phases is demonstrated using both sensing schemes for active wavefront control.

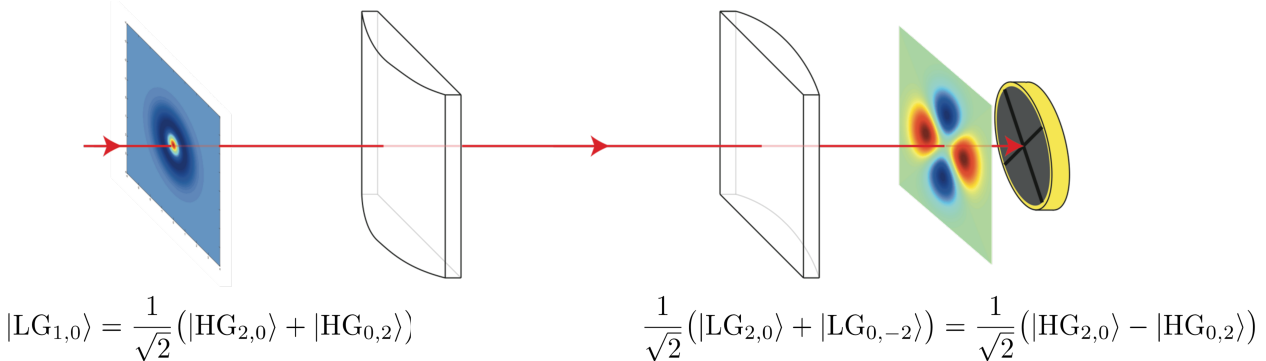


Figure 5.5: **Passing a bullseye mode through a  $\pi/2$  mode converter.** The reflected fields of a well aligned Fabry-Perot cavity with a slight mode mismatch will have a large contribution from the  $|HG_{20}\rangle + |HG_{02}\rangle$  mode which is cylindrically symmetric. After passing through a cylindrical telescope which has a  $\pi/2$  phase advance for one axis, there is a relative sign flip which breaks the symmetry and the error signal can be extracted with an RF quadrant photodiode.

# Chapter 6

## Wavefront Control at LIGO Hanford

Simulations and calculations are wonderful guides to understanding and building intuition about mode matching, however, no model is perfect and experiments have a way of presenting the most interesting and challenging problems. Preparation for the third observing run (O3) required extensive work to understand Advanced LIGO’s path to achieve higher arm power. One of the most important tasks was tuning the thermal compensation and interferometer sensing/controls systems in order to maintain the power build-ups in the PRC and arms during nominal low noise operation. This chapter will build some constructs on how lensing affects the interferometer fields and a few strategies to tune the Thermal Compensation System (TCS) at LIGO Hanford. Then summarizing a few in-situ measurements taken to understand the mode content at the output mode cleaner in single bounce configuration

For Advanced LIGO, optic heating comes from two sources: one main source is absorption by arm cavity optics from the main interferometer beam and another source is the effects of TCS which are meant to combat the wavefront distortion by applying heat in key places. Thermal compensation currently utilizes ring heaters at all four main test masses, a disk heater at the SR3, and CO<sub>2</sub> lasers at the input test masses.

## 6.1 Hot vs. Cold Interferometers

When fully operational, the arm cavities can have approximately 150 kilowatts of circulating power. An estimated but useful description of the total arm power in each arm is

$$P_{\text{ARM}} \approx \frac{1}{2}(g_{\text{PRC}} * g_{\text{ARM}} * P_{\text{in}}) \quad (6.1)$$

where  $g_{\text{PRC}} \approx 45$  is the power recycling cavity gain and  $g_{\text{ARM}} \approx 225$  is the single arm cavity gain. For O3, the intended input power  $P_{\text{in}}$  will reach approximately 30 W which means  $P_{\text{ARM}} \approx 150,000$  W. A fraction of that power between 0.2-0.8 PPM, will be absorbed by the high reflectivity surface creating a *thermo-elastic* effect which changes the radius of curvature. By changing the test mass curvatures, the resonant Gaussian mode will also change its profile. Additionally, the *thermo-refractive* effect will vary the index of refraction within the bulk as a function of absorbed temperature which creates a thermal lens that turns out to be an order of magnitude larger than the wavefront distortion from therm-elastic effects in fused silica [89].

### 6.1.1 Thermal Lensing

As seen in Section 2.0.5, the sideband and carrier frequencies propagate differently in the interferometer by design, which means their fields see different thermal lensing effects. The ITM substrate which sees the thermo-refractive change from absorption will play the largest role because the carrier is not affected to first order, this will be shown in Section 6.1.1. To understand how the fields change, the easiest way is to invoke the ABCD transfer matrix approach to track how the phase changes as they propagate through the optical system [60].

#### Carrier

The carrier is resonant in the 4 kilometer arm cavities as well as the PRC, so a simplified model resembles a coupled cavity setup where there is already a locked resonator with some

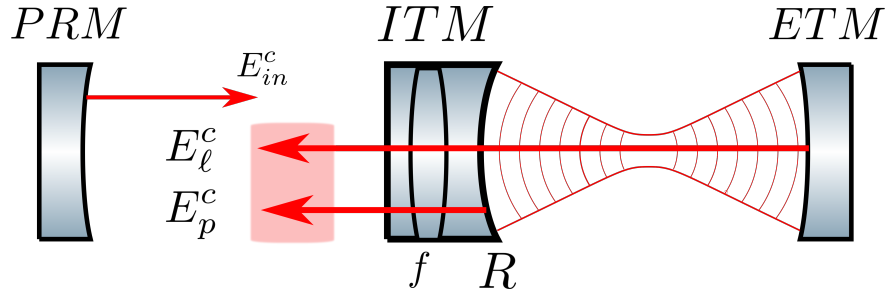


**Figure 6.1: A simplified model for the effect of a substrate thermal lens on the carrier field.** An input beam,  $E_{in}^c$ , from the power recycling mirror (PRM) will have a radius of curvature that mode matches to the input test mass (ITM). The promptly reflected beam,  $E_p^c$ , is denoted by equation 6.4 and the leakage beam,  $E_\ell^c$ , is expressed by equation 6.5 where the sum of them would make the total reflected beam. The leakage field will have the same shape as the ITM radius of curvature  $R$  when exiting the arm and see the thermal lensing  $f$ . The promptly reflected field will also see the lens  $f$  twice but when combined with the leakage beam, the *total* reflected field is not affected by the thermal lens.

leakage beam and there is an input mode propagating from the power recycling cavity. Consider the diagram in Figure 6.1, a two-mirror optical system which has an input carrier beam,  $|E_{in}^c\rangle$ , that has a portion promptly reflected off the input mirror to create  $|E_p^c\rangle$

$$|E_p^c\rangle = \hat{M}_p^c |E_{in}^c\rangle \quad (6.2)$$

The prompt reflection is made up of a beam incident on a converging lens(-) from the substrate and a single reflection from the input coupler's convex(+) surface, therefore, the transfer matrix is

$$\hat{M}_p^c = \begin{bmatrix} 1 & 0 \\ -\frac{1}{f} & 1 \end{bmatrix} \begin{bmatrix} 1 & 0 \\ +\frac{2}{R} & 1 \end{bmatrix} \begin{bmatrix} 1 & 0 \\ -\frac{1}{f} & 1 \end{bmatrix} \quad (6.3)$$

where  $R$  is the radius of curvature of the high reflectivity surface and  $f$  is the focal length of the mirror substrate. In general, this can be a combination of the static lens and any thermal effects which create additional (intentional or non-intentional) lensing.

$$|E_p^c\rangle = \hat{M}_p^c \begin{bmatrix} 1 \\ \frac{1}{q_{in}} \end{bmatrix} = \begin{bmatrix} 1 \\ \frac{1}{q_{in}} + 2\left(\frac{1}{R} - \frac{1}{f}\right) \end{bmatrix} = \begin{bmatrix} 1 \\ \frac{1}{q_p} \end{bmatrix} \quad (6.4)$$

In addition, there is also a circulating field inside the cavity which leaks out can be denoted by  $|E_\ell^c\rangle$  which exits with the input coupler's radius of curvature and sees a single pass through the substrate lens,

$$|E_\ell^c\rangle = \begin{bmatrix} 1 & 0 \\ -\frac{1}{f} & 1 \end{bmatrix} \begin{bmatrix} 1 \\ \frac{1}{R} \end{bmatrix} = \begin{bmatrix} 1 \\ \frac{1}{R} - \frac{1}{f} \end{bmatrix} \quad (6.5)$$

The total reflected beam is a summation of the prompt and leaked cavity fields. LIGO uses arms which are highly over-coupled optical cavities so the promptly reflected amplitude is  $|E_p^c| \approx |E_{in}|$  and using equation 2.15, the leakage amplitude is  $|E_\ell^c| \approx -2|E_{in}|$ . Putting all this together, the total reflected field of the carrier is

$$\begin{aligned} E_{REFL}^c &= E_\ell^c + E_p^c \\ &= E_{in} \left[ \exp\left(\frac{-ikr^2}{2q_p}\right) - 2\exp\left(\frac{-ikr^2}{2q_\ell}\right) \right] \\ &\approx E_{in} \left[ -1 - \frac{ikr^2}{2} \left( \frac{1}{q_p} - \frac{2}{q_\ell} \right) \right] \\ &\approx -E_{in} \exp\left(\frac{ikr^2}{2q_{in}}\right) \end{aligned} \quad (6.6)$$

This shows that the total reflected carrier field will be the original amplitude with a negative sign and the same absolute curvature, however, now the beam is diverging instead of converging. **The amazing part is that the end result is independent of the substrate lensing to first order.** The point where this model breaks down is when the power recycling mode is altered so much by the lens that it is no longer well matched to the arms such that the input beam does not have the right radius of curvature. At this point, there will be extra losses from higher order mode-coupling. Also, if the lensing becomes so bad that the radius of curvature shifts the PRC g-factors such that the resonant mode is no longer

geometrically stable (see Appendix A), however, this requires significant thermal lensing well beyond what is expected in Advanced LIGO [60]. A numerical FINESSE model uses this simplified geometry to calculate the power recycling gain and arm build up in Figure 6.16 as a function of round trip losses and thermal lensing.

### Sidebands

Using the same formalism as the carrier fields, the sidebands will have the same input curvature, however, they do not resonate in the arms so there is no cavity leakage field. Therefore, the sidebands will see the phase change due to the substrate lens and this has very important consequences on the sideband build up within the power recycling cavity.

### GW Signal

As mentioned in Section 2.0.5, LIGO currently employs a DC readout scheme that extracts the signal by beating the carrier field with the audio frequency sidebands created by the gravitational wave. Although the carrier field was shown to be immune from substrate thermal lensing, the gravitational wave sideband field will see a single-passed lensing effect as it propagates out of the cavity and towards the beamsplitter. If there is differential lensing, the signal recycling cavity will see an effective thermal lens,  $TL_-$ , which will be scattered into higher order modes. This reduces the amount of gravitational wave signal at the anti-symmetric port that is directly proportional to the mode mismatch between the arms.

## 6.2 Wavefront Distortions from Thermal Effects

In the previous section, it was shown that lensing in the substrate affects fields in the interferometer differently. The thermal distortions were modeled as a simple addition of phase, however, it is useful to understand how the optical path varies from first principles. This

provides theoretical groundwork for modeling interferometer heating as well as corrective measures using TCS. A lot of work in this field was introduced in the context of gravitational wave detectors by Hello and Vinet [52] [85] where they implemented the Heat Diffusion equation in order to analytically derive the phase change due to thermal aberrations. In general, there are two effects which occur when a beam interacts with an optic which has a temperature field: thermo-refractive and thermo-elastic.

The first arises from the index of refraction changing as a function of the temperature distribution  $T(r, z)$ ,

$$\Delta n_r(r, z) = \frac{dn}{dT} T(r, z) \quad (6.7)$$

where  $\frac{dn}{dT}$  is the temperature index coefficient and is dependent on the optic material. For example, if the heating source comes from a laser beam which imparts onto the optic a Gaussian-like intensity pattern, the temperature profile will be non-uniform and lead to a varying index of refraction that causes wavefront distortions (see Figure 6.2).

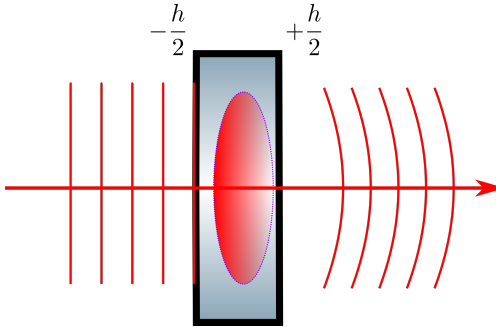


**Figure 6.2: A plane wave passing through a lens with a temperature gradient.** The index of refraction,  $n$ , depends on the material and temperature so when a plane wave moves through a medium with a non-uniform temperature field, a phase lag or lead occurs in the wavefront. Since  $\frac{dn}{dT}$  is negative, the distortion will resemble a diverging lens.

To understand how changing the index of refraction varies the optical path length, consider the function  $S(r)$  which describes surfaces that are perpendicular to the rays. If  $S(r)$  is a known function then the rays can be reconstructed using the gradient,  $\nabla S(r)$ . As an analogy to electrostatics,  $S(r)$  is similar to the potential function  $V$  and the electric field is

described by  $E = -\nabla V$ . As an extension of ray optics, Fermat's principle requires that the Eikonal equation be satisfied,

$$|\nabla S|^2 = n^2 \quad (6.8)$$

By integrating along the axis of propagation ( $\hat{z}$ ) in Figure 6.2 through the substrate, one can find the optical path distortion

$$Z(r) = \frac{dn}{dT} \int_{-h/2}^{+h/2} T(r, z) dz \quad (6.9)$$

It is clear that the temperature field is key to understanding exactly how the wavefront is distorted. In order to analytically solve for  $T(r, z)$ , one must invoke the famous Heat equation,

$$\kappa \nabla^2 T(r, z) = \rho C \frac{\partial T}{\partial t} \quad (6.10)$$

where  $\kappa$  is the thermal conductivity,  $\rho$  is the density, and  $C$  is the specific heat. A complete solution for such an equation will be a sum of two parts:

$$T(r, z, t) = T_s(r, z) + T_t(r, z, t) \quad (6.11)$$

where the first term is the steady-state solution which includes the an ambient temperature and a perturbation,  $T_s(r, z) = T_p(r, z) + T_0$ . The main goal for the remainder of the section will be finding a solution to the perturbation field. The second term is the transient time-dependent solution which will converge to the steady-state as time goes to infinity. For the LIGO test masses which are approximately cylindrical, the heat equation in steady-state equilibrium is

$$\kappa \left[ \frac{1}{r} \frac{\partial}{\partial r} \left( r \frac{\partial}{\partial r} \right) + \frac{\partial^2}{\partial z^2} \right] T_s(r, z) = 0 \quad (6.12)$$

The next step is to understand the boundary conditions using Figure 6.3 and the balance of

heat fluxes at each of the surfaces,

$$\mathbf{n} \cdot [\mathbf{F} + \kappa \nabla T_s]_{\text{surf}} = 0 \quad (6.13)$$

Assuming that the outward flux is from radiation which follows the Stefan-Boltzmann law,

$$\begin{aligned} \mathbf{n} \cdot \mathbf{F}_{t_{\text{surf}}} &= \sigma_B [T_s^4 - T_0^4] = \sigma_B [(T_p(r, z) + T_0)^4 - T_0^4] \\ &\approx 4\sigma_B T_0^3 T_p(r, z) \end{aligned} \quad (6.14)$$

where  $\sigma_B$  is the Stefan-Boltzmann's constant. It is important to note that  $\sigma_B$  depends on the material and may vary by a scalar amount but for brevity, it is used as a constant here. The last part of the equation assumes that the temperature field is only a small perturbation from the ambient surroundings,  $T_p(r, z) \ll T_0$ , which allows the radiation term to become linear. Figure 6.3 shows boundary conditions for the LIGO test masses,

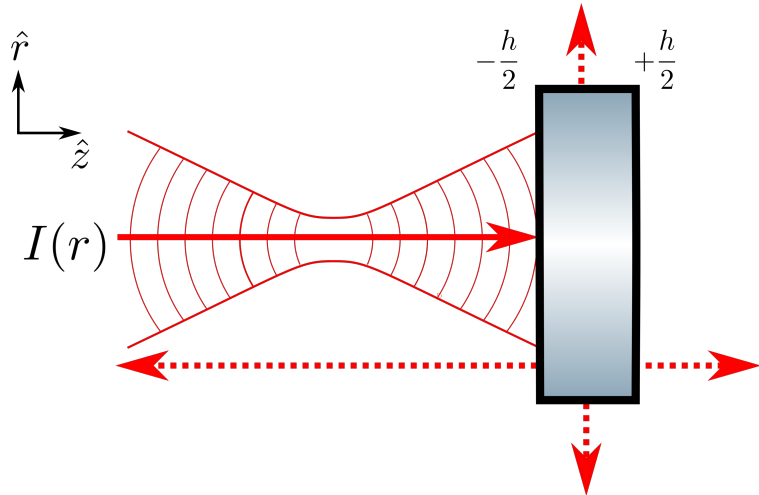


Figure 6.3: **A conceptual model of flux balance for a cylindrical object.** The red dotted lines represent the radiative fluxes escaping the optic while a Gaussian beam with intensity profile  $I(r)$  is pumping energy in as denoted by the red solid line.

At the surface where  $z = h/2$  the total flux is radiative,

$$-\kappa \frac{\partial T_p(r, h/2)}{\partial z} = 4\sigma_B T_0^3 T_p(r, h/2) \quad (6.15)$$

At the barrel of the cylinder where  $r = a$ , total flux is also radiative,

$$-\kappa \frac{\partial T_p(a, z)}{\partial r} = 4\sigma_B T_0^3 T_p(a, z) \quad (6.16)$$

At the surface where  $z = -h/2$  there are two components of flux, one is radiative and the second is the input power from the laser beam striking the optic surface,

$$-\kappa \frac{\partial T_p(r, -h/2)}{\partial z} = -4\sigma_B T_0^3 T_p(r, -h/2) + \epsilon_a I(r) \quad (6.17)$$

where  $I(r) = \frac{2P}{\pi w^2} \exp\{-2r^2/w^2\}$  is the laser beam intensity with power  $P$  over a beam size of  $w$  and  $\epsilon_a$  is the absorption coefficient. Here, the radiative term has a negative sign to represent the flux direction. Once boundary conditions are established, most introductory textbooks that deal with partial differential equations will apply an educated guess for the solution. In this case, the resulting temperature field will be a harmonic function,

$$T_p(r, \phi, z) = (Ae^{+kz} + Be^{-kz}) J_0(kr) \quad (6.18)$$

where  $J_0$  is the spherical Bessel function of the first kind and  $k$  is a constant. Although this particular temperature distribution can be even more general by allowing all the orders of  $J_n$ , this form is sufficient. Using the boundary condition from 6.16 and the property  $\frac{\partial J_0(x)}{\partial x} = -J_1(x)$ ,

$$-\kappa k \frac{\partial J_0(kr)}{\partial r} \Big|_{r=a} = 4\sigma_B T_0^3 J_0(ka) \quad (6.19)$$

$$ka J_1(ka) - \chi J_0(ka) = 0 \quad (6.20)$$

where  $\chi = 4\sigma T_0^3 a / \kappa$  is the reduced time constant. There exists an infinite number of discrete solutions which can solve 6.20 using various values of  $k_n a = \rho_n$ . The temperature field then becomes,

$$T_p(r, z) = \sum_{n=0}^{\infty} (A_n e^{+k_n z} + B_n e^{-k_n z}) J_0(k_n r) \quad (6.21)$$

In order to solve the conditions from equations 6.15 and 6.17, the strategy is use the orthogonality of the spherical Bessel functions in order to expand the equations into a solvable algebraic form. This will include expanding the intensity profile  $I(r)$  in this basis as well. Consider the boundary from  $r = 0$  to  $r = a$ , the functions  $J_0(k_n r)$  form a complete basis set and the normalization constant is given by the Sturm-Louisville problem,

$$\int_0^a J_0(k_n r) J_0(k_m r) r dr = \delta_{mn} \frac{[\chi^2 + (k_n a)^2]}{2k_n^2} J_0^2(k_n a) = \delta_{mn} \frac{1}{N_n} \quad (6.22)$$

Then expanding the intensity profile in terms of the Bessel function:  $I(r) = \sum_n^\infty p_n J_0(k_n r)$  and inverting to solve for  $p_n$  leads to,

$$\begin{aligned} p_n &= N_n \int_0^a I(r) J_0(k_n a) r dr \\ &= N_n \int_0^a \left[ \frac{2P}{\pi w^2} \right] J_0(k_n a) \exp\{-2r^2/w^2\} r dr \\ &\approx N_n \frac{P}{2\pi a^2} \exp\left\{-\frac{(k_n w)^2}{8}\right\} \end{aligned} \quad (6.23)$$

The approximation came from integrating to infinity instead of  $a$  which is reasonable if diffraction losses are small on the substrate. Plugging in the equation 6.21 and  $I(r)$  into the remaining boundary conditions,

$$\left[ k_n - \frac{4\sigma_B T_0^3}{\kappa} \right] e^{-k_n h} A_n - \left[ k_n + \frac{4\sigma_B T_0^3}{\kappa} \right] B_n = \frac{\epsilon p_n}{\kappa} e^{-k_n h/2} \quad (6.24a)$$

$$\left[ k_n + \frac{4\sigma_B T_0^3}{\kappa} \right] A_n - \left[ k_n - \frac{4\sigma_B T_0^3}{\kappa} \right] B_n e^{-k_n h} = 0 \quad (6.24b)$$

Solving for  $A_n$  and  $B_n$ ,

$$A_n = \frac{\epsilon_a p_n}{\kappa} e^{-3k_n h/2} \frac{\eta_+}{\eta_+ - \eta_- e^{-2k_n h}} \quad (6.25a)$$

$$B_n = \frac{\epsilon_a p_n}{\kappa} e^{-k_n h/2} \frac{\eta_-}{\eta_+ - \eta_- e^{-2k_n h}} \quad (6.25b)$$

where  $\eta_\pm = k_n \pm \frac{4\sigma_B T_0^3}{\kappa}$  is used for brevity. Now it is possible to write down the entire

steady-state temperature field for a cylindrical test mass with a laser beam impinging on the surface,

$$T_p(r, z) = \sum_{n=0}^{\infty} \frac{\epsilon_a p_n}{\kappa} \frac{\eta_- e^{-k_n(3h/2-z)} + \eta_+ e^{-k_n(h/2-z)}}{\eta_+ - \eta_- e^{-2k_n h}} J_0(k_n r) \quad (6.26)$$

Once the temperature profile is solved, the path length distortion from the thermo-refractive effect can be found by solving by equation 6.9,

$$Z_{\text{TR}}(r) = \frac{dn}{dt} \frac{\epsilon_a}{\kappa} \sum_{n=0}^{\infty} \frac{p_n}{k_n} \frac{1 - e^{-k_n h}}{[\eta_+ - \eta_- e^{-k_n h}]} J_0(k_n r) \quad (6.27)$$

where  $p_n$  contains information about the heating profile so it is possible to directly plug in equation 6.23 to represent the distortion from a Gaussian beam,

$$Z_{\text{TR}}^G(r) = \frac{dn}{dt} \frac{\epsilon_a P}{2\pi a^2 \kappa} \sum_{n=0}^{\infty} \frac{N_n}{k_n} e^{-(k_n w)^2/8} \frac{1 - e^{-k_n h}}{[\eta_+ - \eta_- e^{-k_n h}]} J_0(k_n r) \quad (6.28)$$

The thermo-refractive effect due to coating and substrate absorption is only one type, there is also an effect which elastically curves the surface from thermal expansion [85]. This thermo-elastic effect deals with the internal stresses of the material and employs the stress-strain relations in order to derive the wavefront curvature. For the LIGO test masses which use fused silica, this effect is smaller than the thermo-refractive wavefront distortion by about an order of magnitude.

## 6.3 Contrast Defect

Generally, the contrast defect is defined as the ratio of power between the antisymmetric port and the reflected port when locked on a dark fringe. In other words, it is the amount of junk light that is present in the interferometer when light between the two arms do not perfectly interfere with each other. This junk light can be the symptom of various causes, for example, an imbalance of reflectivity between ITMX and ITMY will cause non-perfect destructive interference at the antisymmetric port and a camera would see a TEM00 beam

when locked on length. Another cause of contrast defect could be from misalignment between the ITMs or beamsplitter which will result in seeing a TEM 01/10 mode. However, if both of the aforementioned causes are fixed with a combination of stringent design specifications for the reflectivity and alignment loops closed to minimize angular jitter, then the contrast defect will be dominated by mode mismatch which can be fixed by a combination of ring heaters and CO<sub>2</sub> lasers. The picture gets even more complicated when adding in the absorption for individual optics and introducing multiple Fabry-Perot cavities which will treat the sidebands and carrier fields differently. One of the main goals for the Thermal Compensation System is to correct the cold and hot interferometer differences in radii of curvature.

### 6.3.1 Simple Michelson Contrast Defect

The simple Michelson can give a first estimate of the contrast defect when starting to commission the interferometer's thermal system, however, it is not used in nominal low noise since the dual-recycled Michelson is implemented. By propagating the input mode cleaner beam to the beamsplitter and taking a single bounce at the high reflectivity surface, one can approximate the resultant mode overlap by measuring the power at the antisymmetric port. The static mismatch correction was measured this way and is compensated using one of the CO<sub>2</sub> lasers to reduce the contrast at 2 Watts of input power from 0.4% to 0.1% [? ].

At this point the carrier and sideband fields follow the same ABCD matrix transfer function, so only one calculation is needed to estimate the contrast defect. A keen reader will notice that this model will not take the Schnupp asymmetry into account which allows the  $\hat{x}$ -direction beam to travel an extra 8 centimeters further than the  $\hat{y}$ , however, this effect will only change the end result by approximately 10%. In fact, for this interferometer configuration, the dominate source of mismatch will be from the prompt reflection off the HR surfaces of the ITMs where most of the phase change occurs. The sideband contribution at the antisymmetric port can be estimated by using equation 2.7 and measuring the modulation

depth,  $\Gamma_\Omega$ , for the 9 and 45 MHz RF fields that enter the interferometer,

$$\begin{aligned} P_{\text{SB}} &= 2P_{\text{in}} \left( \frac{\Gamma}{2} \right)^2 t_{\text{SB}\pm} \\ &= 2P_{\text{in}} \left( \frac{\Gamma}{2} \right)^2 \sin^2(k_\Omega \Delta\ell) \end{aligned} \quad (6.29)$$

Additionally, the beamsplitter RMS motion will also contribute extra power at the AS and can be estimated by calculating the coupling coefficient from the 00 to 01 HG mode,

$$P_{01} = 2P_{\text{in}} \left( \frac{\pi \alpha w(z)}{\lambda} \right)^2 \quad (6.30)$$

where  $w(z)$  is the beam size on the test mass and  $\alpha$  is the misalignment RMS.

### 6.3.2 Modal Contrast Defect

During full lock, the formalism must be extended to include the mode shape of two arm cavities interfering at the beamsplitter. Using the Laguerre-Gauss modes is useful for brevity because the mode mismatch couples to only one higher order mode. Contrast defect can be defined using the zeroth eigenmode of each arm and then expanded to project the X-arm's basis onto Y-arm using higher order LG modes,  $LG_y^{00} \rightarrow LG_x^{00} + \alpha LG_x^{10}$ . Where  $\alpha = \frac{1}{\sqrt{2}} \left( \frac{\Delta\omega_0}{\omega_0} + i \frac{\Delta z}{z_R} \right)$  is the amount of higher order mode coupling due to mismatch in beam size and location, respectively (see Chapter 3).

$$\begin{aligned} \text{CD} &\equiv \frac{P_{\text{AS}}}{P_{\text{REFL}}} \\ &= \frac{|LG_x^{00} - LG_y^{00}|^2}{|LG_x^{00} + LG_y^{00}|^2} \\ &= \frac{|LG_x^{00}|^2 + |LG_x^{00} + \alpha LG_x^{10}|^2 - 2 \text{Re}(LG_x^{00}[LG_x^{00*} + \alpha LG_x^{10}])}{|LG_x^{00}|^2 + |LG_x^{00} + \alpha LG_x^{10}|^2 + 2 \text{Re}(LG_x^{00}[LG_x^{00*} + \alpha LG_x^{10}])} \\ &\approx \frac{\alpha^2}{4} \\ &\approx \frac{1}{8} \left[ \left( \frac{\Delta\omega_0}{\omega_0} \right)^2 + \left( \frac{\Delta z}{z_R} \right)^2 \right] \end{aligned} \quad (6.31)$$

Mismatch between the arm cavities can stem from a few sources such as the difference between the radii of curvature on the high reflectivity surfaces that will cause the resonant modes to be shaped differently between the X-arm and Y-arm. LIGO tries to optimize this effect by pairing the optics based on their properties, however, during the upgrades from O2 to O3 at Hanford, ITMX was replaced but ITMY was not which lead to a static mismatch between the input test masses.

## 6.4 Tuning Thermal Compensation for LIGO

Goals: A path to higher power with preloading [89] [83]

As mentioned in Section 6.1.1, the circulating power in each of the arms can be close to 150 kW for O3 and higher for the next observation runs. Even with absorption estimates between 0.2 – 0.8 parts per million, the induced substrate lensing can be significant. The Thermal Compensation System (TCS) [60] [17] was developed to correct the wavefront by applying heat to cancel the deformities caused by interferometer heating. Lock acquisition and gravitational-wave optimization are the main metrics for success when commissioning most LIGO systems. To aid in the former, TCS is required to thermally lens the substrate between the beamsplitter and high-reflectivity surfaces of the test masses such that the optical path difference is optimized for the carrier and sideband power recycling gains. Both deal heavily with mode-matching the arm cavities such that overlap between the Gaussian modes is maximized.

To optimize the TCS settings for the best power build-ups, there are two separate strategies: The first requires estimating the amount of absorption on the test masses with the Hartmann Wavefront Sensors to measure the optical path distortion induced by the interferometer during a lock loss. Then pre-load the ring heaters with the nominal settings which would cancel carrier beam's thermal absorption in the "hot" state. The ring heaters have a very long time constant (30 hours) to reach thermal equilibrium with a step response of

electrical power, so if there is compensation needed, the heaters must be energized at all times. However, turning them on will change the radius of curvature and induce a substrate lens (see Section 6.4.2) that has to be canceled out by the CO<sub>2</sub> (Carbon Dioxide) lasers which create a lens on the compensation plate of the quadruple pendulum. Since the CO<sub>2</sub> lasers have a time constant of approximately 0.5 hours, they can be turned up during lock acquisition and reduced as needed when the interferometer input power is increased. The second method is to use relevant interferometer RF signals at various ports to experimentally adjust the lensing commonly or differentially to maintain power recycling build-ups while increasing the interferometer input power. In principle, either method should lead to the same answer but in practice, both are used to find the nominal thermal compensation configuration.

#### 6.4.1 Hartmann Wavefront Sensors

All estimates of steady-state curvature changes due to heating by the main interferometer beam depend linearly on the absorption and this can be quite difficult to detect when the coating absorption are typically less than one part in a million.

In order to diagnose this effect, the Hartmann Wavefront Sensors (HWS) [13] [84] was a system developed by Adelaide and Caltech [15] [16] which use an auxiliary beams and charged-coupled imaging devices (CCD) to sense the wavefront distortions formed by heating from the interferometer beam during power up and a lock loss. Currently, there are four Hartmann sensors installed at each test mass, which are injected from the AR surface side of the optics. Technical constraints require the ITM HWSs optical paths to differ from the ETM HWSs but the concept is still the same, so for brevity, only the ITMs HWSs will be discussed in detail. In Figure 6.4, the system starts with an auxiliary super-luminous LED (SLED) beam being injected into the vacuum system and a telescope (Lens 1, Lens 2) which collimates/expands the beam to sample a space 200 mm in diameter on the test mass HR surface. The return beams are picked-off and sent to a CCD with a Hartmann

plate mounted on the front which effectively decompose the wavefront into individual rays. Using a wavefront from a previous time with a cold optic as a reference. The Hartmann code creates a gradient vector field between the two times which have information about thermal lensing, then numerically integrates the gradients to fit a wavefront distortion field. The algorithm then uses the Zernike polynomials as a single basis to represent the effect of the thermal lens. [14]

### Tuning the Hartmann Sensors

A source of systematic noise was from beam clipping in chamber on the ITMX HWS, see Figure 6.7. This creates fringes which are extremely sensitive to misalignment; one bandage that was applied to reduce this noise was to digitally mask the fringes so they do not confuse the fitting algorithms. Hand tuning must be done so the mask is wide enough and centered around the interferometer lensing but not so large that the Hartmann fitting is corrupted by the fringes. The aperture is very tight from baffles and are relatively far field from the CCD plane. Two in-air periscope mirrors with pico-motors were used for alignment but beam clipping could not be fully removed. This artifact was also found at LLO so it suggests a systematic error in the alignment scheme. A possible fix could be implemented by replacing an in-vacuum steering mirror with a pico-motor.

It was also found that the CCDs (Dalsa pantera 1m60) had a number of pixels which would create large spikes in their intensity counts and produce large artifacts in the gradient plots that corrupted the spherical lens fitting (see Figure 6.6). One of the requirements for the HWSs is a wavefront distortion resolution of 1.35 nm [17] and a single glitch could register a few orders of magnitude higher. A solution for this was implemented by using the dark images to locate the bad pixels by averaging the counts over a few minutes and finding all the pixels which have counts higher than a particular threshold, generally 1.5 times above the average ambient dark noise level (about 50 counts). The dark frames would be read in by the Hartmann code which has a module written by Adelaide that uses the dark images as

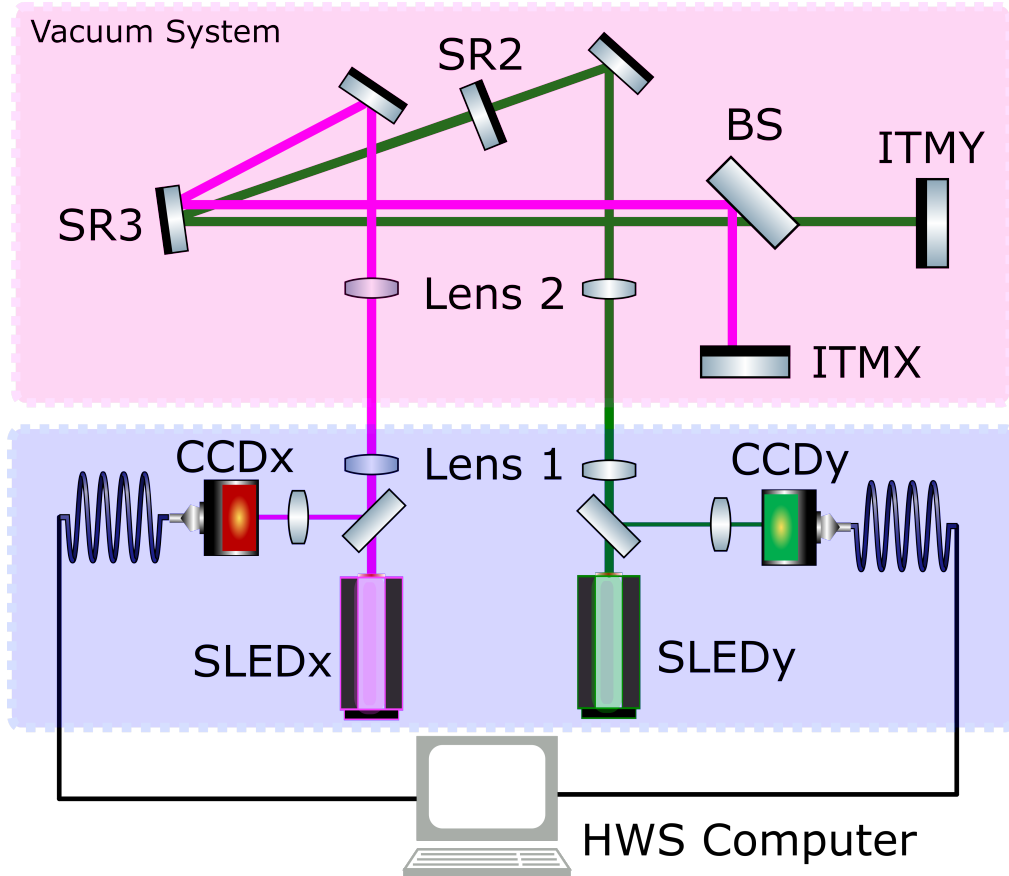


Figure 6.4: **ITM Hartmann sensors optical layout.** The path for injection is different for the two Hartmann sensors which use separate wavelengths to take advantage of the main beam splitter AR/HR surface reflectivity. The ITMX (magenta) and ITMY (green) probe beam wavelengths are 800 nm and 833 nm, respectively, and have a 40 nm linewidth [17]. The beams are sent into the vacuum system and retro-reflected off their respective optics back towards the pick-off mirrors before going into the CCDs with a Hartmann plate attached. The cameras are then sent via fiber to a computer that runs the analysis pipeline on the images and exports the data to EPICS so the users can interface with the real time digital system in the control rooms.

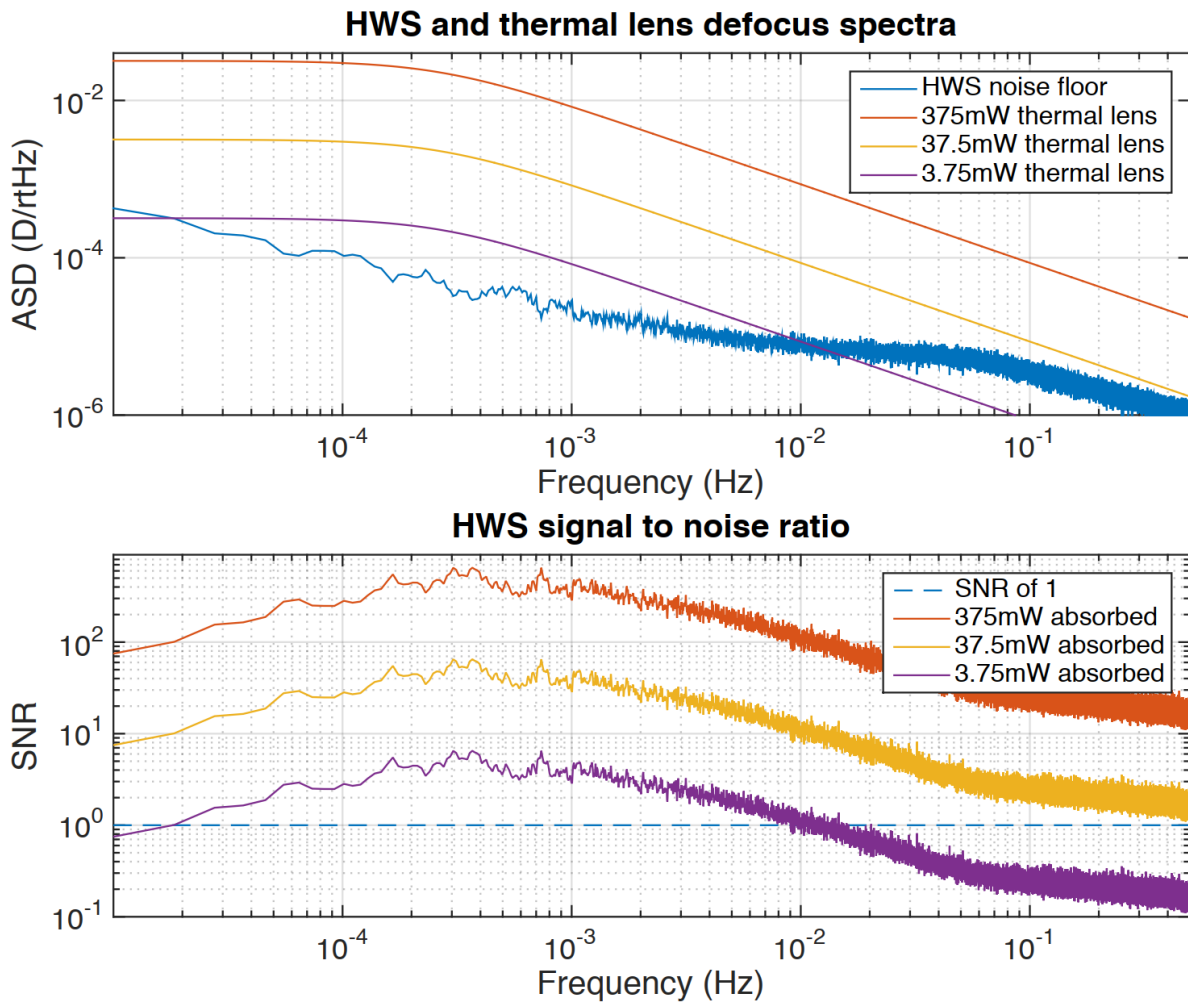
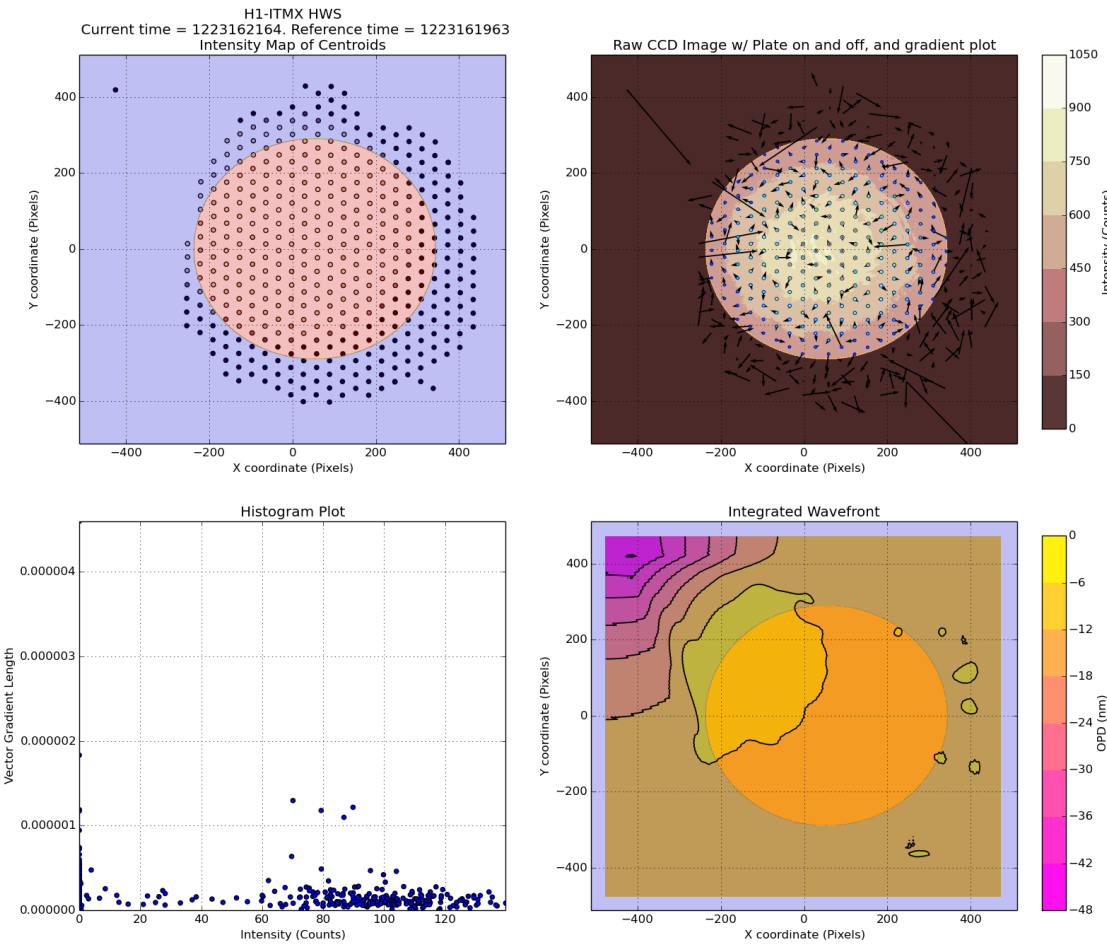


Figure 6.5: **Noise spectra for the HWS spherical lensing.** Taken from [17], this puts a lower bound on the Hartmann sensitivity to distortions for various time scales.



**Figure 6.6: ITMX Hartmann Sensor output.** Between the reference and current times for this measurement, no heating was applied to the test masses so the expectation is a relatively flat and smooth wavefront. This is mostly true except for a large, anomalous arrow at pixel coordinate  $[X,Y] = [-410, 405]$  of the gradient plots (upper right) which leads to a false wavefront distortion in the same area for the contour plot (lower right). The sharp iris in the middle represents a digital mask that is can be turned on to reduce the effects of fringing. A histogram in the bottom left plot shows the intensity distribution for each of the gradients; if the HWS beams are co-aligned well with the interferometer beam, then most of the information about thermal lensing occurs near the center of the intensity distribution.

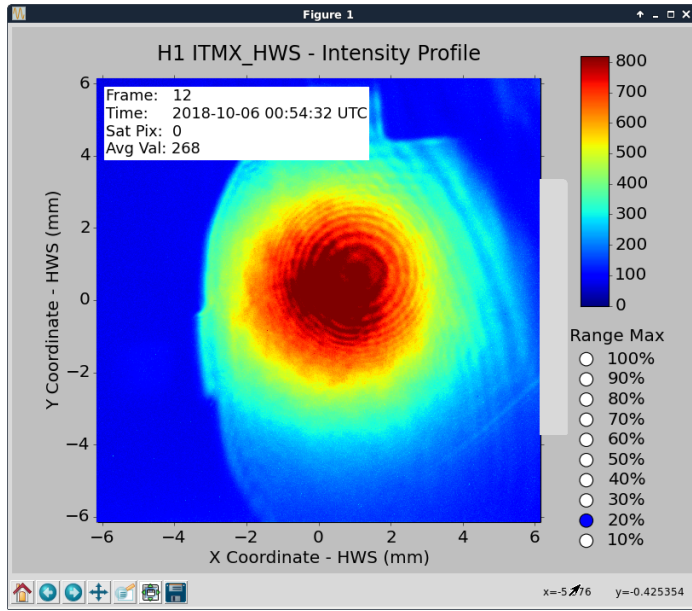


Figure 6.7: Clipping on ITMX Hartmann Sensor.

references to find the average of surrounding pixels and replace the problematic pixel. This digital procedure greatly reduced the amount of glitches found in the Hartmann sensor data.

When increasing the input power into the interferometer, there were large spikes associated with the spherical power estimation on the ITMX. This was eventually tracked down to leakage beam introduced by stray light from the interferometer. At times, the leakage beam was 40% the intensity of the main Hartmann beam which severely distorted the fitting algorithms. ITMY HWS did not see this effect because SR2 is such a good high reflector and attenuated any 1064 nm contributions down to the PPM level.

### Measuring Uniform Absorption

After the arm power drops suddenly, the heat decays exponentially depending on the amount of absorption on the high reflective surface of the arm cavity. Using the HWS, it is possible to fit the decay rate to a finite element model of a cylindrical mass. A fitted parameter for absorption is extremely important in pre-determining the amount compensation necessary to prepare the test masses for lock acquisition.

Applying a Markov Chain Monte-Carlo method allows some statistical uncertainty es-

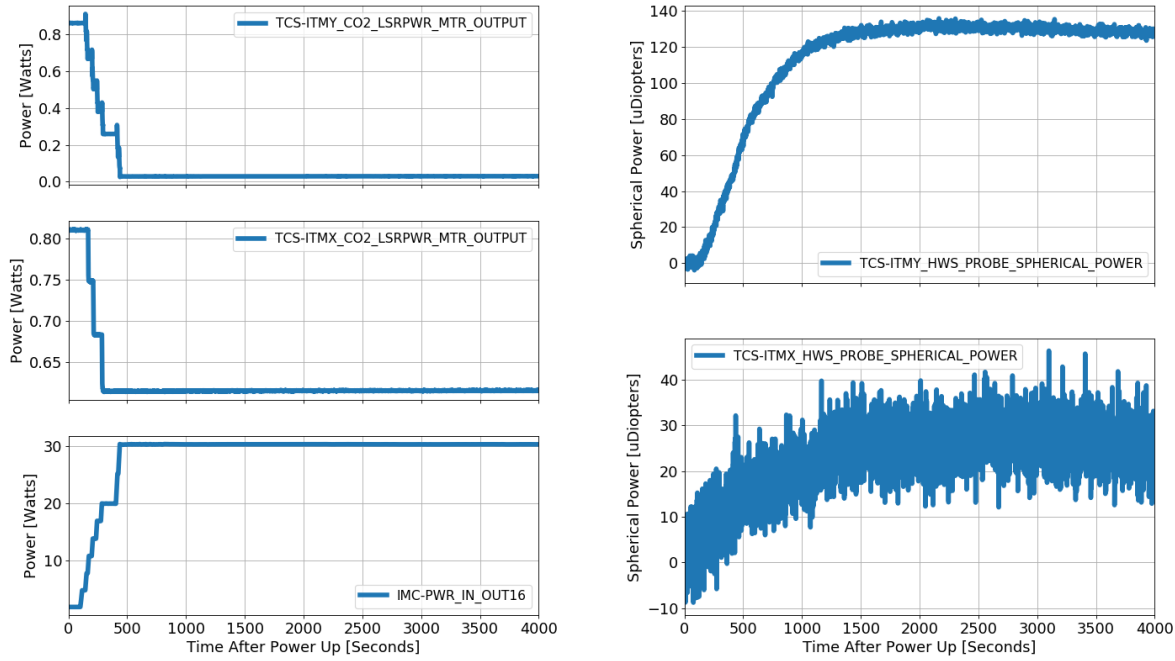


**Figure 6.8: A time series of the interferometer power increase sequence.** During this time, the interferometer is using DC-readout and locked at 2 watts of PSL input power with all of the angular control loops closed with high-bandwidth, in this configuration, the power recycling gain is approximately 45. The left figure shows the increase of PSL input power and the CO<sub>2</sub> lasers stepping down in power where levels of compensation were experimentally determined such that the angular control loops were stable and sideband build ups remained as high as possible. The right plot shows the Hartmann sensor spherical power as a function of time with the starting point scaled to zero micro-diopters. Although the point absorbers do not exhibit the same spatial structure as uniform heating so it is difficult to derive absolute absorption for ITMY, the spherical fitting gives some information about the relative scale of heating absorption between the two optics.

timates for the exponential fitting to the data shown in Figure 6.12, where the priors are assumed to be random Gaussian noise and the initial guesses are scaled roughly with a least squares fitting algorithm. Figure 6.11 shows the measured spherical power from interferometer heating for ITMX/ITMY and comparing the two optics shows that the spherical power difference for ITMY is almost a factor of 2 larger than ITMX. One of the main differences

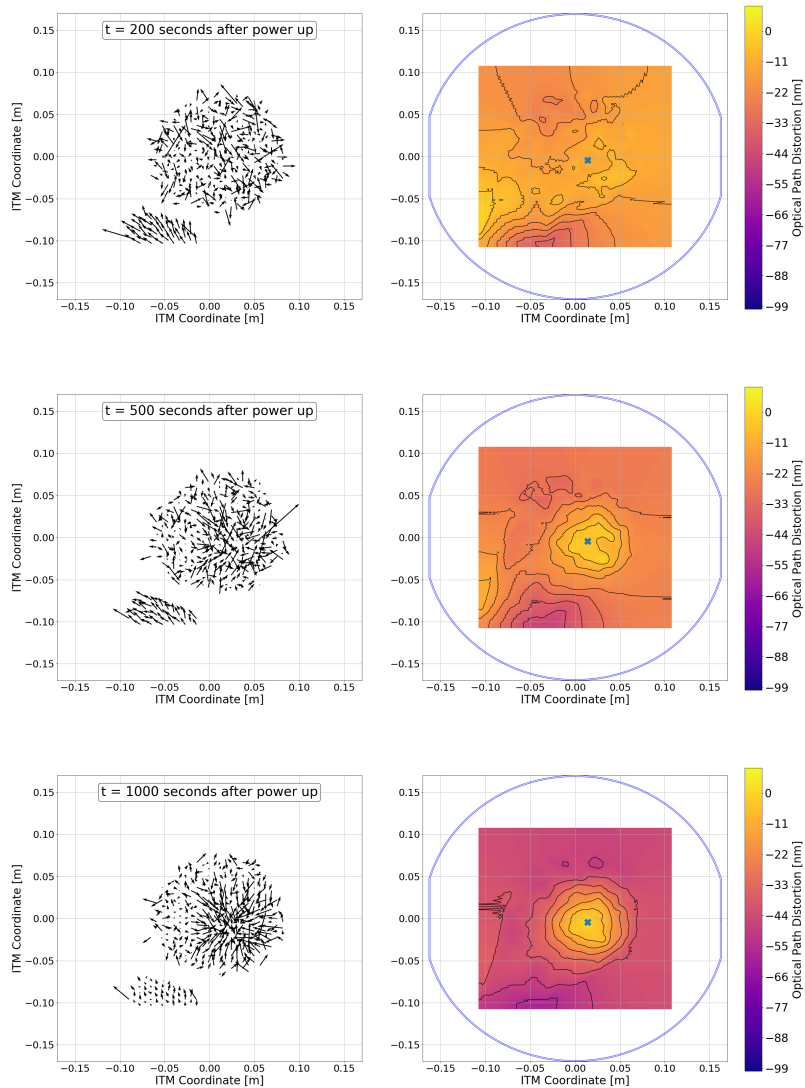


**Figure 6.9: ITMX gradient plots (left) and wavefront maps (right) during a power up to 30 Watts of input power.** It is important to note that there is a back-reflected stray beam from the super-luminous LED that is incident in the bottom left portion of the camera which is digitally cropped out during the real-time analysis. As previously noted, this particular Hartmann sensors suffers from beam clipping on the right side of the image which adds to the systematic noise. A blue cross denotes the origin which is fitted with the Zernike polynomials to derive a spherical power. The arrow lengths in the gradient plots are normalized to each individual plot and are meant to guide the eye in discerning the directionality and pattern of lensing.

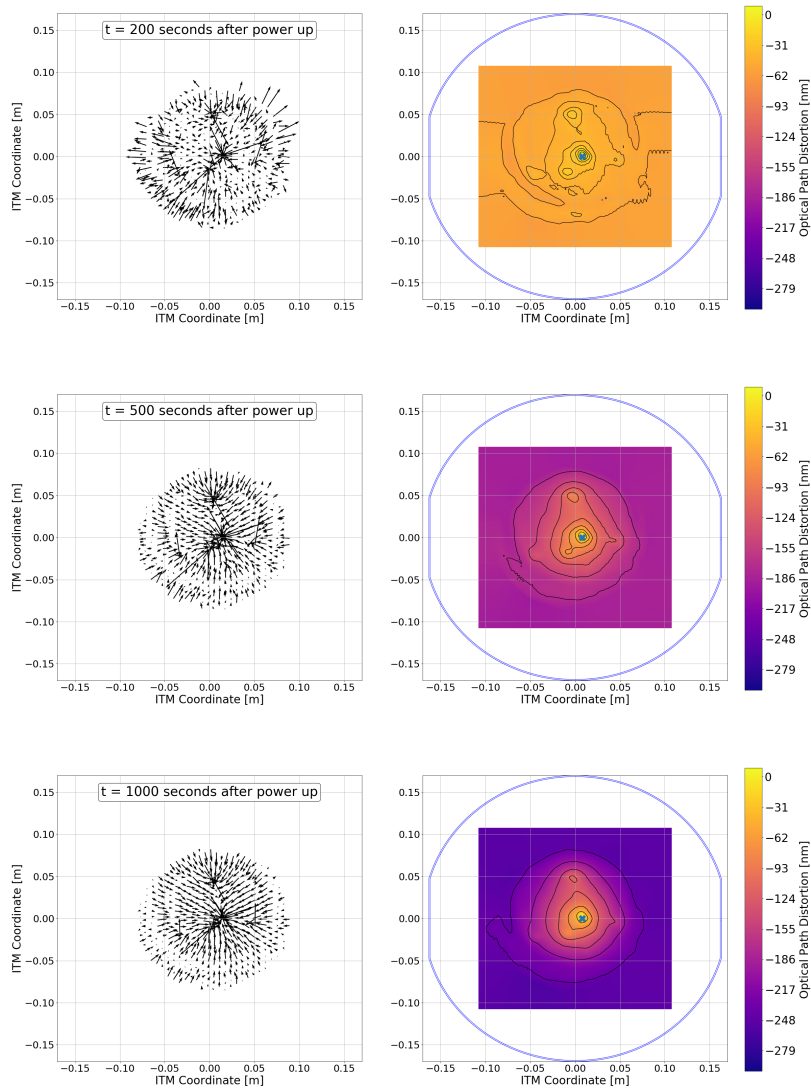


**Figure 6.10: ITMY gradient plots (left) and wavefront maps (right) during a power up to 30 Watts of input power.** Compared to the ITMX phase map in Figure 6.9, ITMY has a much larger overall heating pattern and higher spatial frequencies in the contours which was the first clue that revealed multiple (possibly 4) point absorber on the test mass. There is also a halo of gradients on the outer rim of the plots which is most prominent on the lower left corner. This is due reducing the CO<sub>2</sub> laser power in an attempt to compensate the lensing effects as the interferometer beam heats up the test mass. The overall scale of self-heating with the higher spatial frequencies of the point absorbers makes it incredibly difficult to compensate with using the CO<sub>2</sub> lasers as designed by Advanced LIGO.

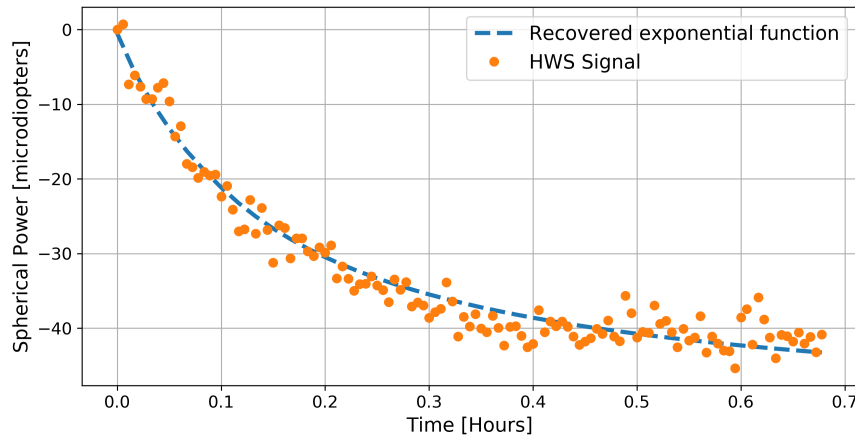
between the O2 and O3 observing runs was the replacement of ITMX, ETMX, and ETMY test masses. With a fully running Hartmann Sensor system in place which monitors the wavefront curvature across the optic, long-term trends over the observation runs will be able to determine how absorption changes as a function of time and whether test masses have an innate lifetime. This will be particularly important if the next generation of detectors use much higher power levels in order to achieve better high frequency sensitivity [18]. Using this method, the current absorption estimates for the H1 input test masses are as follows:

$$\begin{aligned} A_{\text{ITMX}} &= 328 \pm 84 \text{ ppb} \\ A_{\text{ITMY}} &= 688 \pm 85 \text{ ppb} \end{aligned} \tag{6.32}$$

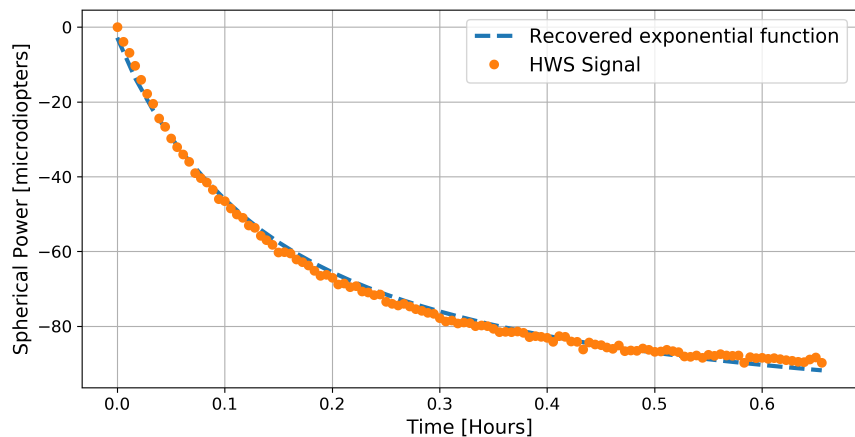
#### 6.4.2 Ring Heater and CO2 Commissioning

To counteract the effects of interferometer heating, Advanced LIGO uses a ring heater [73] [86] which has two heating elements mounted on the suspension cage. Each of them are glass formers wrapped by nichrome wire that has current running through it and radiates an annular heating pattern. The ring heaters will have two effects, it will induce a substrate lens and a radius of curvature change. As shown in Section 6.1, the carrier beam will not see the substrate lens but the radius of curvature difference will change the overall modal shape of the cavity. Similar to the distortion derived in section 6.2 where the thermo-refractive effect dominates when dealing with a Gaussian beam, the same is true from the ring heaters. Using equation D.6, one can directly calculate the power overlap between a pre-loaded cavity and the original, as it turns out, the effect varies the overlap by less than 0.1%

After using the Hartmann sensors to determine the absorption and pre-loading the ring heaters to compensate the interferometer lensing, the substrate is no longer in the nominal configuration during lock acquisition. Therefore, it is necessary to use CO2 (Carbon Dioxide) lasers to mimic the interferometer's heating on the compensation plate. The CO2 lasers



(a) ITMX absorption



(b) ITMY absorption

**Figure 6.11: Thermal lensing as seen by the ITM Hartmann Sensors after a lock loss.** A finite element simulation from COMSOL shows an impulse response which resembles an exponential decay can be linearized and fitted to the spherical power. The model assumes a beam size of 54 mm and 1 Watt of uniformly absorbed power then uses MCMC to fit the offset and scale to the data. Comparing ITMX and ITMY at Hanford shows a huge overall difference between the two optics, mostly due to the fact that ITMY has multiple point absorbers adding to the absorption estimate. In addition, fitting ITMY data points with the model does not seem to agree very well which indicates extra physics that stems from non-uniform heating by a 54 mm beam.

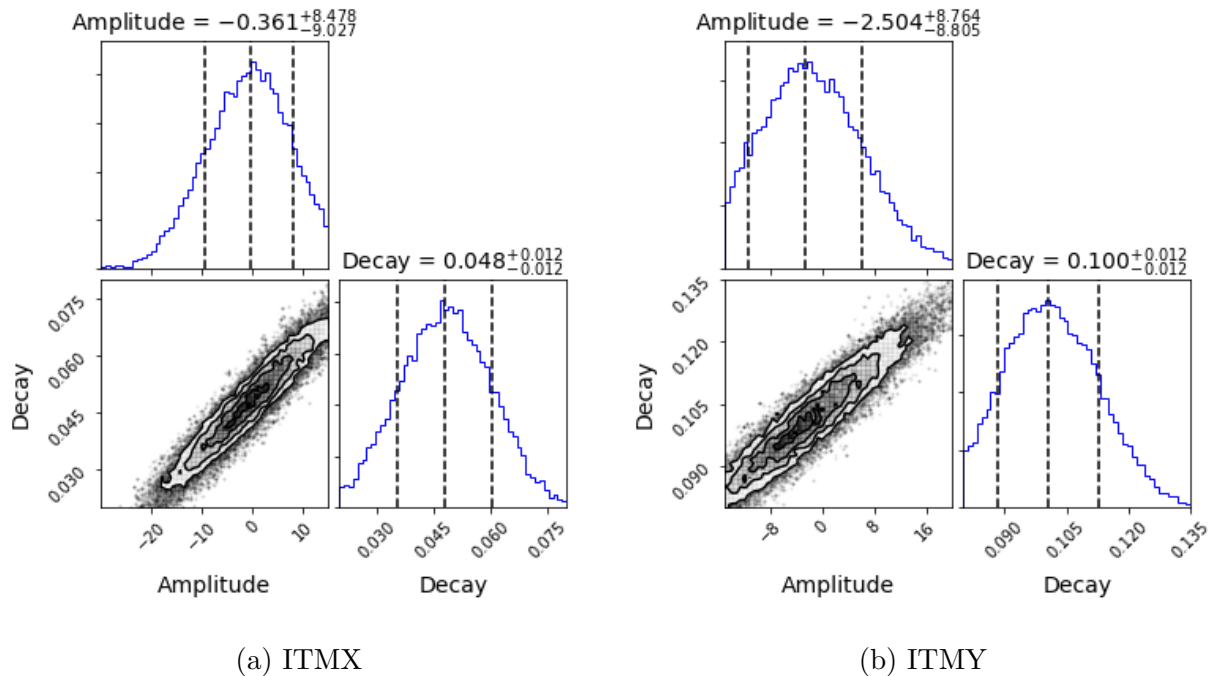


Figure 6.12: Posterior distributions from fitting the Hartmann sensor spherical power. Using the MCMC Hammer [42]

are located on each input test mass chamber and injected through a double zinc selenide viewport, then two steering mirrors direct the heating beam on the compensation plate of the reaction mass. In initial LIGO, the CO<sub>2</sub> beams were injected onto the high reflectivity surfaces of the test masses which created both a radius of curvature on the cavity side and a thermo-refractive change in the substrate. However, in advanced LIGO, the CO<sub>2</sub> lasers will only affect the substrate lensing. Tuning the CO<sub>2</sub> power will have a dramatic effect on the interferometer auxiliary degrees of freedom because the sidebands get rejected by the arm cavity and only resonate in the recycling cavities.

The self-heating caused by the interferometer beam is assumed to have a Gaussian intensity profile, while the CO<sub>2</sub> heating beam is meant to have a uniform heating profile across the test mass surface which allows for a consistent phase distortion as a beam passes through the substrate.

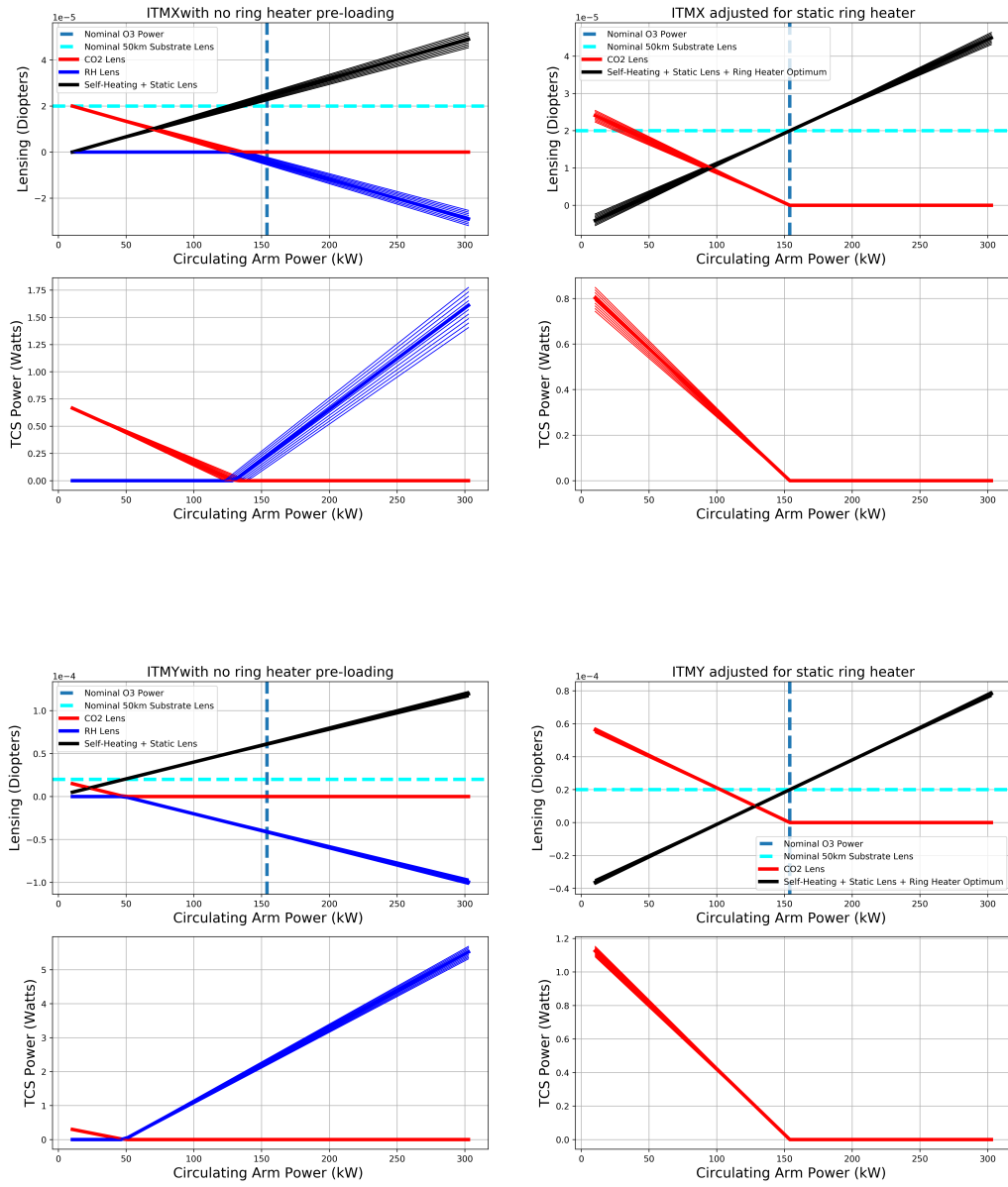


Figure 6.13: **Calculated TCS settings to balance the substrate lens.** The nominal circulating power denoted by the vertical blue line is a function of the input power, the recycling gain, and the arm cavity gain. The nominal input power for O3 will be 50 Watts and the power recycling gain is around 45. The arm cavity gain can be estimated by calibrating the transmitted power from each of the arms and is approximately 228. The horizontal, dashed turquoise line represents the nominal substrate lens with a focal length of 50 km. This value is what the power recycling cavity expects to properly mode match to the arms.

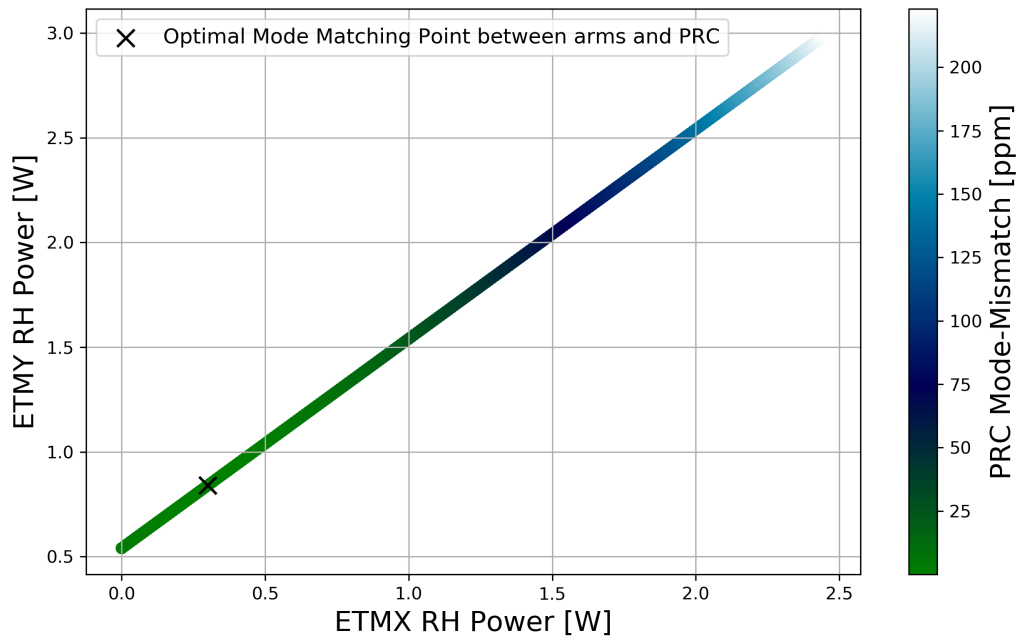


Figure 6.14: **Mode matching the arm cavities to the power recycling cavity.** Determining the ITM ring heaters and CO<sub>2</sub> power levels still leaves the end test mass ring heaters to be set. The goal is to maintain the mode matching between the arms while simultaneously searching for the optimal overlap with the power recycling cavity. This is done by determining the spatial mode overlap between all three cavities (2 ARMS) The linear portion of the graph shows a combination of common and differential adjustment of each ring heater that keeps the mode matching between the arms at less than 1 PPM

	Substrate	HR surface	Compensation Plate
Self Heating	*4.9e-4	*-3.6e-5	N/A
Ring Heater	-9.0e-6	*9.9e-7	N/A
CO2x	N/A	N/A	1.5e-5
CO2y	N/A	N/A	2.5e-5

Table 6.1: **Single pass actuator lensing calibrations for aLIGO TCS in micro-diopters/Watt.** The asterisks indicate the values are extracted from a model and the measured values use the Hartmann sensors which cannot distinguish between surface and substrate lensing, however, the latter is larger by an order of magnitude. CO2x and CO2y were measured to be different in their actuation strength which could stem from either misalignment or a misplaced central mask. The uncertainty is expressed by the last digit available.

## 6.5 Point Absorbers

Up till to point, all actuators models, and measurements assumed uniform absorption across the optics which results in second order Hermite-Gauss coupling with the fundamental Gaussian beam . As it turns out, this assumption is not so simple. One of the main successes for the Hartmann Wavefront Sensors have been the ability to find excess absorption due to point absorbers on the high reflectivity surfaces of the test masses. During the second observation run (O2), there was an absorber found on ITMX that made increasing the input power past 30 watts extremely difficult and futile because it was thought to couple intensity noise into DARM. The exact origin of these point absorbers is still an active area of research but incursions into the vacuum system will always pose a risk of spreading particulate on the HR surfaces.

*Part way into commissioning for O3, another point absorber on ITMY was detected that showed similar characteristics.* Since their spatial frequencies are much higher than the uniform absorption, many of the models for scattered power and thermal effects require significant adjustment to predict the interferometer behavior. To decompose the differential phase map into the Hermite Gauss basis requires a relatively high order and makes full interferometer simulations very difficult. For example, FINESSE

calculations on a laptop tend to become unwieldy at around  $n + m \leq 6$ . This affects the HWS's ability to properly evaluate total thermal lens from the interferometer, therefore changing the estimated absorption. There are two main parts which allow point absorbers to adversely affect interferometer performance. The first is scattering from the arm cavity that takes away carrier light and couples to higher order modes, and secondly, the thermal lens in the substrate distorts the power recycling cavity for the sideband build ups dramatically.

A few ways to try getting around this could be separating the temporal effects which quadratically depend on the point absorber size. The thermo-refractive transient solution found in Vinet [85] has the form

$$Z_{\text{TR}}(t) \propto 1 - \exp\{-t/\tau\} \quad (6.33)$$

where  $\tau = \frac{\rho C w_{\text{pa}}^2}{3\kappa}$  is the characteristic time constant that depends on the beam size  $w_{\text{pa}}$ , the thermal conductivity  $\kappa$ , the specific heat  $C$  and the material density  $\rho$ . A simple model can consist of two beams with different sizes which will have separate time constants. Another interesting way of characterizing what can be compensated for O3 could be to Fourier transform the optical path distortion and low pass the high spatial frequency components with a Gaussian filter. The cut-off frequency can be estimated by the approximate point absorber size (10-20 mm). Of course, early detection and replacement of an optic may be the most efficient way to avoid custom thermal compensation. Figure 6.15 shows a comparison between ITMX and ITMY while the interferometer is increasing input laser power from 2 to 30 Watts. Within the first few hundred seconds, the point absorbers begin showing up in the optical path distortion map.

During commissioning periods, the highest starting priority is to achieve full resonance as quickly as possible and is easier with approximately 2 Watts of input laser power. This requires locking the arm length stabilization (ALS) system with 532 nm, the vertex degrees of freedom (DRMI) and complete the common arm length (CARM) transition. Additionally,

closing all angular degrees of freedom (ASC) will take a lot of time and energy. If major upgrades or fixes have occurred such as replacing main test masses then all the prior steps require many months of commissioning. Generally, vacuum incursions into the main vertex cost the most time and money because of the large volume needing to be pumped. All this is to say, the earlier point absorbers are detected, the better. However, this requires a high level of arm power which historically has come much later on the road to nominal low noise. In Figure 6.5, the signal-to-noise ratio is 10 at 0.01 Hz for 37.5 mW of absorbed power which means the circulating arm power must reach at least 75 kW (assuming absorption is approximately 0.5 ppm) to be detectable within the time constant of point absorbers. This could still be achieved without full lock if the first priority after pumping down is resonating a single arm with power recycling at the highest input laser power possible (currently 70 Watts). With a single power recycled arm cavity the expected circulating power absorbed on the HR surface of the test masses is

$$\begin{aligned} P_{\text{PRC-1ARM}} &= P_{\text{in}} * g_{\text{PRC}} * g_{\text{ARM}} * 0.25 * \epsilon_a \\ &\approx 98 \text{ mW} \left[ \frac{P_{\text{in}}}{70 \text{ Watts}} \right] \left[ \frac{g_{\text{PRC}}}{45} \right] \left[ \frac{g_{\text{ARM}}}{225} \right] \left[ \frac{\epsilon_a}{0.5 \text{ ppm}} \right] \end{aligned} \quad (6.34)$$

where the factor of 0.25 comes from double passing the main beamsplitter, the coefficient  $\epsilon_a$  is the estimated uniform absorption. Using  $D_{\text{sub}} \approx 487 \frac{\mu\text{D}}{1 \text{ Watt}}$  as the modeled conversion from absorbed power to steady-state spherical power. The expected substrate lensing in units of micro-diopters [ $\mu\text{D}$ ] is

$$S_{\text{PRC-1ARM}} = P_{\text{PRC-1ARM}} * D_{\text{sub}} \approx 48 \mu\text{D} \quad (6.35)$$

which readily detectable by the current Hartmann sensors. Commissioning and installation schedules are ever-changing entities and there have been times when the end stations are not ready for integration simultaneously. This provides a window where only single arm commissioning is available so this method might be able to detect the existence of point

absorbers much sooner.

The question still remains, once these anomalies are found, what can be done?

One consideration is a complete re-design of Thermal Compensation to account for higher frequency spatial corrections. There are already custom masks at Hanford which are designed to smooth the optical path distortion in the substrate and can be implemented with the CO<sub>2</sub> lasers on the compensation plate to increase the sideband build ups, which is one of the biggest difficulties associated with point absorbers. However, this does not solve the fundamental problem of losing power recycling gain due to power scattering where the quadratic losses of the arm cavity set an upper limit for increasing power. Another way to avoid these effects is to move the beam spot away from the point absorber on the HR surface but it must be sufficiently far or the odd higher order modes will couple very strongly with asymmetry.

## 6.6 Higher Power Operation

The goal for O3 is 150 kW of circulating power in the arms.

With the sensors and tests described in the preceding sections, a cohesive plan to pre-load the interferometer was implemented in order to achieve stable higher power operation in the detectors. Generally, the Thermal Compensation System has two goals: Firstly, the actuators are used to pre-load the test masses with heat in anticipation of the lensing due to the interferometer while operating at full lock and higher power. Secondly, the amount of mode-matching between the coupled cavities must be optimized in order to achieve the best sensitivity. Using the absorptions measured in Figure 6.11, it is possible to estimate the total amount of lensing from self-heating as a function of input power.

In principle, the Hartmann measurements of absorbed power provide sufficient information to pre-loaded the interferometer in anticipation of 50 Watts of input power. At Hanford, this proved to be very difficult for reliably locking the interferometer, so with the combi-

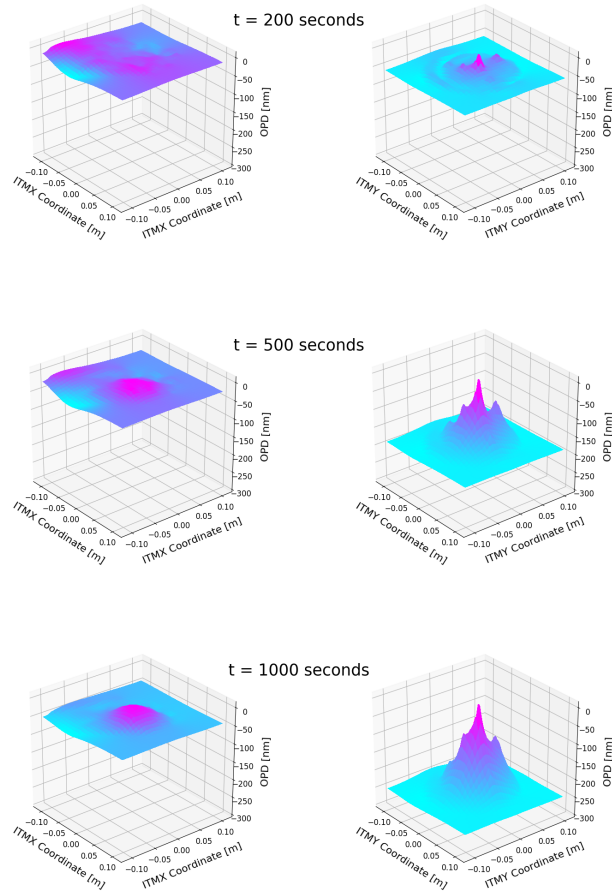


**Figure 6.15: Comparing 3-D plots of the optical path distortion for ITMX and ITMY test masses after powering up the interferometer.** The horizontal axes represent the test mass coordinates as seen on the Hartmann sensors and the vertical axis is the optical path distortion in units of nanometers. The color map is scaled for each plot and is meant to show particularly hot areas and roughly compare the high frequency spatial distribution of point absorbers. Plots in the left column (ITMX) have smooth spatial features that stem from uniform absorption and the effects are not prominent till after approximately 500 seconds. In contrast, plots in the right column (ITMY) have very sharp spatial features which already rise above the floor at 200 seconds into powering up. Comparing the overall surface deformation on the same scale, the difference between ITMX and ITMY is striking and it is clear how an interferometer with point absorbers on the surface will struggle to increase powers above 200 kW within the arm cavities.

nation of estimates provided by the Hartmann Sensors and experimentation with the CO2 power levels at each stage of increasing the PSL power, we are able to consistently lock at 30 Watts of PSL input power and  $\approx 140\text{ kW}$  of circulating arm power. The biggest difficulty associated with implementing this thermal compensation scheme was consistently locking DRMI in high micro-seismic conditions. This could be contributed to misalignment of CO2 lasers to the test masses, which were aligned using the Hartmann sensors and doubly-checked by cycling the lasers on/off to measure the single bounce interferometer beam deflection at the anti-symmetric port.

This required considerable tuning of the thermal compensation system that is not needed at Livingston for the same input power. Although both interferometers saw a decay in power recycling which was found to be attributed to a point absorber on L1-ETMX.

During the early phases of commissioning higher power at Hanford, most of the locklosses occurred when the 9 Mhz sidebands would fall below a certain threshold level.

## 6.7 Mode Matching IFO to OMC: Single Bounce

Using the OMC as an optical spectrum analyzer is one simplest methods for understanding the mode matching coming out of the interferometer. In the single bounce configuration, measuring the ratio between the second order mode and the fundamental gives a first look at the limit of matching. The same can be done using the squeezed beam as well and during commissioning of the squeezer, a mode-mismatch of 20% was observed which led to a re-design of the optical path entering the interferometer.

### 6.7.1 SR3 Heater

- Beckhoff code

### 6.7.2 SRM Heater

- Mode Profiling: Single Bounce
  - OMC Scanning

## 6.8 Mode Matching Squeezer to OMC

- Mode Profiling
  - OMC Scanning
- Astigmatism: expected in LIGO and measured!

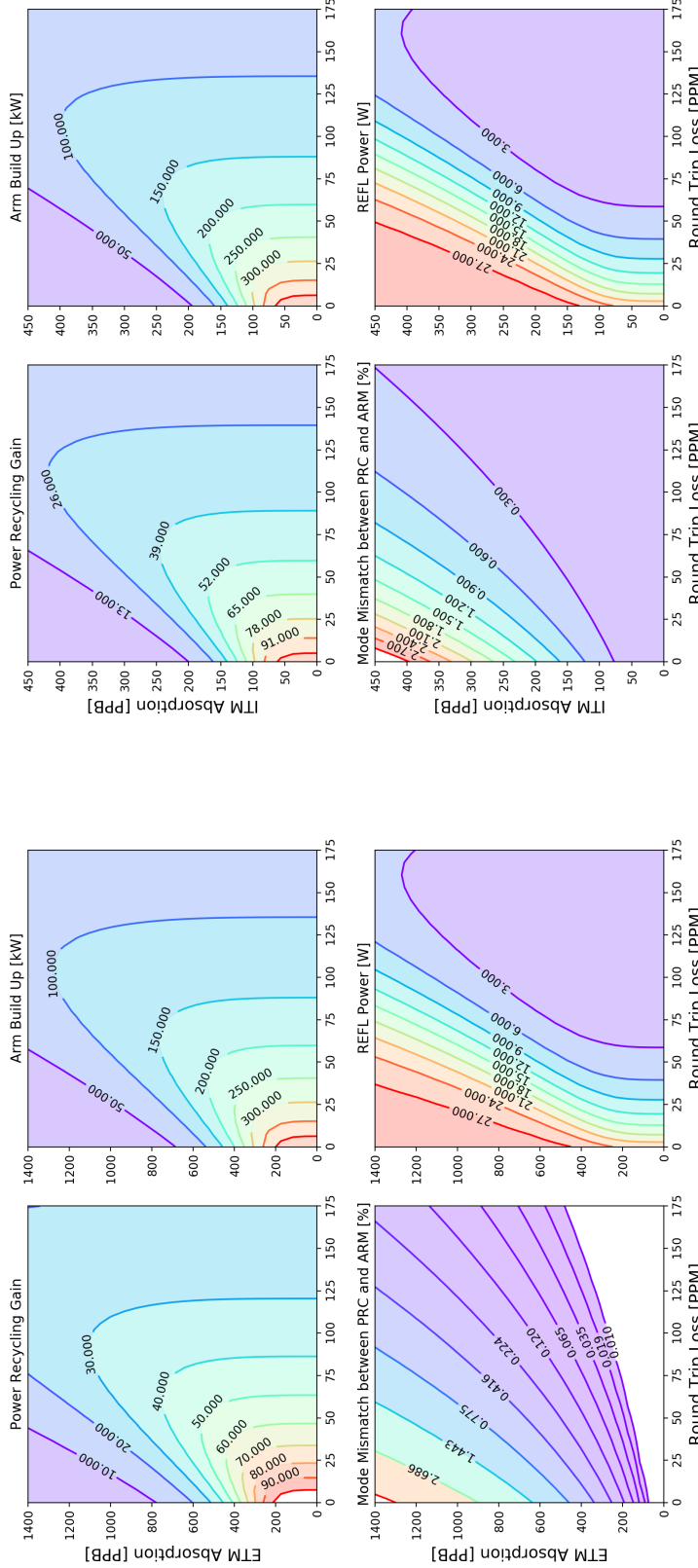


Figure 6.16: **Interferometer DC powers as a function of round trip arm loss and test mass absorption.** Simplifying the power recycling cavity and a combined arm model to understand the powers as a function of loss has a few advantages with regards to computational time and the results are easier to conceptually understand. Here, absorption changes the radius of curvature and substrate thermal lens which results in some mode mismatch while the round trip loss takes into account the rest of the higher order modes from point absorbers. The ITM absorption has a much larger effect on the overall power recycling gain loss by almost a factor of 3 compared to ETM absorption. Of course, the simplified model will fall short in describing effects on the antisymmetric signals of the full interferometer.

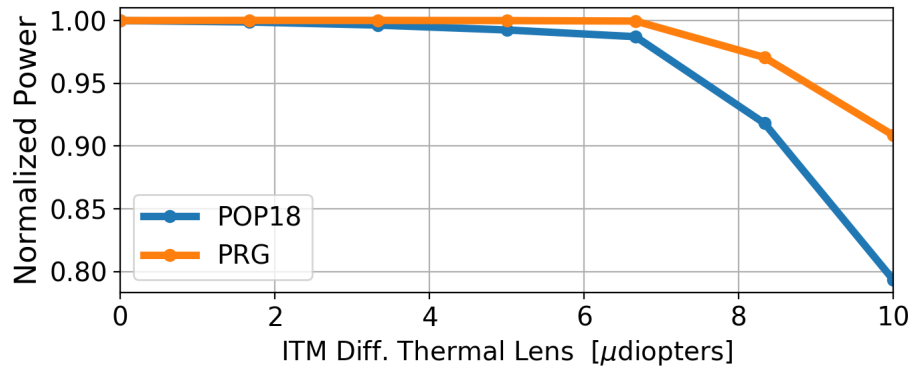


Figure 6.17: **Model of POP-18 as a function of differential thermal lensing using FINESSE.** The horizontal axis is differential lensing between the ITMX/ITMY substrates and the vertical axis represents the normalized power when locked with nominal mode matching. POP-18 is the signal at the power recycling pick-off port demodulated at 18 MHz which shows the sideband power buildup in the power recycling cavity. In this particular simulation the differential lensing requires finding a new operational point to lock the longitudinal degrees of freedom. Additionally, the sensors which are used to maintain resonance and readout the RF power need to be re-phased in order to get the upper limit estimate. Even with modest differential lensing (10 micro diopters), the buildup drops by 20 percent and eventually the simulation has trouble maintaining resonance similarly to the actual interferometer.

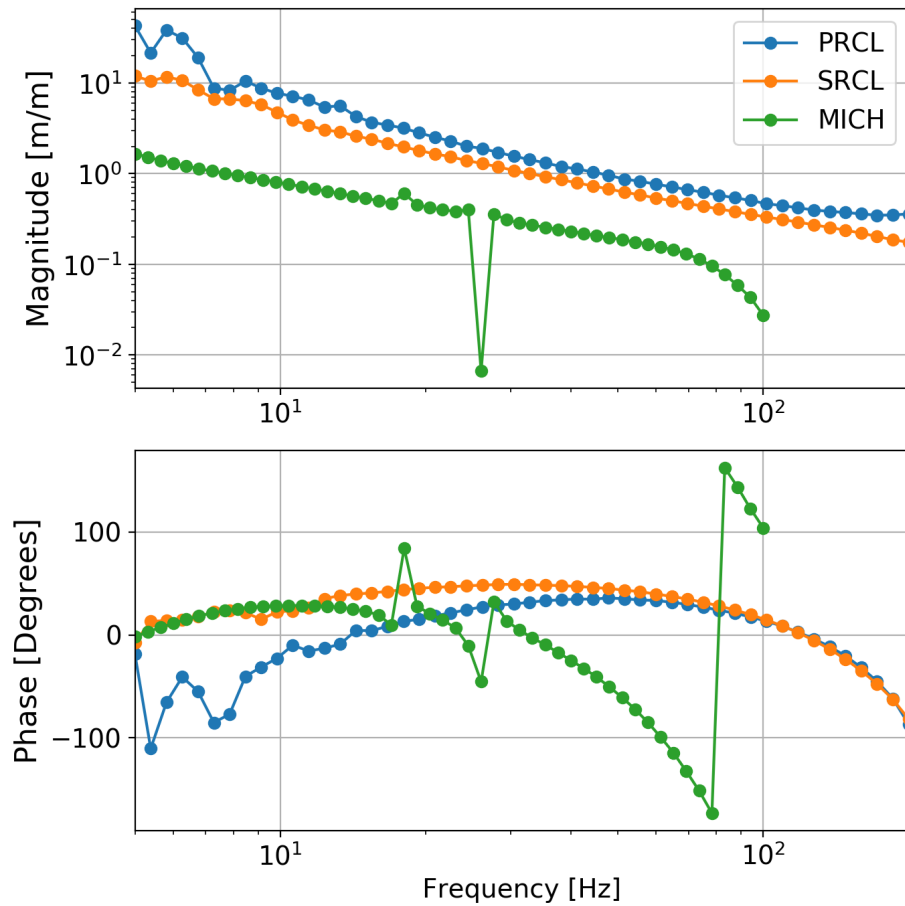


Figure 6.18: **Vertex open loop transfer functions while in Nominal Low Noise.** The nominal UGF for PRCL is around 45 Hz.

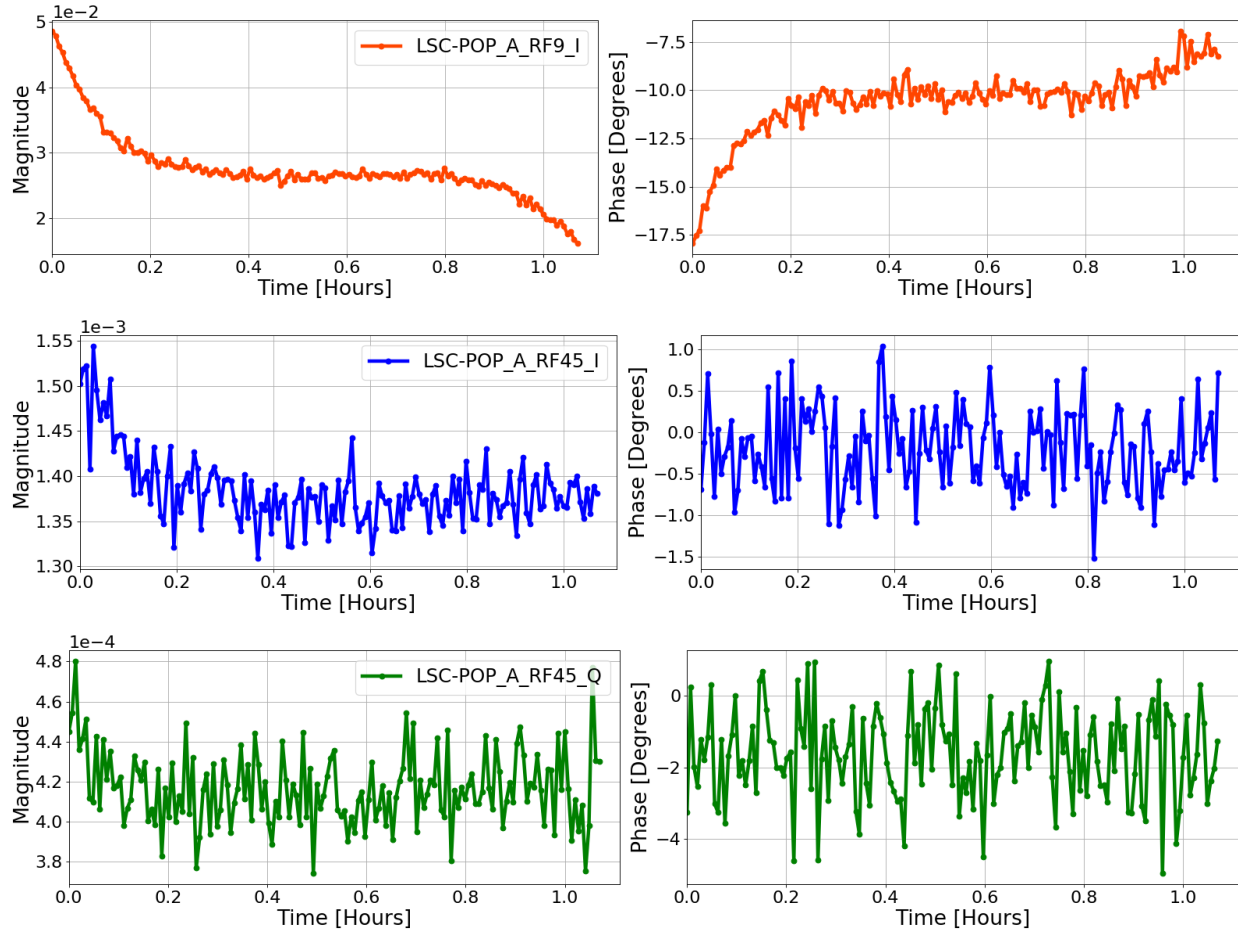


Figure 6.19: **Measuring vertex optical gains as a function of heating.** Injecting a dither line into each degree of freedom and digitally demodulating the respective sensors at the excitation frequency can provide insight on how much the optical gain/phase shifts as a function of heating. At time  $t=0$ , the power begins increasing from 2 watts of input power to 20 watts. In PRCL, there is a reduction to 80% of the starting magnitude and 7.5 degrees of phase rotation with the first power increase. At 0.9 hours, the input power goes from 20 to 30 watts and the magnitude drops to about 30% of the original gain which results in a lock loss. As for the SRCL and MICH degrees of freedom, there are slight changes first power increase but not nearly as bad as PRCL.

# Chapter 7

## Solutions for Detector Upgrades

A solution to the current mode matching situation will be solved by further expanding active wavefront control described in Section [17]. A full modal picture, sensors and actuator

### 7.1 Sensors

\* Bullseye photodetectors

\* Operation: range (in terms of watts and percentage mismatch)

### 7.2 High Sensitivity Telescope

\* Translation stages: General principles, rigging, sensitivity

\* Mechanical description (Solidworks designs)

\* Constraints (range, vacuum, alignment, integration)

\* Electronics

\* Software

\*Implementation: rigg something better, in situ measurements.

## 7.3 A Global Active Wavefront Control Scheme

To truly implement a system that solves the mode matching challenges presented in LIGO, an active control scheme that implements both sensors and actuators will be required to span the degrees of freedom that are present in the interferometer.

### 7.3.1 Hard and Soft Mode Matching

Similar to the wavefront sensors already being used in LIGO at the time of this writing, the active wavefront system should be able to rotate the phase of their actuators and sensors to the common and differential basis. Also, the extra two degrees of freedom required are the hard and soft modes for thermal lensing which curve the ITMs and ETMs in a way which vary the waist size and position orthogonally.

# Appendices

# Appendix A

## Resonator Formulas

Equation 2.23 describes the stability condition for a two mirror Fabry-Perot cavity, but is worthwhile to derive the criterion for geometric stability from the ray matrix tools commonly used in optics. The alignment of two plane waves traveling in space can differ by two quantities: the axial and angular separations,  $y$  and  $\theta$ , respectively. These two quantities can be transformed via these optical matrices:

Lens:

$$\hat{F}_i = \begin{pmatrix} 1 & 0 \\ -\frac{1}{f_i} & 1 \end{pmatrix} \quad (\text{A.1})$$

Curved Mirror:

$$\hat{M}_i = \begin{pmatrix} 1 & 0 \\ \frac{2}{R_i} & 1 \end{pmatrix} \quad (\text{A.2})$$

Space:

$$\hat{D}_i = \begin{pmatrix} 1 & d_i \\ 0 & 1 \end{pmatrix} \quad (\text{A.3})$$

Using these matrices, the periodic Fabry-Perot with two mirrors can be represented by the

matrix,

$$\begin{pmatrix} y_{m+1} \\ \theta m + 1 \end{pmatrix} = \hat{M}_{FP} \begin{pmatrix} y_m \\ \theta m \end{pmatrix} \quad (\text{A.4})$$

where

$$\hat{M}_{FP} = \hat{M}_i \hat{D}_i \hat{M}_i \hat{D}_i \quad (\text{A.5})$$

is the optical transfer matrix. The goal is to find a geometric condition that is dependent on the optical transfer matrix which keeps the axial displacement from diverging.

$$\begin{pmatrix} y_{m+1} \\ \theta m + 1 \end{pmatrix} = \begin{pmatrix} A & B \\ C & D \end{pmatrix} \begin{pmatrix} y_m \\ \theta m \end{pmatrix} \quad (\text{A.6})$$

which means

$$\theta_m = \frac{y_{m+1} - A y_m}{B} \quad (\text{A.7a})$$

$$\theta_{m+1} = \frac{y_{m+2} - A y_{m+1}}{B} \quad (\text{A.7b})$$

Solving for  $y_{m+2}$

$$y_{m+2} = (A + D) y_{m+1} - \det(\hat{M}_{FP}) y_m \quad (\text{A.8})$$

Assuming a geometrical solution where  $y_m = y_o h^m$  and plugging into the equation above,

$$h^2 = (A + D) h - \det(\hat{M}_{FP}) \quad (\text{A.9})$$

which is a quadratic equation that has two solutions and can be further simplified if the index of refraction for the entire system remains constant such that  $\det(\hat{M}_{FP}) = 1$ . Plugging back into  $y_m$  and doing some algebra

$$y_m \propto \sin(m\phi) \quad (\text{A.10})$$

where  $\phi = \cos^{-1}(\frac{A+D}{2})$ , which is also referred to as the round trip Gouy phase of the cavity.

In order for  $y_m$  to be harmonic instead of hyperbolic and hence confined, this condition must be met

$$\frac{|A + D|}{2} \leq 1 \quad (\text{A.11})$$

By actually calculating the terms of  $\hat{M}_{FP}$  and doing even more algebra, it is clear that

$$0 \leq \left(1 - \frac{L}{R_1}\right) \left(1 - \frac{L}{R_2}\right) \leq 1 \quad (\text{A.12})$$

which is what was stated in equation 2.23. There is a simpler and less algebraic way to reach the same conclusion by looking at the Rayleigh range of a finite Gaussian beam for a simple cavity. In Table II of Kogelnik and Li [59], there is an expression for the Rayleigh range

$$\begin{aligned} z_R^2 &= \frac{L(R_1 - L)(R_2 - L)(R_1 + R_2 - L)}{(R_1 + R_2 - 2L)^2} \\ &= \frac{g_1 g_2 (1 - g_1 g_2)}{(g_1 - g_2 - 2g_1 g_2)^2} \end{aligned} \quad (\text{A.13})$$

If the Rayleigh range is a real number, then once again, equation 2.23 must be true.

## Appendix B

### Hermite Gauss Normalization

According to equation 3.12, the higher order modes in the Hermite Gauss basis has the intensity profile,

$$I_{mn}(x, y, z) = |A_{mn}|^2 \left[ \frac{W_0}{W(z)} \right]^2 \mathbb{G}_n^2 \left( \frac{\sqrt{2}x}{W(z)} \right) \mathbb{G}_n^2 \left( \frac{\sqrt{2}y}{W(z)} \right) \quad (\text{B.1})$$

It is useful to normalize the first few lowest order modes with respect to the total optical power since the Gaussian beam will couple to them the most due either misalignment or mode mismatch as seen in section []. In one dimension, the total optical power for the first 3 modes are

$$\begin{aligned} P_0(x, y, z) &= \int_{-\infty}^{\infty} |A_0|^2 \left[ \frac{W_0}{W(z)} \right] e^{-2x^2/w^2(z)} dx \\ P_1(x, y, z) &= \int_{-\infty}^{\infty} |A_1|^2 \left[ \frac{W_0}{W(z)} \right] \frac{8x^2}{w^2(z)} e^{-2x^2/w^2(z)} dx \\ P_2(x, y, z) &= \int_{-\infty}^{\infty} |A_2|^2 \left[ \frac{W_0}{W(z)} \right] \left( \frac{8x^2}{w^2(z)} - 2 \right)^2 e^{-2x^2/w^2(z)} dx \end{aligned} \quad (\text{B.2})$$

In two dimensions, the total optical power for the first 3 modes are

$$\begin{aligned} P_{00}(x, y, z) &= \int_{-\infty}^{\infty} \int_{-\infty}^{\infty} |A_{00}|^2 \left[ \frac{W_0}{W(z)} \right]^2 e^{-2x^2/w^2(z)} e^{-2y^2/w^2(z)} dx dy \\ P_{10}(x, y, z) &= \int_{-\infty}^{\infty} \int_{-\infty}^{\infty} |A_{10}|^2 \left[ \frac{W_0}{W(z)} \right]^2 \frac{8x}{w^2(z)} e^{-2x^2/w^2(z)} e^{-2y^2/w^2(z)} dx dy \\ P_{20}(x, y, z) &= \int_{-\infty}^{\infty} \int_{-\infty}^{\infty} |A_{20}|^2 \left[ \frac{W_0}{W(z)} \right]^2 \left( \frac{8x^2}{w^2(z)} - 2 \right)^2 e^{-2x^2/w^2(z)} e^{-2y^2/w^2(z)} dx dy \end{aligned} \quad (\text{B.3})$$

By setting the equations above to unity, the normalization factors become

$$\begin{aligned} A_0 &= \left( \frac{2}{\pi w_0^2} \right)^{1/4} \\ A_1 &= \left( \frac{2}{\pi w_0^2} \right)^{1/4} \frac{1}{\sqrt{2}} \\ A_2 &= \left( \frac{2}{\pi w_0^2} \right)^{1/4} \frac{1}{\sqrt{8}} \end{aligned} \quad (\text{B.4})$$

$$\begin{aligned} A_{00} &= \sqrt{\frac{2}{\pi w_0^2}} \\ A_{10} &= \sqrt{\frac{1}{\pi w_0^2}} \\ A_{20} &= \sqrt{\frac{1}{4\pi w_0^2}} \end{aligned} \quad (\text{B.5})$$

# Appendix C

## Bullseye and Quadrant Photodiode Characterization

Both RF and DC segmented photodiodes are widely used in LIGO’s sensing schemes, however, the quadrant photodiodes (QPDs) are more readily implemented. Recently, a bullseye photodiode has been installed upstream of the pre-mode cleaner to sense the size and angular jitter noise contribution from the high powered oscillator. It is useful to have angular sensors both upstream and downstream of optical cavities to narrow down where jitter could be coupling into the optical path. That being said, to calibrate the two types of sensors in common units, it is easiest to scale by beam diameters.

### C.1 Quadrant Photodiodes (QPD)

Calculating the QPD response to angular jitter is relatively straight forward. Beginning with a Gaussian beam in rectangular coordinates that is displaced along the horizontal axis by a

small value  $\Delta x$  and expanding to first order:

$$\begin{aligned} I(x, y) &= \left( \frac{2}{\pi w^2} \right) e^{-2 \frac{(x+\Delta x)^2 + y^2}{w^2}} \\ &\approx \left( \frac{2}{\pi w^2} \right) e^{-2 \frac{x^2 + y^2}{w^2}} \left( 1 - \frac{4x\Delta x}{w^2} \right) \end{aligned} \quad (\text{C.1})$$

Converting to polar coordinates where  $x = r \cos \theta$  and  $y = r \sin \theta$  then integrating over the individual segments to get the power,

$$\begin{aligned} P &= \left( \frac{2}{\pi w^2} \right) \int_0^\infty \int_{\theta_1}^{\theta_2} e^{-2 \frac{r^2}{\omega^2}} \left( 1 - \frac{4r \cos \theta}{w^2} \Delta x \right) r dr d\theta \\ &= \frac{1}{2} - [\cos \theta_2 - \cos \theta_1] \frac{8\Delta x}{\pi \omega^4} \int_0^\infty e^{-2 \frac{r^2}{\omega^2}} r^2 dr \\ &= \frac{1}{2} - [\cos \theta_2 - \cos \theta_1] \frac{\Delta x}{2\pi \omega^2} \left( \sqrt{2\pi} \omega \operatorname{erf}\left(\frac{\sqrt{2}r}{\omega}\right) - 4r e^{-2 \frac{r^2}{\omega^2}} \right) \Big|_0^\infty \\ &= \frac{1}{2} - [\cos \theta_2 - \cos \theta_1] \frac{\Delta x}{w} \sqrt{\frac{1}{2\pi}} \end{aligned} \quad (\text{C.2})$$

where  $\theta_1$  and  $\theta_2$  are the limits from  $\pm\pi/2$  for the right half and  $\mp\pi/2$  for the left half. Denoting the right and left segment as  $P_2$  and  $P_1$ , respectively, it is possible to subtract the halves and obtain a calibrated DC signal in units of beam diameter.

$$S = P_2 - P_1 = 2 \sqrt{\frac{2}{\pi}} \frac{\Delta x}{\omega} \quad (\text{C.3})$$

It is trivial to repeat the calculation for vertical displacements so it is left for the reader to complete.

## C.2 Bullseye Photodiodes

Similar to the QPD calibration above, it is possible to express pitch and yaw displacements that are normalized to beam diameters. Additionally, the bullseye's geometry will give insight on the beam size jitter. A sensing matrix for these degrees of freedom is realized in

	Seg 1	Seg 2	Seg 3	Seg 4
Pit	1	1	-2	0
Yaw	-1	1	0	0
Wid	1	1	1	-1
Sum	1	1	1	1

Table C.1: Bullseye photodiode sensing matrix.

Table ??.

### C.2.1 Width

The bullseye's calibration is determined in a similar manner to the QPD however, the sensitivity will inherently depend on the beam size. To calculate what beam size is optimal, first consider a power integral for a cylindrically symmetric Gaussian beam,

$$\begin{aligned} \text{Power} &= \int_A^B |A_{00}|^2 e^{\frac{-2r^2}{\omega^2}} 2\pi r dr \\ &= -|A_{00}|^2 \frac{\pi\omega^2}{2} e^{\frac{-2r^2}{\omega^2}} \Big|_A^B \end{aligned} \quad (\text{C.4})$$

Plugging in limits for the equation where  $R$  is the boundary between the inner and outer segments,

$$P_{\text{in}} = \text{Power} \Big|_0^R = |A_{00}|^2 \frac{\pi\omega^2}{2} [1 - e^{\frac{-2R^2}{\omega^2}}] \quad (\text{C.5})$$

$$P_{\text{out}} = \text{Power} \Big|_R^\infty = |A_{00}|^2 \frac{\pi\omega^2}{2} [e^{\frac{-2R^2}{\omega^2}}] \quad (\text{C.6})$$

The error signal comes from subtracting the inner segment from the outer,

$$S_{\text{WID}} = P_{\text{in}} - P_{\text{out}} \quad (\text{C.7})$$

Minimizing the derivative with respect to the beam size will determine the optimal width which gives the best sensitivity to beam size change,

$$\begin{aligned}\frac{\partial S_{\text{WID}}}{\partial \omega} &\approx \frac{8R^2}{\omega^2} \left(1 - \frac{2R^2}{\omega^2}\right) = 0 \\ \Rightarrow \omega &= \sqrt{2}R\end{aligned}\quad (\text{C.8})$$

When determining the beam size, it is possible to measure the beam size directly by fitting the power ratio. For example, if the constraint that  $\omega = \sqrt{2}R$  then the power ratio is,

$$\text{DC Power Ratio} = \frac{P_{\text{out}}}{P_{\text{in}}} = \frac{e^{-2R^2/\omega_0^2}}{1 - e^{-2R^2/\omega_0^2}} \approx 0.582 \quad (\text{C.9})$$

### C.2.2 Pitch

To calibrate the pitch signal on a bullseye, first consider a Gaussian that is displaced in the vertical direction,

$$\begin{aligned}I^{\text{Pit}}(x, y) &= \left(\frac{2}{\pi w^2}\right) e^{-2\frac{x^2+(y+\Delta y)^2}{w^2}} \\ &\approx \left(\frac{2}{\pi w^2}\right) e^{-2\frac{x^2+y^2}{\omega^2}} \left(1 - \frac{4x\Delta y}{w^2}\right)\end{aligned}\quad (\text{C.10})$$

The integrated power for a given segment is,

$$\begin{aligned}P_{\theta_1 \rightarrow \theta_2}^{\text{Pit}} &= \left(\frac{2}{\pi w^2}\right) \int_R^\infty \int_{\theta_1}^{\theta_2} e^{-2\frac{r^2}{\omega^2}} \left(1 - \frac{4r \sin \theta}{w^2} \Delta y\right) r dr d\theta \\ &= \left(\frac{\theta_2 - \theta_1}{2\pi}\right) e^{-2\frac{R^2}{\omega^2}} + (\cos \theta_2 - \cos \theta_1) \frac{1}{\sqrt{2\pi}} \frac{\Delta y}{\omega} \left[\operatorname{erfc}\left(\frac{\sqrt{2}R}{\omega}\right) \sqrt{\frac{8}{\pi}} \frac{R}{\omega} e^{-2\frac{R^2}{\omega^2}}\right]\end{aligned}\quad (\text{C.11})$$

The error signal from a pitch displacement following Table ?? is,

$$S^{\text{Pit}} = P_{\text{seg1}}^{\text{Pit}} + P_{\text{seg2}}^{\text{Pit}} - 2P_{\text{seg3}}^{\text{Pit}} = 3\sqrt{\frac{3}{2\pi}} \frac{\Delta y}{\omega} \left[\operatorname{erfc}\left(\frac{\sqrt{2}R}{\omega}\right) + \sqrt{\frac{8}{\pi}} \frac{R}{\omega} e^{-2\frac{R^2}{\omega^2}}\right] \quad (\text{C.12})$$

### C.2.3 Yaw

Using C.1 and repeating the mathematics above, the power for an individual segment is

$$\begin{aligned} P_{\theta_1 \rightarrow \theta_2}^{\text{Yaw}} &= \left( \frac{2}{\pi w^2} \right) \int_R^\infty \int_{\theta_1}^{\theta_2} e^{-2\frac{r^2}{\omega^2}} \left( 1 - \frac{4r \cos \theta}{w^2} \Delta x \right) r dr d\theta \\ &= \left( \frac{\theta_2 - \theta_1}{2\pi} \right) e^{-2\frac{R^2}{\omega^2}} + (\cos \theta_2 - \cos \theta_1) \frac{1}{\sqrt{2\pi}} \frac{\Delta x}{\omega} \left[ \operatorname{erfc} \left( \frac{\sqrt{2}R}{\omega} \right) \sqrt{\frac{8}{\pi}} \frac{R}{\omega} e^{-2\frac{R^2}{\omega^2}} \right] \end{aligned} \quad (\text{C.13})$$

Plugging in the angles to get the signal response in terms of beam radius,

$$S^{\text{Yaw}} = P_{\text{seg1}}^{\text{Yaw}} - P_{\text{seg2}}^{\text{Yaw}} = \frac{3}{\sqrt{2\pi}} \frac{\Delta x}{\omega} \left[ \operatorname{erfc} \left( \frac{\sqrt{2}R}{\omega} \right) + \sqrt{\frac{8}{\pi}} \frac{R}{\omega} e^{-2\frac{R^2}{\omega^2}} \right] \quad (\text{C.14})$$

## Appendix D

### Overlap of Gaussian Beams

When a cavity is mode mismatched to an incoming laser field, the amount of power loss from scattering to higher order modes is quantified by the spatial overlap integral between the TEM00 cavity eigenmode and TEM00 of the input beam. An arbitrary Gaussian integral is defined as,

$$\begin{aligned} |A(r)\rangle &= \frac{A_0}{q(z)} e^{\frac{-ikr^2}{2q(z)}} \\ &= \frac{A_0}{q(z)} e^{\frac{-ikr^2(z-iz_0)}{2|q(z)|^2}} \end{aligned} \quad (\text{D.1})$$

where  $A_0$  is a real amplitude,  $q(z) = z + iz_0$  is the complex beam parameter,  $k$  is the wave number, and  $r$  is the radial variable in the transverse direction. Then normalizing to unity,

$$\langle A(r)|A(r)\rangle = \frac{|A_0|^2}{z^2 + z_0^2} \int_0^\infty e^{\frac{-kr^2 z_0}{|q(z)|^2}} 2\pi r dr = 1 \quad (\text{D.2})$$

$$A_0 = \sqrt{\frac{kz_0}{\pi}} \quad (\text{D.3})$$

For a Gaussian beam with arbitrary q-parameters,

$$|A_i\rangle = \frac{A_{0,i}}{q_i} e^{\frac{-ikr^2(z-iz_0)}{2|q_i|^2}} \quad (\text{D.4})$$

where  $z_{0,i}$  is the waist size of one particular beam, the overlap integral for the amplitude becomes

$$\langle A_1 | A_2 \rangle = 2i \frac{z_{0,1} z_{0,2}}{q_1 - q_2^*} \quad (\text{D.5})$$

So the power overlap is:

$$\text{Power Overlap} = |\langle A_1 | A_2 \rangle|^2 = 4 \frac{z_{0,1} z_{0,2}}{|q_1 - q_2^*|^2} \quad (\text{D.6})$$

Essentially, mode matching an optical system only requires the designer to match the incoming beam's q-parameter to the cavity's, so it makes sense that the final power overlap depends only on the waist size and location.

# List of Figures

1.1	A ring of free floating particles being stretched and squeezed by a passing gravitational wave. . . . .	9
1.2	A Michelson Interferometer. . . . .	10
1.3	Detector to radiation frame. . . . .	11
1.4	The phase response of an interferometer to a gravitational wave. . . . .	14
2.1	A heterodyne detection scheme for interferometers. . . . .	21
2.2	Delay Line (top) vs Fabry Perot (bottom) . . . . .	23
2.3	The reflected, circulating, and transmitted powers for a single Fabry-Perot cavity. . . . .	24
2.4	Bode Plots of a linear Fabry-Perot response in reflection. . . . .	25
2.5	Control scheme for an optical cavity. . . . .	28
2.6	Error signal in reflection . . . . .	29
2.7	Michelson with Fabry Perot arms . . . . .	30
2.8	A power recycled Fabry-Perot interferometer. . . . .	33
2.9	A dual recycled Fabry-Perot interferometer. . . . .	34
2.10	Comparing the shot noise limited differential arm spectra for different interferometer configurations. . . . .	35
2.11	Important sensor ports for Advanced LIGO . . . . .	37

2.12 Noise budget from GWINC (Gravitational Wave Interferometer Noise Calculator) . . . . .	38
2.13 Displacement spectrum for thermal noise. . . . .	49
3.1 A depiction of the Gaussian beam properties with respect to cylindrical coordinates. . . . .	59
3.2 Beam size, radius of curvature, and Gouy phase as a function of distance propagation from the waist. . . . .	60
3.3 Intensity . . . . .	61
3.4 Misalignment and mode mismatch between two different Gaussian beams. . .	65
3.5 A Finesse model of a longitudinal mode scan comparing the Advanced LIGO power recycling and signal recycling cavities. . . . .	71
4.1 Full interferometer simulation with FINESSE. . . . .	73
4.2 How FINESSE sees a beamsplitter. . . . .	74
4.3 Quantum limited sensitivity simulation to compare mismatches in the presence of squeezed light. . . . .	81
4.4 Simulating the output actuator phase spaces projected onto the OMC mode basis. . . . .	82
5.1 MEDM master screen for adaptive mode matching at Syracuse. . . . .	84
5.2 Model overview for adaptive mode matching. . . . .	90
5.3 Intensity profiles passing through a mode converter. . . . .	91
5.4 Simulated error signals from MATLAB (QPD) and FINESSE (BPD). . . . .	92
5.5 Passing a bullseye mode through a $\pi/2$ mode converter. . . . .	93
6.1 A simplified model for the effect of a substrate thermal lens on the carrier field.	96
6.2 A plane wave passing through a lens with a temperature gradient. . . . .	99
6.3 A conceptual model of flux balance for a cylindrical object. . . . .	101

<i>LIST OF FIGURES</i>	150
6.4 ITM Hartmann sensors optical layout.	110
6.5 Noise spectra for the HWS spherical lensing.	111
6.6 ITMX Hartmann Sensor output.	112
6.7 Clipping on ITMX Hartmann Sensor.	113
6.8 A time series of the interferometer power increase sequence.	114
6.9 ITMX gradient plots (left) and wavefront maps (right) during a power up to 30 Watts of input power.	115
6.10 ITMY gradient plots (left) and wavefront maps (right) during a power up to 30 Watts of input power.	116
6.11 Thermal lensing as seen by the ITM Hartmann Sensors after a lock loss.	118
6.12 Posterior distributions from fitting the Hartmann sensor spherical power.	119
6.13 Calculated TCS settings to balance the substrate lens.	120
6.14 Mode matching the arm cavities to the power recycling cavity.	121
6.15 Comparing 3-D plots of the optical path distortion for ITMX and ITMY test masses after powering up the interferometer.	126
6.16 Interferometer DC powers as a function of round trip arm loss and test mass absorption.	129
6.17 Model of POP-18 as a function of differential thermal lensing using FINESSE.	130
6.18 Vertex open loop transfer functions while in Nominal Low Noise.	131
6.19 Measuring vertex optical gains as a function of heating.	132

# List of Tables

2.1	Frequency bands of common seismic noise at LHO. . . . .	45
4.1	Mode matching actuation matrix for the transverse x direction. . . . .	78
4.2	Mode matching actuation matrix for the transverse y direction. . . . .	79
4.3	Calculated cavity parameters for the advanced LIGO interferometer. . . . .	80
6.1	Single pass actuator lensing calibrations for aLIGO TCS in micro-diopters/Watt.	122
C.1	Bullseye photodiode sensing matrix. . . . .	143

# Bibliography

- [1] J. Abadie et al. Sensitivity Achieved by the LIGO and Virgo Gravitational Wave Detectors during LIGO’s Sixth and Virgo’s Second and Third Science Runs. *arXiv*, 2012. 11
- [2] B. P. e. a. Abbott. Observation of gravitational waves from a binary black hole merger. *Phys. Rev. Lett.*, 116:061102, Feb 2016. doi: 10.1103/PhysRevLett.116.061102. URL <https://link.aps.org/doi/10.1103/PhysRevLett.116.061102>. 1
- [3] B. P. e. a. Abbott. Gw170817: Observation of gravitational waves from a binary neutron star inspiral. *Phys. Rev. Lett.*, 119:161101, Oct 2017. doi: 10.1103/PhysRevLett.119.161101. URL <https://link.aps.org/doi/10.1103/PhysRevLett.119.161101>. 1
- [4] R. Abbott, R. Adhikari, G. Allen, S. Cowley, E. Daw, D. DeBra, J. Giaime, G. Hammond, M. Hammond, C. Hardham, J. How, W. Hua, W. Johnson, B. Lantz, K. Mason, R. Mittleman, J. Nichol, S. Richman, J. Rollins, D. Shoemaker, G. Stapfer, and R. Stebbins. Seismic isolation for advanced ligo. *Classical and Quantum Gravity*, 19(7):1591, 2002. URL <http://stacks.iop.org/0264-9381/19/i=7/a=349>. 45
- [5] and and. Ix. a determination of the deflection of light by the sun’s gravitational field, from observations made at the total eclipse of may 29, 1919. *Philosophical Transactions of the Royal Society of London A: Mathematical, Physical and Engineering Sciences*, 220(571-581):291–333, 1920. ISSN 0264-3952. doi: 10.1098/rsta.1920.0009. URL <http://rsta.royalsocietypublishing.org/content/220/571-581/291>. 6

- [6] D. Z. Anderson. Alignment of resonant optical cavities. *Appl. Opt.*, 23(17):2944–2949, Sep 1984. doi: 10.1364/AO.23.002944. URL <http://ao.osa.org/abstract.cfm?URI=ao-23-17-2944>. 60
- [7] M. Beijersbergen, L. Allen, H. van der Veen, and J. Woerdman. Astigmatic laser mode converters and transfer of orbital angular momentum. *Optics Communications*, 96(1):123 – 132, 1993. ISSN 0030-4018. doi: [https://doi.org/10.1016/0030-4018\(93\)90535-D](https://doi.org/10.1016/0030-4018(93)90535-D). URL <http://www.sciencedirect.com/science/article/pii/003040189390535D>. 59, 88
- [8] P. G. Bergmann. Summary of the chapel hill conference. *Rev. Mod. Phys.*, 29:352–354, Jul 1957. doi: 10.1103/RevModPhys.29.352. URL <https://link.aps.org/doi/10.1103/RevModPhys.29.352>. 8
- [9] E. D. Black. An introduction to pound–drever–hall laser frequency stabilization. *American Journal of Physics*, 69(1):79–87, 2001. doi: 10.1119/1.1286663. URL <https://doi.org/10.1119/1.1286663>. 22, 28
- [10] D. G. Blair. *The detection of gravitational waves*. Cambridge University Press, 2005. 45
- [11] C. Bond, D. Brown, A. Freise, and K. A. Strain. Interferometer techniques for gravitational-wave detection. *Living Reviews in Relativity*, 19(1):3, Feb 2017. ISSN 1433-8351. doi: 10.1007/s41114-016-0002-8. URL <https://doi.org/10.1007/s41114-016-0002-8>. 72
- [12] C. e. a. Bond. Finesse input files for the h1 interferometer. URL <https://dcc.ligo.org/LIGO-T1300904>. 35, 74
- [13] A. Brooks, P. Veitch, J. Munch, and T.-L. Kelly. An off-axis hartmann sensor for the measurement of absorption-induced wavefront distortion in advanced gravitational

- wave interferometers. *General Relativity and Gravitation*, 37(9):1575–1580, Sep 2005. ISSN 1572-9532. doi: 10.1007/s10714-005-0137-5. URL <https://doi.org/10.1007/s10714-005-0137-5>. 108
- [14] A. F. Brooks. *Hartmann Wavefront Sensors for Advanced Gravitational Wave*. PhD thesis, The University of Adelaide, 7 2007. 109
- [15] A. F. Brooks, T.-L. Kelly, P. J. Veitch, and J. Munch. Ultra-sensitive wavefront measurement using a hartmann sensor. *Opt. Express*, 15(16):10370–10375, Aug 2007. doi: 10.1364/OE.15.010370. URL <http://www.opticsexpress.org/abstract.cfm?URI=oe-15-16-10370>. 108
- [16] A. F. Brooks, D. Hosken, J. Munch, P. J. Veitch, Z. Yan, C. Zhao, Y. Fan, L. Ju, D. Blair, P. Willems, B. Slagmolen, and J. Degallaix. Direct measurement of absorption-induced wavefront distortion in high optical power systems. *Appl. Opt.*, 48(2):355–364, Jan 2009. doi: 10.1364/AO.48.000355. URL <http://ao.osa.org/abstract.cfm?URI=ao-48-2-355>. 108
- [17] A. F. Brooks, B. Abbott, M. A. Arain, G. Ciani, A. Cole, G. Grabeel, E. Gustafson, C. Guido, M. Heintze, A. Heptonstall, M. Jacobson, W. Kim, E. King, A. Lynch, S. O’Connor, D. Ottaway, K. Mailand, G. Mueller, J. Munch, V. Sannibale, Z. Shao, M. Smith, P. Veitch, T. Vo, C. Vorvick, and P. Willems. Overview of advanced ligo adaptive optics. *Appl. Opt.*, 55(29):8256–8265, Oct 2016. doi: 10.1364/AO.55.008256. URL <http://ao.osa.org/abstract.cfm?URI=ao-55-29-8256>. 107, 109, 110, 111, 133
- [18] D. Brown. Personal Communication, 2018. 117
- [19] A. Buonanno and Y. Chen. Quantum noise in second generation, signal-recycled laser interferometric gravitational-wave detectors. *Phys. Rev. D*, 64:042006, Jul 2001. doi: 10.1103/PhysRevD.64.042006. URL <https://link.aps.org/doi/10.1103/PhysRevD.64.042006>. 39

- [20] S. M. Carroll. *Spacetime and geometry: an introduction to general relativity*. Pearson, 2003. 6
- [21] C. M. Caves. Quantum-mechanical noise in an interferometer. *Phys. Rev. D*, 23:1693–1708, Apr 1981. doi: 10.1103/PhysRevD.23.1693. URL <https://link.aps.org/doi/10.1103/PhysRevD.23.1693>. 39
- [22] C. M. Caves and B. L. Schumaker. New formalism for two-photon quantum optics. i. quadrature phases and squeezed states. *Phys. Rev. A*, 31:3068–3092, May 1985. doi: 10.1103/PhysRevA.31.3068. URL <https://link.aps.org/doi/10.1103/PhysRevA.31.3068>. 39, 50
- [23] C. M. Caves, K. S. Thorne, R. W. P. Drever, V. D. Sandberg, and M. Zimmermann. On the measurement of a weak classical force coupled to a quantum-mechanical oscillator. i. issues of principle. *Rev. Mod. Phys.*, 52:341–392, Apr 1980. doi: 10.1103/RevModPhys.52.341. URL <https://link.aps.org/doi/10.1103/RevModPhys.52.341>. 39
- [24] J. L. Cervantes-Cota, S. Galindo-Uribarri, and G. F. Smoot. A brief history of gravitational waves. *Universe*, 2(3), 2016. ISSN 2218-1997. doi: 10.3390/universe2030022. URL <http://www.mdpi.com/2218-1997/2/3/22>. 9
- [25] Y. Chen, S. L. Danilishin, F. Y. Khalili, and H. Müller-Ebhardt. Qnd measurements for future gravitational-wave detectors. *General Relativity and Gravitation*, 43(2):671–694, Feb 2011. ISSN 1572-9532. doi: 10.1007/s10714-010-1060-y. URL <https://doi.org/10.1007/s10714-010-1060-y>. 39
- [26] S. S. Y. Chua. *Quantum Enhancement of a 4km Laser Interferometer Gravitational-Wave Detector*. PhD thesis, The Australian National University, 4 2013. 53
- [27] L. Collaboration. Ligo optics. URL <https://galaxy.ligo.caltech.edu/optics/>. 32, 80

- [28] T. L. S. Collaboration. A gravitational wave observatory operating beyond the quantum shot-noise limit. *Nature Physics*, 7:962, Nov 2009. doi: 10.1038/nphys2083. URL <http://dx.doi.org/10.1038/nphys2083>. 50
- [29] T. L. S. Collaboration. Enhanced sensitivity of the ligo gravitational wave detector by using squeezed states of light. *Nature Physics*, 7:613, Jul 2013. doi: 10.1038/nphoton.2013.177. URL <http://dx.doi.org/10.1038/nphoton.2013.177>. 50
- [30] T. L. S. Collaboration. Advanced ligo. *Classical and Quantum Gravity*, 32(7):074001, 2015. URL <http://stacks.iop.org/0264-9381/32/i=7/a=074001>. 29
- [31] H. Collins. *Gravity's shadow: the search for gravitational waves*. University of Chicago Press, 2004. 9
- [32] R. DeRosa, J. C. Driggers, D. Atkinson, H. Miao, V. Frolov, M. Landry, J. A. Giaime, and R. X. Adhikari. Global feed-forward vibration isolation in a km scale interferometer. *Classical and Quantum Gravity*, 29(21):215008, 2012. URL <http://stacks.iop.org/0264-9381/29/i=21/a=215008>. 45
- [33] J. C. Driggers, J. Harms, and R. X. Adhikari. Subtraction of newtonian noise using optimized sensor arrays. , 86(10):102001, Nov. 2012. doi: 10.1103/PhysRevD.86.102001. 50
- [34] S. Dwyer, L. Barsotti, S. S. Y. Chua, M. Evans, M. Factourovich, D. Gustafson, T. Isogai, K. Kawabe, A. Khalaidovski, P. K. Lam, M. Landry, N. Mavalvala, D. E. McClelland, G. D. Meadors, C. M. Mow-Lowry, R. Schnabel, R. M. S. Schofield, N. Smith-Lefebvre, M. Stefszky, C. Vorvick, and D. Sigg. Squeezed quadrature fluctuations in a gravitational wave detector using squeezed light. *Opt. Express*, 21(16):19047–19060, Aug 2013. doi: 10.1364/OE.21.019047. URL <http://www.opticsexpress.org/abstract.cfm?URI=oe-21-16-19047>. 53

- [35] A. Einstein. Die grundlage der allgemeinen relativitätstheorie. *Annalen der Physik*, 354(7):769–822, 1905. doi: 10.1002/andp.19163540702. URL <https://onlinelibrary.wiley.com/doi/abs/10.1002/andp.19163540702>. 6
- [36] A. Einstein. Investigations on the theory of the brownian movement. *Ann. der Physik*, 1905. URL [http://www.physik.fu-berlin.de/~{}kleinert/files/eins\\_brownian.pdf](http://www.physik.fu-berlin.de/~{}kleinert/files/eins_brownian.pdf). 45
- [37] A. Einstein. Zur Elektrodynamik bewegter Körper. (German) [On the electrodynamics of moving bodies]. *Annalen der Physik*, 322(10):891–921, 1905. doi: <http://dx.doi.org/10.1002/andp.19053221004>. 6
- [38] R. W. et al. Ligo document m890001-v3, 1989. URL <https://dcc.ligo.org/LIGO-M890001/public>. 13
- [39] M. Evans, S. Ballmer, M. Fejer, P. Fritschel, G. Harry, and G. Ogin. Thermo-optic noise in coated mirrors for high-precision optical measurements. *Phys. Rev. D*, 78:102003, Nov 2008. doi: 10.1103/PhysRevD.78.102003. URL <https://link.aps.org/doi/10.1103/PhysRevD.78.102003>. 49
- [40] M. Evans, L. Barsotti, P. Kwee, J. Harms, and H. Miao. Realistic filter cavities for advanced gravitational wave detectors. *Phys. Rev. D*, 88:022002, Jul 2013. doi: 10.1103/PhysRevD.88.022002. URL <https://link.aps.org/doi/10.1103/PhysRevD.88.022002>. 52
- [41] L. S. Finn. Binary inspiral, gravitational radiation, and cosmology. *Phys. Rev.*, D53: 2878–2894, 1996. doi: 10.1103/PhysRevD.53.2878. 11, 14, 16
- [42] D. Foreman-Mackey, D. W. Hogg, D. Lang, and J. Goodman. emcee : The mcmc hammer. *Publications of the Astronomical Society of the Pacific*, 125(925):306, 2013. URL <http://stacks.iop.org/1538-3873/125/i=925/a=306>. 119

- [43] P. Fritschel, D. Shoemaker, and R. Weiss. Demonstration of light recycling in a michelson interferometer with fabry–perot cavities. *Appl. Opt.*, 31(10):1412–1418, Apr 1992. doi: 10.1364/AO.31.001412. URL <http://ao.osa.org/abstract.cfm?URI=ao-31-10-1412>. 32
- [44] P. Fritschel, N. Mavalvala, D. Shoemaker, D. Sigg, M. Zucker, and G. González. Alignment of an interferometric gravitational wave detector. *Appl. Opt.*, 37(28):6734–6747, Oct 1998. doi: 10.1364/AO.37.006734. URL <http://ao.osa.org/abstract.cfm?URI=ao-37-28-6734>. 45, 55
- [45] P. Fritschel, R. Bork, G. González, N. Mavalvala, D. Ouimette, H. Rong, D. Sigg, and M. Zucker. Readout and control of a power-recycled interferometric gravitational-wave antenna. *Appl. Opt.*, 40(28):4988–4998, Oct 2001. doi: 10.1364/AO.40.004988. URL <http://ao.osa.org/abstract.cfm?URI=ao-40-28-4988>. 22, 29
- [46] P. Fritschel, R. Bork, G. González, N. Mavalvala, D. Ouimette, H. Rong, D. Sigg, and M. Zucker. Readout and control of a power-recycled interferometric gravitational-wave antenna. *Appl. Opt.*, 40(28):4988–4998, Oct 2001. doi: 10.1364/AO.40.004988. URL <http://ao.osa.org/abstract.cfm?URI=ao-40-28-4988>. 32
- [47] C. C. Gerry and P. Knight. *Introductory quantum optics*. Cambridge University Press, 2005. 39, 41
- [48] G. I. González and P. R. Saulson. Brownian motion of a mass suspended by an anelastic wire. *The Journal of the Acoustical Society of America*, 96(1):207–212, 1994. doi: 10.1121/1.410467. URL <https://doi.org/10.1121/1.410467>. 49
- [49] D. J. Griffiths. *Introduction to quantum mechanics*. Pearson Prentice Hall, 2005. 39
- [50] G. M. Harry, A. M. Gretarsson, P. R. Saulson, S. E. Kittelberger, S. D. Penn, W. J. Startin, S. Rowan, M. M. Fejer, D. R. M. Crooks, G. Cagnoli, J. Hough, and

- N. Nakagawa. Thermal noise in interferometric gravitational wave detectors due to dielectric optical coatings. *Classical and Quantum Gravity*, 19(5):897, 2002. URL <http://stacks.iop.org/0264-9381/19/i=5/a=305>. 49
- [51] Y. Hefetz, N. Mavalvala, and D. Sigg. Principles of calculating alignment signals in complex resonant optical interferometers. *J. Opt. Soc. Am. B*, 14(7):1597–1606, Jul 1997. doi: 10.1364/JOSAB.14.001597. URL <http://josab.osa.org/abstract.cfm?URI=josab-14-7-1597>. 65
- [52] P. Hello and J.-Y. Vinet. Analytical models of thermal aberrations in massive mirrors heated by high power laser beams. *Journal de Physique*, 51(12):1267–1282, 1990. doi: 10.1051/jphys:0199000510120126700. 99
- [53] S. Hild, H. Grote, J. Degallaix, S. Chelkowski, K. Danzmann, A. Freise, M. Hewitson, J. Hough, H. Lück, M. Prijatelj, K. A. Strain, J. R. Smith, and B. Willke. Dc-readout of a signal-recycled gravitational wave detector. *Classical and Quantum Gravity*, 26(5):055012, 2009. URL <http://stacks.iop.org/0264-9381/26/i=5/a=055012>. 22
- [54] S. A. Hughes and K. S. Thorne. Seismic gravity-gradient noise in interferometric gravitational-wave detectors. *Phys. Rev. D*, 58:122002, Nov 1998. doi: 10.1103/PhysRevD.58.122002. URL <https://link.aps.org/doi/10.1103/PhysRevD.58.122002>. 50
- [55] I. K. and S. D. Frequency response of the aligo interferometer: part1. Technical report, California Institute of Technology, 2015. URL <https://dcc.ligo.org/LIGO-T1500325>. 37
- [56] I. K., S. D., and K. K. Frequency response of the aligo interferometer: part2. Technical report, California Institute of Technology, 2015. URL <https://dcc.ligo.org/LIGO-T1500461>. 37

- [57] I. K., S. D., and K. K. Frequency response of the aligo interferometer: part3. Technical report, California Institute of Technology, 2015. URL <https://dcc.ligo.org/LIGO-T1500559>. 37
- [58] H. J. Kimble, Y. Levin, A. B. Matsko, K. S. Thorne, and S. P. Vyatchanin. Conversion of conventional gravitational-wave interferometers into quantum nondemolition interferometers by modifying their input and/or output optics. *Phys. Rev. D*, 65:022002, Dec 2001. doi: 10.1103/PhysRevD.65.022002. URL <https://link.aps.org/doi/10.1103/PhysRevD.65.022002>. 39, 50, 51, 52
- [59] H. Kogelnik and T. Li. Laser beams and resonators. *Appl. Opt.*, 5(10):1550–1567, Oct 1966. doi: 10.1364/AO.5.001550. URL <http://ao.osa.org/abstract.cfm?URI=ao-5-10-1550>. 138
- [60] R. Lawrence, M. Zucker, P. Fritschel, P. Marfuta, and D. Shoemaker. Adaptive thermal compensation of test masses in advanced ligo. *Classical and Quantum Gravity*, 19(7):1803, 2002. URL <http://stacks.iop.org/0264-9381/19/i=7/a=377>. 95, 98, 107
- [61] O. D. M Rakhmanov, F Bondu and R. L. S. Jr. Characterization of the ligo 4 km fabry–perot cavities via their high-frequency dynamic responses to length and laser frequency variations. *Classical and Quantum Gravity*, Feb 2004. URL <http://iopscience.iop.org/article/10.1088/0264-9381/21/5/015/meta>. 24
- [62] F. Magana-Sandoval. Adaptive mode matching upgrade for advanced ligo. URL <https://dcc.ligo.org/LIGO-P1800143>. 83
- [63] F. Maticichard, B. Lantz, K. Mason, R. Mittleman, B. Abbott, S. Abbott, E. Allwine, S. Barnum, J. Birch, S. Biscans, D. Clark, D. Coyne, D. DeBra, R. DeRosa, S. Foley, P. Fritschel, J. Giaime, C. Gray, G. Grabeel, J. Hanson, M. Hillard, J. Kissel, C. Kucharczyk, A. L. Roux, V. Lhuillier, M. Macinnis, B. O'Reilly, D. Ottaway,

- H. Paris, M. Puma, H. Radkins, C. Ramet, M. Robinson, L. Ruet, P. Sareen, D. Shoemaker, A. Stein, J. Thomas, M. Vargas, and J. Warner. Advanced ligo two-stage twelve-axis vibration isolation and positioning platform. part 1: Design and production overview. *Precision Engineering*, 40:273 – 286, 2015. ISSN 0141-6359. doi: <https://doi.org/10.1016/j.precisioneng.2014.09.010>. URL <http://www.sciencedirect.com/science/article/pii/S0141635914001561>. 45
- [64] F. Matichard, B. Lantz, K. Mason, R. Mittleman, B. Abbott, S. Abbott, E. Allwine, S. Barnum, J. Birch, S. Biscans, D. Clark, D. Coyne, D. DeBra, R. DeRosa, S. Foley, P. Fritschel, J. Giaime, C. Gray, G. Grabeel, J. Hanson, M. Hillard, J. Kissel, C. Kucharczyk, A. L. Roux, V. Lhuillier, M. Macinnis, B. O'Reilly, D. Ottaway, H. Paris, M. Puma, H. Radkins, C. Ramet, M. Robinson, L. Ruet, P. Sareen, D. Shoemaker, A. Stein, J. Thomas, M. Vargas, and J. Warner. Advanced ligo two-stage twelve-axis vibration isolation and positioning platform. part 2: Experimental investigation and tests results. *Precision Engineering*, 40:287 – 297, 2015. ISSN 0141-6359. doi: <https://doi.org/10.1016/j.precisioneng.2014.11.010>. URL <http://www.sciencedirect.com/science/article/pii/S0141635914002098>. 45
- [65] F. Matichard, B. Lantz, R. Mittleman, K. Mason, J. Kissel, B. Abbott, S. Biscans, J. McIver, R. Abbott, S. Abbott, E. Allwine, S. Barnum, J. Birch, C. Celerier, D. Clark, D. Coyne, D. DeBra, R. DeRosa, M. Evans, S. Foley, P. Fritschel, J. A. Giaime, C. Gray, G. Grabeel, J. Hanson, C. Hardham, M. Hillard, W. Hua, C. Kucharczyk, M. Landry, A. L. Roux, V. Lhuillier, D. Macleod, M. Macinnis, R. Mitchell, B. O'Reilly, D. Ottaway, H. Paris, A. Pele, M. Puma, H. Radkins, C. Ramet, M. Robinson, L. Ruet, P. Sarin, D. Shoemaker, A. Stein, J. Thomas, M. Vargas, K. Venkateswara, J. Warner, and S. Wen. Seismic isolation of advanced ligo: Review of strategy, instrumentation and performance. *Classical and Quantum Gravity*, 32(18):185003, 2015. URL <http://stacks.iop.org/0264-9381/32/i=18/a=185003>. 45

- [66] E. Morrison, B. J. Meers, D. I. Robertson, and H. Ward. Automatic alignment of optical interferometers. *Appl. Opt.*, 33(22):5041–5049, Aug 1994. doi: 10.1364/AO.33.005041. URL <http://ao.osa.org/abstract.cfm?URI=ao-33-22-5041>. 60
- [67] G. Mueller, Q. ze Shu, R. Adhikari, D. B. Tanner, D. Reitze, D. Sigg, N. Mavalvala, and J. Camp. Determination and optimization of mode matching into optical cavities by heterodyne detection. *Opt. Lett.*, 25(4):266–268, Feb 2000. doi: 10.1364/OL.25.000266. URL <http://ol.osa.org/abstract.cfm?URI=ol-25-4-266>. 85, 89
- [68] E. Oelker, T. Isogai, J. Miller, M. Tse, L. Barsotti, N. Mavalvala, and M. Evans. Audio-band frequency-dependent squeezing for gravitational-wave detectors. *Phys. Rev. Lett.*, 116:041102, Jan 2016. doi: 10.1103/PhysRevLett.116.041102. URL <https://link.aps.org/doi/10.1103/PhysRevLett.116.041102>. 52
- [69] U. of Birmingham. *Finesse Manual*, 2014. URL <http://www.gwoptics.org/finesse/>. 35, 72
- [70] A. T. O’Neil and J. Courtial. Mode transformations in terms of the constituent hermite–gaussian or laguerre–gaussian modes and the variable-phase mode converter. *Optics Communications*, 181(1):35 – 45, 2000. ISSN 0030-4018. doi: [https://doi.org/10.1016/S0030-4018\(00\)00736-7](https://doi.org/10.1016/S0030-4018(00)00736-7). URL <http://www.sciencedirect.com/science/article/pii/S0030401800007367>. 59, 87, 88, 91
- [71] A. Perreca, J. Lough, D. Kelley, and S. W. Ballmer. Multidimensional optical trapping of a mirror. *Phys. Rev. D*, 89:122002, Jun 2014. doi: 10.1103/PhysRevD.89.122002. URL <https://link.aps.org/doi/10.1103/PhysRevD.89.122002>. 83
- [72] F. A. E. Pirani. Republication of: On the physical significance of the riemann tensor. *General Relativity and Gravitation*, 41(5):1215–1232, May 2009. ISSN 1572-9532. doi: 10.1007/s10714-009-0787-9. URL <https://doi.org/10.1007/s10714-009-0787-9>. 9

- [73] J. Ramette, M. Kasprzack, A. Brooks, C. Blair, H. Wang, and M. Heintze. Analytical model for ring heater thermal compensation in the advanced laser interferometer gravitational-wave observatory. *Appl. Opt.*, 55(10):2619–2625, Apr 2016. doi: 10.1364/AO.55.002619. URL <http://ao.osa.org/abstract.cfm?URI=ao-55-10-2619>. 117
- [74] B. E. A. Saleh and M. C. Teich. *Fundamentals of Photonics*. Wiley-Interscience, 2009. 56, 69
- [75] P. Saulson. *Fundamentals of Gravitational Wave Detectors*. World Scientific, 2016. 6, 13, 23, 47, 49
- [76] P. R. Saulson. Terrestrial gravitational noise on a gravitational wave antenna. *Phys. Rev. D*, 30:732–736, Aug 1984. doi: 10.1103/PhysRevD.30.732. URL <https://link.aps.org/doi/10.1103/PhysRevD.30.732>. 50
- [77] P. R. Saulson. Thermal noise in mechanical experiments. *Phys. Rev. D*, 42:2437–2445, Oct 1990. doi: 10.1103/PhysRevD.42.2437. URL <https://link.aps.org/doi/10.1103/PhysRevD.42.2437>. 49
- [78] P. R. Saulson. If light waves are stretched by gravitational waves, how can we use light as a ruler to detect gravitational waves? *American Journal of Physics*, 65(6):501–505, 1997. doi: 10.1119/1.18578. URL <https://doi.org/10.1119/1.18578>. 8
- [79] B. Schutz. *A First Course in General Relativity*. Cambridge University Press, 2009. 6
- [80] B. F. Schutz. *A first course in general relativity*. Cambridge University Press, 2009. 6
- [81] R. Shankar. *Principles of Quantum Mechanics*. Springer Verlag, 2014. 38, 39
- [82] J. A. Sidles and D. Sigg. Optical torques in suspended fabry–perot interferometers. *Physics Letters A*, 354(3):167 – 172, 2006. ISSN 0375-9601. doi: <https://doi.org/10.1016/j.physleta.2006.01.051>. URL <http://www.sciencedirect.com/science/article/pii/S0375960106001381>. 55

- [83] K. Strain, K. Danzmann, J. Mizuno, P. Nelson, A. Rüdiger, R. Schilling, and W. Winkler. Thermal lensing in recycling interferometric gravitational wave detectors. *Physics Letters A*, 194(1):124 – 132, 1994. ISSN 0375-9601. doi: [https://doi.org/10.1016/0375-9601\(94\)00717-4](https://doi.org/10.1016/0375-9601(94)00717-4). URL <http://www.sciencedirect.com/science/article/pii/0375960194007174>. 107
- [84] P. Veitch, A. Brooks, W. Kim, C. Blair, H. Cao, G. Grabeel, T. Hardwick, M. Heintze, A. Heponstall, C. Ingram, J. Munch, D. Ottaway, and T. Vo. Hartmann wavefront sensors for advanced ligo. In *Conference on Lasers and Electro-Optics*, page SW3M.5. Optical Society of America, 2018. doi: 10.1364/CLEO\_SI.2018.SW3M.5. URL [http://www.osapublishing.org/abstract.cfm?URI=CLEO\\_SI-2018-SW3M.5](http://www.osapublishing.org/abstract.cfm?URI=CLEO_SI-2018-SW3M.5). 108
- [85] J.-Y. Vinet. On special optical modes and thermal issues in advanced gravitational wave interferometric detectors. *Living Reviews in Relativity*, 12(1):5, Jul 2009. ISSN 1433-8351. doi: 10.12942/lrr-2009-5. URL <https://doi.org/10.12942/lrr-2009-5>. 99, 104, 123
- [86] H. Wang, C. Blair, M. D. Álvarez, A. Brooks, M. F. Kasprzack, J. Ramette, P. M. Meyers, S. Kaufer, B. O'Reilly, C. M. Mow-Lowry, and A. Freise. Thermal modelling of advanced ligo test masses. *Classical and Quantum Gravity*, 34(11):115001, 2017. URL <http://stacks.iop.org/0264-9381/34/i=11/a=115001>. 117
- [87] J. Weber. Evidence for discovery of gravitational radiation. *Phys. Rev. Lett.*, 22:1320–1324, Jun 1969. doi: 10.1103/PhysRevLett.22.1320. URL <https://link.aps.org/doi/10.1103/PhysRevLett.22.1320>. 9
- [88] J. M. Weisberg, J. H. Taylor, and L. A. Fowler. Gravitational waves from an orbiting pulsar. *Scientific American*, 245(4):74–83, 1981. ISSN 00368733, 19467087. URL <http://www.jstor.org/stable/24964580>. 6
- [89] W. Winkler, K. Danzmann, A. Rüdiger, and R. Schilling. Heating by optical absorption

- and the performance of interferometric gravitational-wave detectors. *Phys. Rev. A*, 44: 7022–7036, Dec 1991. doi: 10.1103/PhysRevA.44.7022. URL <https://link.aps.org/doi/10.1103/PhysRevA.44.7022>. 95, 107
- [90] H. Yu, D. Martynov, S. Vitale, M. Evans, D. Shoemaker, B. Barr, G. Hammond, S. Hild, J. Hough, S. Huttner, S. Rowan, B. Sorazu, L. Carbone, A. Freise, C. Mow-Lowry, K. L. Dooley, P. Fulda, H. Grote, and D. Sigg. Prospects for detecting gravitational waves at 5 hz with ground-based detectors. *Phys. Rev. Lett.*, 120:141102, Apr 2018. doi: 10.1103/PhysRevLett.120.141102. URL <https://link.aps.org/doi/10.1103/PhysRevLett.120.141102>. 45